PhotoniX Life

Open Access
PhotoniX Life (2026)1:3
https://doi.org/10.3724/PXLIFE.2025-0008

Review

Recent progress on lanthanide-doped photon conversion nanoparticles for biological and medical applications

Chang Jiang[1#], Xindong Wang[2#], Hui Li[3#], Paras N. Prasad[4*] AND Guanying Chen[1*]

[1]School of Chemistry and Chemical Engineering, Harbin Institute of Technology, Harbin 150001, China;
[2]Medical-Industrial Integration Research Centre, Sun Yat-sen Memorial Hospital, Sun Yat-sen University, Guangzhou 510120, China;
[3]School of Medicine, Southeast University, Nanjing 210009, China;
[4]Institute for Lasers, Photonics, and Biophotonics, Department of Chemistry, University at Buffalo, State University of New York, New York 14221, USA
* Corresponding authors (emails: pnprasad@buffalo.edu (P.N.P.); chenguanying@hit.edu.cn (G.C.))
# These authors contributed equally to this work.

Received 9 May 2025; accepted 24 January 2026; published online 31 March 2026

Abstract Lanthanide-doped nanoparticles possess exceptional optical properties, including photon upconversion and downconversion, long emission lifetimes, narrow bandwidths, and outstanding photostability, establishing their prominence in optical detection and imaging, particularly in biological and medical contexts. This review offers a comprehensive overview of recent advancements in enhancing their photon conversion efficiency and explores their applications across biological and medical fields. While they have driven major progress in biological research, clinical adoption remains limited by regulatory and ethical hurdles, notably the lack of the U.S. Food and Drug Administration approval for human use. However, their compatibility with medical devices presents a promising avenue for overcoming these barriers. We conclude by highlighting current limitations and proposing strategic directions to advance the clinical translation of these luminescent systems.

Keywords lanthanide, upconversion, near-infrared, biological imaging, medical diagnostics, clinical translation

1. Introduction

Lanthanide-doped luminescent materials have emerged as a powerful and versatile class of optical probes, offering unique advantages that make them particularly attractive for a wide array of biological and medical applications [1-5]. The exceptional optical behavior of these materials originates from the shielded 4f electrons of trivalent lanthanide (Ln^{3+}) ions, whose $[Xe]4f^n$ electronic configurations give rise to intra-4f transitions that are largely unaffected by the surrounding chemical environment. These transitions enable a range of distinct photophysical properties, including sharp emission bands [6], long luminescence lifetimes [7,8], and broad spectral tunability ranging from the ultraviolet (UV) to the near-infrared (NIR) range [9].

A hallmark of lanthanide-doped nanoparticles (LnNPs) is their ability to exhibit both upconversion and downconversion luminescence (DCL). Upconversion involves the sequential absorption of multiple NIR photons, culminating in the emission of higher-energy photons (anti-Stokes emission), facilitated by the ladder-like energy levels of Ln^{3+} ions [10-12]. Conversely, downconversion processes convert high-energy photons into lower-energy emissions, typically spanning the visible to NIR range. Compared with other luminescent platforms such as quantum dots (QDs) [13], carbon dots [14], and gold nanoclusters [15], LnNPs offer distinct photon conversion capabilities and optical behaviors that are difficult to replicate with conventional fluorophores.

Building on these unique photophysical processes, LnNPs provide several advantages for biomedical applications. Their near-zero autofluorescence background significantly improves *in vivo* signal-to-noise ratios [16,17], while their large anti-Stokes shifts enable clean separation of excitation and emission channels. The intrinsically narrow emission linewidths of lanthanide ions facilitate high-precision multiplexing [18], and their exceptional photostability ensures reliable imaging under prolonged excitation [19,20]. Additional attributes such as non-blinking emission [21], reduced light scattering, and efficient deep-tissue penetration—enabled by NIR excitation within the biological transparency window [22,23]—further support their utility in complex biological environments. Moreover, the long luminescence lifetimes of lanthanide emitters allow time-resolved detection and lifetime multiplexing, providing temporal discrimination advantages unavailable in most organic dyes or semiconductor nanomaterials [7,8,24].

These unique properties position LnNPs as strong candidates for a wide range of theranostic applications, including targeted imaging [25], drug delivery [26-28], biosensing [29-31], and light-triggered therapy [32-34]. However, despite this promise, the clinical translation of these materials remains limited. A principal challenge arises from the inherently low absorption cross-sections of Ln^{3+} ions, leading to suboptimal excitation efficiency. Compounding this are unresolved concerns surround-

© The Author(s) 2026. This is an Open Access article distributed under the CC BY-NC-ND license (https://creativecommons.org/licenses/by-nc-nd/4.0/).

ing biocompatibility, biodegradability, and long-term biosafety, all of which are essential for regulatory approval and routine clinical use. To date, no LnNPs have received the U.S. Food and Drug Administration (FDA) approval for human application, underscoring the substantial regulatory and ethical hurdles that remain. Nonetheless, their compatibility with existing medical instrumentation—such as optical imaging platforms, endoscopes, and wearable sensors—offers a promising route to bridge the gap between research and clinical application. By leveraging this technological alignment, it may be possible to accelerate their adoption in real-world medical settings. To facilitate future clinical translation, it is essential to address both the optical performance and long-term biosafety of LnNPs, as well as their integration with existing medical devices.

This review provides a comprehensive assessment of recent strategies aimed at enhancing the optical performance of lanthanide-doped materials and evaluates their evolving roles in biological and medical sciences. While their utility in fundamental biological research is well established, overcoming the translational barriers remains critical for broader medical integration. We conclude by outlining key limitations and proposing strategic pathways to address them, charting a course toward the future clinical deployment of these advanced luminescent systems.

2. Synthesis of photon conversion nanoparticles

The 2023 Nobel Prize in chemistry was awarded for advancements in QDs [13], bringing the frontier progress of nanomaterials to the forefront of scientific attention. In 1983, the quantum size effect was discovered in inorganic nanomaterials, where the band gap of nanoparticles increases as their size decreases, leading to unique optical, electrical, and catalytic properties. Among various inorganic nanomaterials, rare-earth nanomaterials have garnered widespread interest due to the distinctive properties of the 4f electrons in rare-earth elements. The development of simple and efficient synthesis strategies for high-quality LnNPs, with precisely controlled crystalline phases, shapes, and sizes, is crucial for tailoring their physicochemical properties. This control plays a pivotal role in unlocking the diverse potential of these materials, particularly for their use in various biological applications. Consequently, advancing synthesis techniques for Ln^{3+}-doped nanoparticles is likely to enhance their compatibility with a wide range of bioapplications, fostering further progress in both biological research and clinical settings.

2.1 Core lanthanide-doped nanoparticles

2.1.1 Thermal decomposition synthesis

The thermal decomposition method, initially proposed for the synthesis of LnNPs, involves the breakdown of organofluoride precursors at elevated temperatures, typically above 300 °C. This endothermic process utilizes heat to break bonds within molecular structures, releasing fluoride and lanthanide ions, which are key to the formation of LnNPs. Common precursors include trifluoroacetates such as CF_3COONa and $Ln(CF_3COO)_3$ (Ln = Y, Yb, Tm, Ho, and Er), which, upon decomposition, yield fluoride-metal complexes, facilitating the nucleation and growth of nanocrystals [35].

One of the pioneering studies in this field by Ye et al. [36] used CF_3COONa and $Ln(CF_3COO)_3$ as precursors. By manipulating parameters such as reaction time and precursor ratios, the morphology of the LnNPs was finely tuned, achieving diverse nanostructures from nanospheres to nanoprisms (Figure 1a–c). This method demonstrated excellent control over the synthesis of various lanthanide-doped nanocrystals, including $NaYF_4$, $NaGdF_4$, $NaYbF_4$, $NaLuF_4$, and $LiYF_4$, showing promise in tailoring nanocrystal properties [35,37-41]. A notable advancement by You et al. [42] introduced a solid-liquid thermal decomposition approach using $NaHF_2$ and $Ln(CH_3COO)_3$. This method produced monodispersed β-$NaYF_4$-based LnNPs with high scalability (>67 g per synthesis), which is significantly higher than the yield of other approaches (typically around 100 mg per synthesis). By carefully controlling reaction parameters and adding CH_3COONa, they successfully synthesized LnNPs of varying sizes and phases. This method's scalability suggests strong potential for industrial applications, with post-processing techniques like surface modification enhancing the functionality of the LnNPs [42,43].

However, despite its advantages, the thermal decomposition process has some drawbacks. The excessive fluoride present during synthesis can lead to the formation of HF gas under high temperatures, and toxic fluorinated byproducts may emerge from the pyrolysis of trifluoroacetates. Therefore, this synthesis method should be conducted in a well-ventilated environment to mitigate potential hazards. In summary, thermal decomposition remains a valuable and widely used technique for synthesizing LnNPs, offering excellent control over nanocrystal properties and scalability for industrial applications, although safety precautions are necessary to handle hazardous byproducts.

2.1.2 High-temperature coprecipitation synthesis

In recent years, several innovative strategies have been developed to address the disadvantages of traditional thermal decomposition methods for synthesizing LnNPs. One significant effort is the use of non-toxic reagents to minimize the generation of hazardous fumes. Yi et al. [44] introduced a method for preparing α-phase $NaYF_4$:Yb^{3+},Er^{3+} LnNPs using ethylenediaminetetraacetic acid (EDTA) as a capping ligand, replacing the conventional organofluoride complexes that are discouraged due to their toxicity. In this approach, rare-earth oxides (Ln_2O_3, Ln = Y, Yb, Er) were used as the lanthanide precursors. Unlike traditional thermal decomposition, this method did not involve a pyrolysis step, and the size of LnNPs was controlled by adjusting the EDTA-to-Ln ions ratio. However, this method led to non-uniform sizes and shapes, highlighting the need for further improvements in crystal growth control [44].

Similarly, Heer et al. [45] employed a high-temperature co-precipitation method using 1-adamantanecarboxylic acid as a capping and chelating ligand. Although this method reduced toxicity, it still resulted in non-uniform LnNPs, indicating that better control over the synthesis process was needed. A more refined approach was introduced by Li et al. [46], who developed a high-temperature co-precipitation method that produced highly uniform β-$NaYF_4$:Yb^{3+},Er^{3+} LnNPs. In this process, rare-earth chloride ($LnCl_3$), ammonium fluoride (NH_4F), and sodium

hydroxide (NaOH) were used as precursors, eliminating the need for excess fluoride. A key feature of this method was the pre-nucleation step at room temperature, where amorphous $NaYF_4$ precipitates formed and acted as nuclei during the subsequent high-temperature incubation. This approach significantly improved the uniformity and crystallinity of the LnNPs, resulting in well-dispersed nanoparticles with high upconversion luminescence (UCL). Additionally, by adjusting the concentration of oleic acid (OA), the morphology could be finely tuned from ellipsoidal to hexagonal shapes. This method has become one of the most popular and successful routes for LnNPs synthesis, successfully applied to the preparation of various materials such as $NaYF_4$, $NaErF_4$, $NaGdF_4$, $NaTbF_4$, $NaYbF_4$, and others [46-48]. These advances highlight the progress in developing safer and more efficient methods for synthesizing LnNPs, with improved control over particle size, shape, and crystallinity.

2.1.3 Hydrothermal synthesis

The hydrothermal method has emerged as an effective approach for the synthesis of LnNPs due to the high-pressure and temperature conditions it enables, which promote crystal growth at lower temperatures than traditional high-temperature methods. Water, as a solvent, provides numerous advantages, including its ability to dissolve ionic complexes such as lanthanide chlorides and its high polarity, which accelerates crystallization under elevated pressure and temperature. By increasing pressure, the boiling point of water can be raised, leading to a subcritical water environment that enhances the reaction rate and supersaturation, thus facilitating nucleation and crystallization at temperatures as low as ~200 °C, compared to ~300 °C for typical high-temperature methods [49].

Wang et al. [50] utilized the hydrothermal method to synthesize rod-shaped $NaLnF_4$ LnNPs by adding precursors, surfactants, and solvents before the reaction. The mixture was then transferred into a sealed autoclave and heated under elevated conditions, producing highly uniform $NaLnF_4$ LnNPs. By adjusting the Gd^{3+}/Y^{3+} stoichiometric ratio, they also successfully tuned the crystal lattice symmetry, transforming the LnNPs from a cubic (α-phase) to a hexagonal (β-phase) structure. In another study, Zhang et al. [51] demonstrated the versatility of the method by synthesizing LnNPs with diverse shapes, including tubes, plates, bars, and intricate flower-like structures, by optimizing reaction parameters and surfactant addition.

Further innovation in hydrothermal synthesis was introduced by Jiao et al. [52], who incorporated flow chemistry into the process, enabling the continuous production of uniformly distributed LnNPs. Under conditions of 260 °C and 30 bar, this setup produced LnNPs in a continuous manner, with size control facilitated by adding low-boiling-point solvents such as cyclohexane or methanol. This approach has been successfully applied to fabricate various LnNPs, including $NaYF_4$, $NaGdF_4$, and $NaLuF_4$, demonstrating its scalability and versatility for diverse materials [52].

2.1.4 Aerosol synthesis

Malekzadeh et al. [53] introduced an aerosol nanosynthesis technique for producing rare-earth containing nanoparticles, which uses laser pyrolysis with a 10.6 μm CO_2 laser (Figure 1d). The laser action generates rapid heating of precursors, leading to decomposition and nanoparticle nucleation, wherein SF_6 can absorb the laser beam and transfer energy to the precursors. They were able to dope the $NaYF_4$ nanocrystals during synthesis with ytterbium as a sensitizer and erbium, thulium, or holmium as an upconversion emitter. They optimized the laser pyrolysis process and introduced postsynthesis calcination to maximize emission at each emission color. Their work also showed that these laser-synthesized LnNPs can be dispersed in many solvents, retaining their visible upconversion emission, thus opening the possibility of creating inks for printing in anticounterfeiting applications, which they demonstrated by drop-casting.

2.1.5 Green synthesis strategies

1) Microbial synthesis

The hot colloidal synthesis of photon upconversion nanoparticles as described in Sects. 2.1.1, 2.1.2, and 2.1.3 requires high temperature, potentially toxic organic solvents, and high concentrations of precursors. University at Buffalo, State University of New York, in collaboration with the Andrés Bello University (Chile), reported the first microorganism-mediated biosynthesis, a green synthesis approach to produce rare-earth containing nanoparticle photon converters. They reported biosynthesis of terbium sulfide (TbS) NPs using *Escherichia coli* [54]. They identified conditions under which *Escherichia coli* extracellularly formed TbS nanoparticles in aqueous media at 37 °C by producing a high concentration of sulfide ions. Characterization by electron microscopy and electron diffraction showed highly crystalline ultrasmall spherical nanoparticles with a mean diameter of (4.1±1.3) nm. Characteristic UV-visible absorption and photoluminescence (PL) of Tb were observed with a downshifting (DS) quantum yield reaching 28.3% and an emission lifetime of ~2 ms. This first reported biosynthesis of Rare-earth sulfide nanoparticles demonstrated that TbS nanoparticles could be produced at room temperature with spherical shape, average size below 5 nm, a size that has not been achieved by chemical methods.

In another report, they utilized Antarctic *Shewanella baltica* and their genetic modifications to biosynthesize Er-doped fluoride nanocrystals (Figure 1e) [55]. They found that incubating bacterial cells with the precursor components in a slightly acidic condition produced the LnNPs in the bacterial periplasm, which adhered to the outer cell membrane and were dispersed extracellularly. The produced $NaYF_4$:Yb^{3+},Er^{3+} showed upconverted emission when excited at 980 nm. Enhancement of the upconverted emission was observed upon heating, likely resulting from enhanced crystallinity of the LnNPs, together with surrounding organic matter carbonization and removal.

2) Room temperature synthesis

The development of room temperature approaches for the synthesis of LnNPs has gained significant attention due to their potential to reduce energy consumption, labor costs, and the need for toxic organometallic salts or protective gas environments. Traditional high-temperature synthesis methods are energy-intensive and time-consuming, necessitating alternative approaches that are more efficient for mass production. Chen et al. [56] pioneered a phase transition method to prepare $NaYF_4$ LnNPs under relatively mild conditions. Although this method

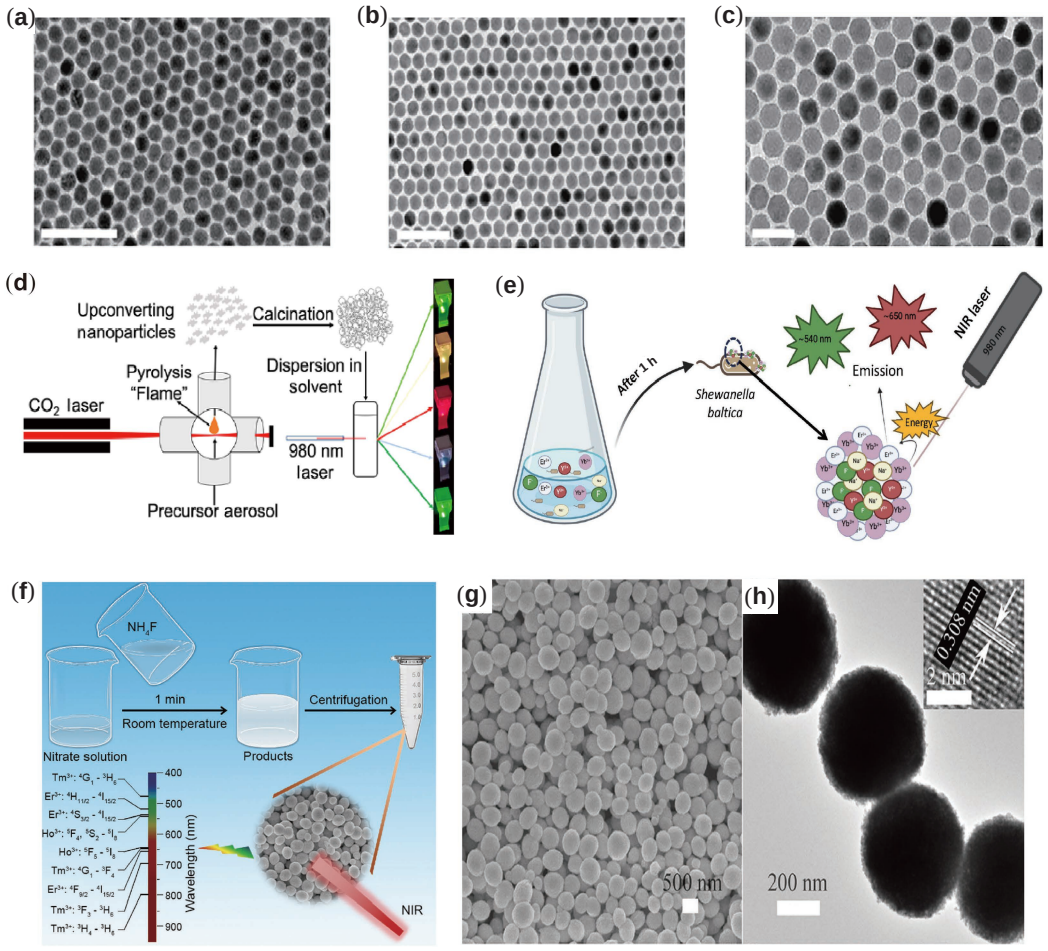

Figure 1 TEM images of **a** $NaYF_4$:20Yb^{3+},2Er^{3+} LnNPs, **b** $NaYF_4$:22Yb^{3+}/0.2Tm^{3+} LnNPs, and **c** $NaYF_4$:20Yb^{3+},11Ce^{3+},2Ho^{3+} LnNPs prepared by thermal decomposition method [36]. Scale bar: 100 nm. **d.** Illustration of the laser-pyrolysis synthesis of lanthanide-doped $NaYF_4$ LnNPs [53]. **e.** The use of bacteria from the *Shewanella* genus as a biofactory for UCNP biosynthesis through an easy room temperature and low precursor concentration protocol [55]. **f.** Schematic illustration of the synthesis procedure of $NaBiF_4$:Yb^{3+},Ln^{3+} (Ln = Er, Ho, Tm) nanoparticles and the main emitting transitions of Ln^{3+} (Ln = Er, Ho, Tm) in the visible and NIR part of the electromagnetic spectrum. Characterization of NaBiF4:Yb^{3+}/Er^{3+} nanoparticles (obtained in 1 min at room temperature): **g** SEM image, **h** TEM and HRTEM image (inset in **h**) [57]. Reproduced with permission from Refs. [53,57]. Copyright©2023 American Chemical Society and Copyright©2017 Wiley-VCH.

yielded LnNPs with good UCL, the crystals exhibited non-uniform shapes and sizes, highlighting challenges in controlling the crystallization process.

A more recent breakthrough by Lei et al. [57] utilized Bi^{3+} doping and $NaBiF_4$ as the matrix for the fast synthesis of LnNPs at room temperature. Bismuth, which shares similar ionic properties with lanthanide ions, proved to be a cost-effective, environmentally friendly, and biologically safe dopant for enhancing UCL. In their method, $NaBiF_4$ LnNPs were formed rapidly by adding NH_4F to lanthanide precursors within one minute, resulting in well-crystallized and uniform LnNPs (Figure 1f–h) [57]. X-ray diffraction (XRD) and scanning electron microscopy (SEM) confirmed the uniformity and crystalline quality of the LnNPs. These $NaBiF_4$-based LnNPs displayed strong UCL under 980 nm laser excitation, making them promising candidates for future industrial applications. However, this method was less effective for $NaLnF_4$-based LnNPs, potentially due to incomplete crystallization at room temperature, underscoring the challenges that still exist in synthesizing LnNPs under mild conditions [58].

In summary, room temperature approaches for LnNPs synthesis, such as those by Chen et al. [56] and Lei et al. [57], offer significant advantages in terms of reduced energy requirements and simplified processes. However, challenges remain, particularly in achieving uniform crystallization and UCL performance across various matrix compositions. These advances demonstrate the potential for scaling up LnNPs production with environmentally benign methods.

2.1.6 Synthesis of metal ions-doped lanthanide-doped nanoparticles

Alkali-metal ion co-doping, especially with Li^+, is commonly achieved during nanoparticle synthesis by introducing lithium salts (e.g., LiCl, $LiNO_3$, Li-acetate) directly into precursor solutions. In thermal decomposition and sol-gel routes, simultaneous addition of Li^+ with lanthanide precursors allows uniform incorporation into the host lattice. For example, Debasu et al. [59] synthesized Li^+-doped Y_2O_3:Yb^{3+},Er^{3+} nanocrystals by co-

dissolving Li^+ and lanthanide precursors followed by high-temperature calcination, achieving controlled phase formation and homogeneous dopant distribution. Similar co-precipitation strategies were applied in Li^+-doped ZrO_2 and $NaGdF_4$ nanoparticles by Pei et al. [60], where Li^+ was introduced during nucleation to regulate crystal growth. In solvothermal systems, Devi et al. [61] demonstrated that controlling Li^+ concentration and post-annealing temperature allowed precise tuning of crystallinity and particle morphology.

Host matrices containing Ca^{2+} are frequently prepared through hydrothermal or sol-gel synthesis, where calcium salts (e.g., $Ca(NO_3)_2$, $CaCl_2$) are co-introduced with lanthanide precursors. In calcium vanadate nanophosphors, Chukova et al. [62] employed a wet chemical route followed by controlled thermal treatment to yield Ca-based lattices uniformly doped with Eu^{3+} and Er^{3+}.

Transition-metal ion doping (Mn^{2+}, Ni^{2+}, Cr^{3+}) is typically realized using corresponding metal acetates or trifluoroacetates in thermal decomposition or solvothermal processes. A scalable synthesis of Na_3CrF_6:Ln nanoparticles using metal trifluoroacetate precursors demonstrated the effective incorporation of Cr^{3+} and Mn^{2+} through controlled precursor ratios and reaction temperatures [63].

Overall, these studies highlight that ion-doped LnNPs are predominantly synthesized through co-precipitation, solvothermal, sol-gel, and thermal decomposition routes, where precise control of precursor composition, reaction temperature, and post-annealing conditions enables reproducible incorporation of Li^+, Ca^{2+}, and transition-metal ions into the host lattice.

2.2 Core-shell lanthanide-doped nanoparticles

2.2.1 Seed-assisted growth

Core-shell LnNPs are typically synthesized by epitaxial growth of shells over core LnNPs. In this seed-assisted growth method, pre-prepared LnNPs cores are introduced into the reaction environment prior to nucleation. This leads to heterogeneous nucleation and crystal growth, as the core particles disrupt the homogeneous nucleation process. The result is the formation of core-shell LnNPs, where the shell grows epitaxially over the core surface. This technique has been widely used to prepare core-shell LnNPs, including Core@$NaYF_4$ [46,64,65], Core@CaF_2 [66-68], Core@$NaGdF_4$ [69], and Core@$NaLuF_4$ [70,71].

A detailed study on the seed-assisted synthesis of core-shell LnNPs was conducted by Liu et al. [72], who investigated the influence of various parameters, such as OA concentration, Ln^{3+} ions, incubation temperature, and fluoride sources, on the final morphology of LnNPs (Figure 2a). OA/OA^- was used as the capping ligand, with the binding preferences of OA and oleate varying depending on the crystal planes of $NaLnF_4$ LnNPs. By adjusting the pH and the amount of sodium hydroxide, the researchers successfully controlled the epitaxial growth of the shell in two orthogonal directions. This led to the synthesis of LnNPs with a variety of morphologies, including dumbbell, flower, bamboo-like, and hourglass shapes, with high uniformity.

Similarly, Qian et al. [65] reported that the different binding affinities of EDTA and citric acid towards crystal facets influenced the shell growth orientation when used as surface ligands for LnNPs. These studies highlight that the epitaxial shell growth of core-shell LnNPs is governed by multiple factors, particularly the ligand effect, which plays a crucial role in controlling the final morphology of the nanocrystals.

2.2.2 Ostwald ripening strategy

The Ostwald ripening strategy involves the use of small or α-phase LnNPs as shell precursors, which are less stable and have high surface energy. When subjected to high temperatures, these LnNPs dissolve and re-deposit on the core LnNPs via epitaxial growth, forming the shell. This method, first described by in 1896, enhances the formation of discrete core-shell LnNPs by minimizing phase separation between the core and the shell precursors. The advantage of Ostwald ripening is that no new nucleation is induced from the surrounding environment, leading to a more controlled and uniform growth process. Zhang et al. [73] showed that lanthanide ions, when used as precursors, did not directly grow on the cores but formed small LnNPs. Conversely, the use of α-phase LnNPs resulted in tip-modified core-shell LnNPs. This method has been successfully employed in the synthesis of various core-shell LnNPs, including Core@-$NaYF_4$ [73,74] and Core@$NaGdF_4$ [75]. The Ostwald ripening strategy offers the advantage of improved homogeneity and a higher degree of control over the final nanocrystal morphology.

2.2.3 Cation exchange approach

The cation exchange method involves the exchange of surface cations with different metal ions to form a shell over the core particles. This approach, although not producing traditional core-shell LnNPs with thick shells, results in a thin atomic layer on the surface. Despite this limitation, the cation exchange method offers significant advantages over other synthesis techniques. Notably, it enables *in situ* luminescence tuning under mild conditions, which is challenging to achieve with conventional methods. Moreover, the method does not induce significant changes in size or morphology, making it unique among core-shell LnNPs synthesis strategies.

Dong et al. [76] were the first to employ the cation exchange strategy to prepare core-shell LnNPs, depositing a LnF_3 layer on a GdF_3 core through the exchange of La^{3+} and Gd^{3+}. This process was facilitated by citrate species, which also prevented precipitation by stabilizing the LnNPs. In a more systematic study, Han et al. [77] explored the cation exchange of various lanthanide and transition metal ions, such as Tb^{3+}, Eu^{3+}, Mn^{2+}, Dy^{3+}, and Ce^{3+}, on $NaGdF_4$, resulting in core-shell LnNPs with novel UCL features (Figure 2b and c). Additionally, Hao et al. [78] introduced a CaF_2 shell layer on $NaGdF_4$ by exchanging Na^+ with Ca^{2+}, creating a buffer layer for subsequent heteroepitaxial growth . This method is gaining popularity due to its simplicity, cost-effectiveness, and ability to achieve *in situ* luminescence tuning without altering the core's size or morphology, offering promising applications in various fields.

3. Strategies for improved optical performances of lanthanide-doped materials

Lanthanide-doped materials possess unique optical properties that arise from the characteristic 4f–4f electronic transitions of Ln^{3+} ions, enabling both upconversion and DCL. These photophysical

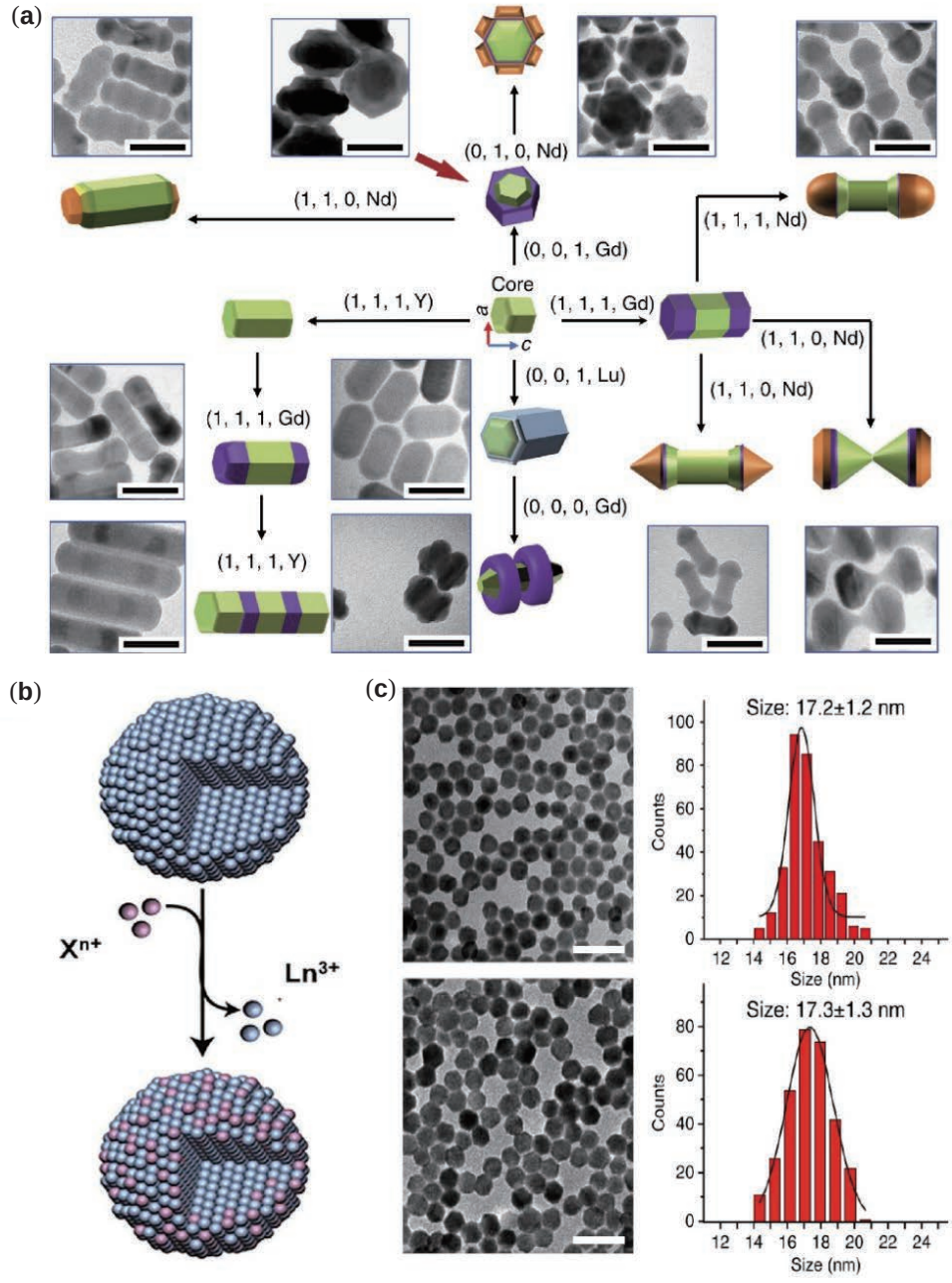

Figure 2 **a.** Different reaction conditions can control the four digital condition codes by modulating the OA/OA^- ratio, the temperature, the source of F^- ions, and the Ln^{3+} concentration. **b.** Schematic representation of a typical cation exchange process, occurring at the particle surface, between Ln^{3+} and exchange X^{n+} ions. **c.** Low-resolution TEM images and corresponding size distributions of the as-prepared $NaGdF_4$:Yb/Tm@$NaGdF_4$ nanoparticles, obtained before (top panel) and after (bottom panel) incubation with $TbCl_3$ [77].

processes underpin a wide range of applications in bioimaging, sensing, and photonic technologies. Upconversion is an anti-Stokes process in which the sequential absorption of two or more low-energy photons leads to the emission of a higher-energy photon. This nonlinear mechanism relies on the long-lived intermediate states and well-defined ladder-like energy levels of Ln^{3+} ions. UCL primarily proceeds via three fundamental pathways: (1) excited state absorption (ESA), (2) energy transfer upconversion (ETU), and (3) cooperative sensitization upconversion (CSU).

In the ESA mechanism (Figure 3a), a single ion sequentially absorbs multiple pump photons, typically in the NIR region, to reach an excited emissive state. For efficient ESA, the energy differences between the ground state (G), intermediate level (E1), and upper emitting state (E2) must be approximately equidistant, with E1 possessing a sufficiently long lifetime to act as an effective energy reservoir. Only a few lanthanide ions, such as Er^{3+}, Ho^{3+}, Tm^{3+}, and Nd^{3+}, possess suitable energy level structures for this process.

In contrast, ETU (Figure 3b) involves energy transfer between two distinct ions. A sensitizer ion (typically Yb^{3+}) absorbs the excitation photon and is elevated to a metastable state (E1). It

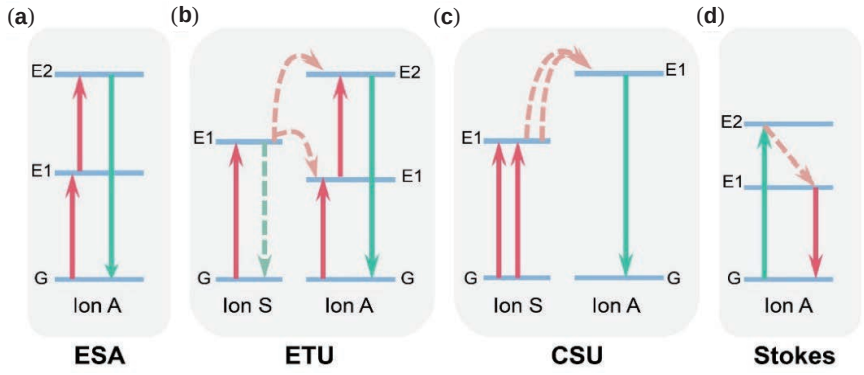

Figure 3 Lanthanide-doped materials exhibit unique optical properties: **a** ESA; **b** ETU; **c** CSU; and **d** Stokes.

subsequently transfers this energy to an activator ion (e.g.,Er^{3+}, Tm^{3+}, or Ho^{3+}), thereby promoting it to a higher-energy emitting state (E2). The efficiency of ETU is critically dependent on the spatial proximity between sensitizer and activator ions, which is controlled by the dopant concentration. Unlike ETU, ESA efficiency is independent of interionic spacing, as all transitions occur within a single ion.

The CSU (Figure 3c) represents a less common but conceptually distinct mechanism, wherein two sensitizer ions are simultaneously excited and jointly transfer energy to a neighboring activator ion, promoting it to an excited state. The activated ion then relaxes radiatively, producing upconverted emission. While CSU is generally orders of magnitude less efficient than ESA or ETU due to its reliance on higher-order, quasi-virtual transitions, it holds promise for high-resolution imaging. Its inherently low efficiency necessitates tightly confined excitation, which can offer advantages in spatial precision not achievable through other UCL mechanisms. CSU has been observed in ion pairs such as Yb^{3+}/Tb^{3+}, Yb^{3+}/Eu^{3+}, and Yb^{3+}/Pr^{3+}.

In contrast to upconversion, downconversion is a Stokes-shifted process, involving the absorption of high-energy photons (e.g., UV or visible) followed by emission at longer wavelengths (Figure 3d). A single ion absorbs a high-energy photon, promoting it to an excited state (E2), from which it may relax non-radiatively to an intermediate level (E1), followed by radiative emission. This process does not require energy transfer between ions and is therefore largely independent of dopant concentration.

Despite their advantageous properties, lanthanide-doped materials face several fundamental limitations. Transitions between 4f states are parity-forbidden and possess low oscillator strengths, resulting in weak absorption and emission. Additionally, the inherently narrow emission bandwidths, while beneficial for multiplexing, reduce photon output relative to conventional fluorophores. These drawbacks are further exacerbated by non-radiative losses arising from multiphonon relaxation, particularly in aqueous environments, where vibrational modes of water molecules and surface defects can significantly quench luminescence. The long-lived excited states of Ln^{3+} ions, though beneficial for time-gated detection, also introduce susceptibility to energy loss via electron-phonon coupling and surface-related quenching pathways. Furthermore, the low molar extinction coefficients of Ln^{3+} severely limit excitation efficiency, posing challenges for applications requiring high brightness. To address these challenges, ongoing efforts focus on engineering the optical performance of lanthanide-doped materials through host lattice optimization, tailoring the local crystal field, surface passivation, engineering energy transfers within lanthanide dopants, surface-plasmon coupling, and sensitization. These strategies aim to enhance quantum yield, mitigate non-radiative losses, and expand the application potential of these materials in complex biological and photonic systems.

3.1 Recent advances in enhancing upconversion efficiency

Recent advances in the highly efficient UCL systems have substantially expanded the potential of lanthanide-doped materials for biomedical applications. Among their photophysical features, enhanced UCL efficiency is particularly crucial, serving as the foundational optical mechanism for enabling high-performance theranostic functionalities, such as deep-tissue imaging, targeted drug delivery, and photodynamic therapy (PDT).

3.1.1 Selection of host materials

Efficient UCL depends critically on the choice of host material. A suitable host lattice should possess low phonon energy, which minimizes non-radiative multiphonon relaxation and enhances radiative emission. Considerable effort has been devoted to the development of high-quality upconversion nanocrystals using a range of synthetic strategies, including co-precipitation [79], thermal decomposition [64], hydrothermal synthesis [80], sol-gel [81], and microwave-assisted synthesis [82]. These methods have facilitated the preparation of diverse host matrices, spanning oxides (e.g., Y_2O_3, zinc oxide (ZnO), and $Yb_3Al_5O_{12}$) [83-85] and fluorides (such as CaF_2, $NaYF_4$, and $KMnF_3$) [86-88]. Among them, fluoride-based hosts have emerged as the most effective, due to their exceptionally low phonon energies, which suppress non-radiative losses from both intermediate and emissive states [89]. In addition to phonon energy, the crystal field environment of the host lattice significantly impacts the upconversion efficiency of doped Ln^{3+} ions. Lower symmetry environments facilitate mixing between 4f and higher-energy configurations, thereby partially lifting parity-forbidden selection rules and enhancing transition probabilities. For instance, hexagonal-phase $NaYF_4$:Yb^{3+},Er^{3+} microcrystals exhibit visible UCL intensities over four times greater than their cubic counterparts [90], and monoclinic ZrO_2 nanoparticles outper-

form their tetragonal analogues in UCL emission [91]. Thus, selecting host materials that combine low phonon energy and low lattice symmetry is fundamental for achieving high upconversion performance.

3.1.2 Tailoring local crystal field

The local crystal environment surrounding Ln^{3+} dopants plays a decisive role in modulating optical transitions (Figure 4a–d). Although host lattice selection determines the global crystal field, further refinement of the local symmetry can be achieved through isovalent or aliovalent doping with non-luminescent ions. These dopants can occupy substitutional or interstitial sites, perturbing the symmetry around Ln^{3+} and enhancing UCL by facilitating otherwise parity-forbidden 4f–4f transitions. Among various dopants, Li^+ ions are especially effective due to their small ionic radius (0.9 Å (1 Å = 1×10^{-10} m)), which allows for facile incorporation into multiple host matrices. Studies by Bai et al. [92,93] and Chen et al. [94] demonstrated that Li^+ doping can enhance UCL in oxide-based nanocrystals by up to two orders of magnitude (Figure 4e). Comparable enhancements have also been reported in fluoride-based systems [82,95]. Moreover, Dou et al. [96] observed significant UCL enhancement in alkali-ion-doped lanthanide fluoride nanoparticles. Incorporation of divalent ions such as Ca^{2+} has also proven highly effective. For example, β-$NaYF_4$:Yb^{3+},Er^{3+} microcrystals doped with 35% Ca^{2+} exhibited green emission intensities over 100-fold greater than Ca^{2+}-free controls (Figure 4f) [97]. Beyond alkali and alkaline-earth ions, transition-metal ion doping has emerged as a powerful strategy. Dopant ions such as Zn^{2+}, Fe^{3+}, Bi^{3+}, and Sc^{3+} possess d orbitals with extended radial distributions, which increase their interaction with the local lattice, promoting enhanced electron-phonon coupling and stronger sensitivity to crystal-field perturbations [98-101]. To better understand upconversion dynamics, it is crucial to address the statistical distribution of dopant ions within individual nanocrystals. In a novel approach, Li et al. [102] reported significant UCL enhancement via interstitial proton (H^+) doping of lanthanide-doped upconversion nanocrystals (UCNs), which introduces local crystal-field asymmetry without altering the crystal phase (Figure 4g). H^+-doped nanocrystals displayed dominant red emission (~654 nm) with red-to-green UCL intensity ratios ranging from 15.6 to 45.8 (Figure 4h). Notably, a 675-fold enhancement in red UCL from Er^{3+} was achieved in orthorhombic $NaMgF_3$:Yb^{3+},Er^{3+} nanocrystals, without increasing particle size (Figure 4i). These findings present an elegant and scalable method for constructing ultrasmall, high-brightness UCNPs, which are particularly suited for optical imaging in biological environments.

Collectively, these advances in local crystal field engineering underscore the importance of both intrinsic and extrinsic structural modulation for maximizing upconversion emission efficiency.

3.1.3 Engineering energy transfers within lanthanide dopants

Non-radiative energy transfer between lanthanide ions primarily proceeds via multipolar or exchange interactions, both of which are highly sensitive to interionic distance. As the spatial separation between dopants is dictated by their concentration within the host lattice [103], precise control over dopant density emerges as a powerful strategy for modulating energy transfer processes and optimizing UCL efficiency. A common approach to improving excitation efficiency is increasing the concentration of sensitizer ions. Chen et al. [104] demonstrated that increasing Yb^{3+} content from 20% to 100% in monodisperse $NaYF_4$:Yb^{3+},Tm^{3+} nanocrystals led to a 43-fold enhancement in 800 nm UCL (Figure 5a). This enhancement was attributed to increased absorption cross-section and more efficient Yb^{3+}→Tm^{3+} energy transfer. However, excessive Yb^{3+} doping (>20%) typically promotes energy migration to surface or lattice defects, resulting in luminescence quenching. To circumvent this, Wang et al. [105] developed orthorhombic KYb_2F_7:Er^{3+} (2%) nanocrystals, where Yb^{3+} ions are spatially organized into tetrad clusters (Figure 5b). This architecture confines excitation energy, dramatically reducing energy loss and enabling intense four-photon violet emission at 410 nm—over eightfold higher than conventional systems (Figure 5c).

High activator ion concentrations (e.g., Tm^{3+},Er^{3+}, or Ho^{3+}) are also essential for maximizing the use of absorbed energy. Zhao et al. [106] showed that increasing Tm^{3+} doping from 0.5% to 8% in $NaYF_4$:Yb^{3+},Tm^{3+} UCNPs under high excitation power led to 5.6-, 71-, and 1,105-fold increases in UCL, respectively. Such ultra-bright UCNPs enable single-particle tracking in live cells [107]. Similarly, highly Er^{3+}-doped sub-10 nm $NaYF_4$:Yb^{3+} nanocrystals maintain strong brightness under increasing excitation, avoiding saturation observed in their 2% Er^{3+} counterparts (Figure 5d) [108]. In Nd^{3+}-doped systems, optimal doping levels were successfully raised from 1% to 20% using indocyanine green (ICG) sensitization, yielding a tenfold enhancement in emission [109]. Fully Er^{3+}-substituted $NaErF_4$@$NaLuF_4$ core-shell nanocrystals demonstrated the highest UCL brightness among a series of Er^{3+}-doped $NaYF_4$ nanocrystals [110].

In addition to lanthanide dopants, host matrix ions can participate in energy transfer. For example, in MnF_2:Yb^{3+},Er^{3+} nanocrystals, energy transfer from Mn^{2+} to Er^{3+} results in preferential population of the $^4F_{9/2}$ level, enhancing red emission relative to green emission [111,112]. Building on these findings, we synthesized $KMnF_3$:Ln^{3+} nanoparticles exhibiting single-band red emission (~660 nm) under 980 nm excitation [88], ideal for deep-tissue bioimaging. Preventing dopant segregation was key to maximizing energy transfer efficiency. Similar red-dominant emission has been reported in $NaMnF_3$ [113] and Mn^{2+}-doped $NaYF_4$ [114].

For lanthanide ions such as Eu^{3+} and Tb^{3+}, which lack intermediate metastable states, UCL can be achieved through energy migration upconversion (EMU). This contrasts with the previously employed CSU (Figure 5e), which is inherently inefficient due to the reliance on quasi-virtual pair levels. Wang et al. [115] introduced a core-shell architecture with Tm^{3+} in the core and Gd^{3+} as a migrating ion across both regions. Excitation energy absorbed by Yb^{3+} is transferred to Tm^{3+}, then relayed to Gd^{3+} (via the $^6P_{7/2}$ state), and finally migrates to surface Eu^{3+} or Tb^{3+} ions, resulting in visible emission (Figure 5f). This approach reduces the excitation power density required for visible UCL to 15 W/cm^2, compared to >10^6 W/cm^2 for CSU.

To address excitation-state energy dissipation, Li et al. [116] designed core-shell-shell (CSS) $NaYF_4$:Yb^{3+},Tm^{3+} nanocrystals

with tunable intermediate layers (1.2–13 nm) (Figure 5g). The sandwich-like architecture spatially confines excitation energy, revealing for the first time a size-dependent long-range energy transfer mechanism in lanthanide-doped systems—challenging the conventional view of size independence. The resulting structure achieved a quantum yield of 13%, surpassing that of bulk materials and offering new directions in nanophotonics and biophotonics.

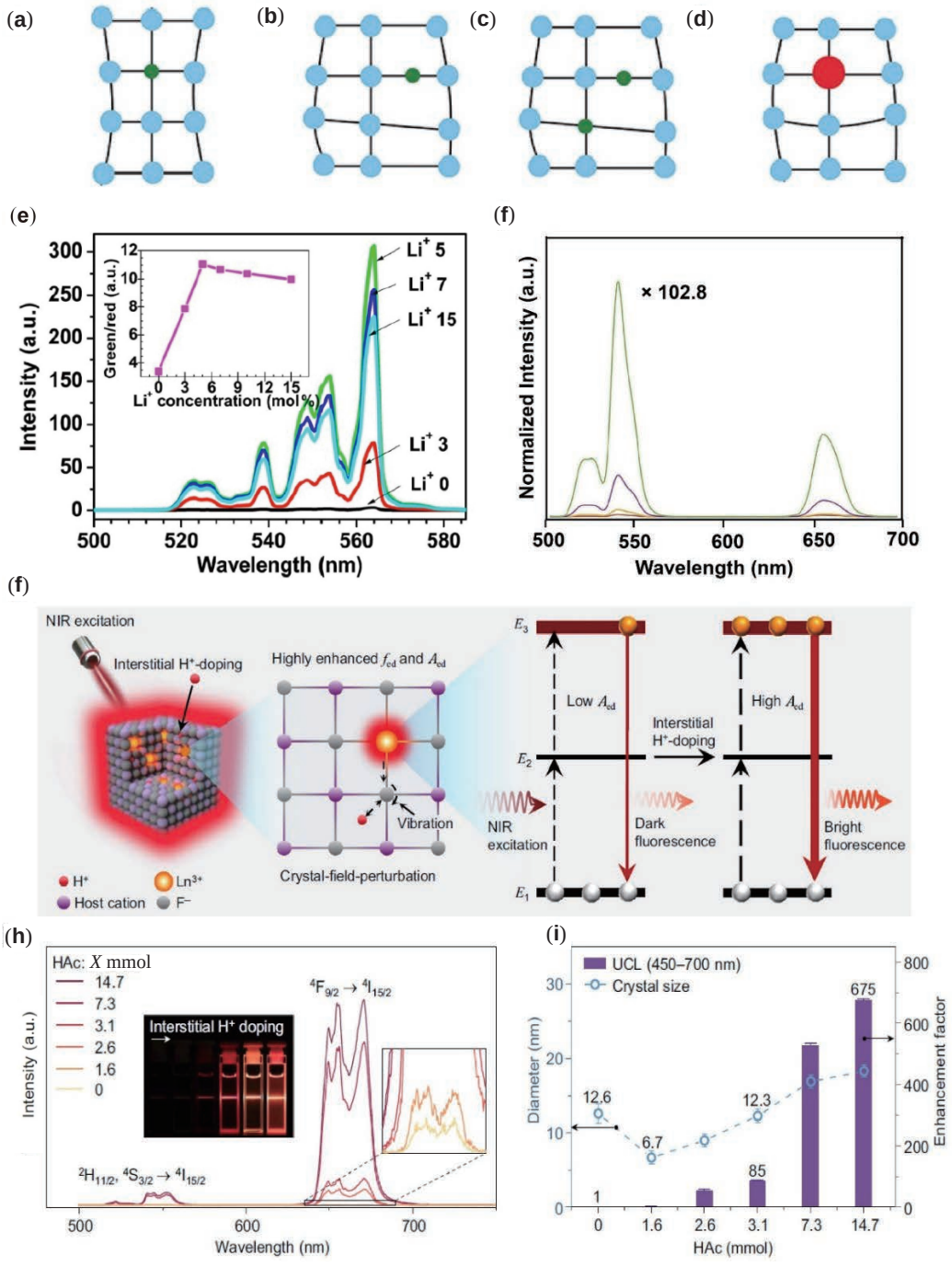

Figure 4 **a.** Substitution by a small atom. **b.** Interstitial occupation by a small atom. **c.** A combination of substitution and interstitial occupation. **d.** Substitution by a big atom. **e.** Measured UC green emission in Y_2O_3 nanocrystals doped with 1 mol% Er^{3+} ions and various Li^+ ions under diode laser excitation of 970 nm. The inset is the intensity ratio of the green to red as a function of Li^+ ions [93]. **f.** UCL spectra of samples β-$NaYF_4$:Yb^{3+},Er^{3+} microcrystals, doping 0%, 10%, 20%, 30%, and 35% Ca^{2+} [97]. **g.** Schematic illustrations of interstitial H^+-doping (left), crystal-field perturbation (middle), and UCL enhancement (right). **h.** Typical UCL spectra of as-synthesized $NaMgF_3$:Yb^{3+},Er^{3+} (NMF-H-X) nanocrystals with different crystal sizes as a function of the nominal amount of acetic acid (HAc) added during the synthetic procedure (X = 0–14.7 mmol). The inset shows corresponding PL images collected using a Canon digital camera. **i.** Evolution of UCL intensity ratio for NMF-H-X NCs and their corresponding crystal sizes as a function of the nominal amount of HAc. The error bars represent the standard deviation of luminescence enhancement factor (purple) and crystal size (blue) [102]. Reproduced with permission from Ref. [93]. Copyright©2008 Elsevier.

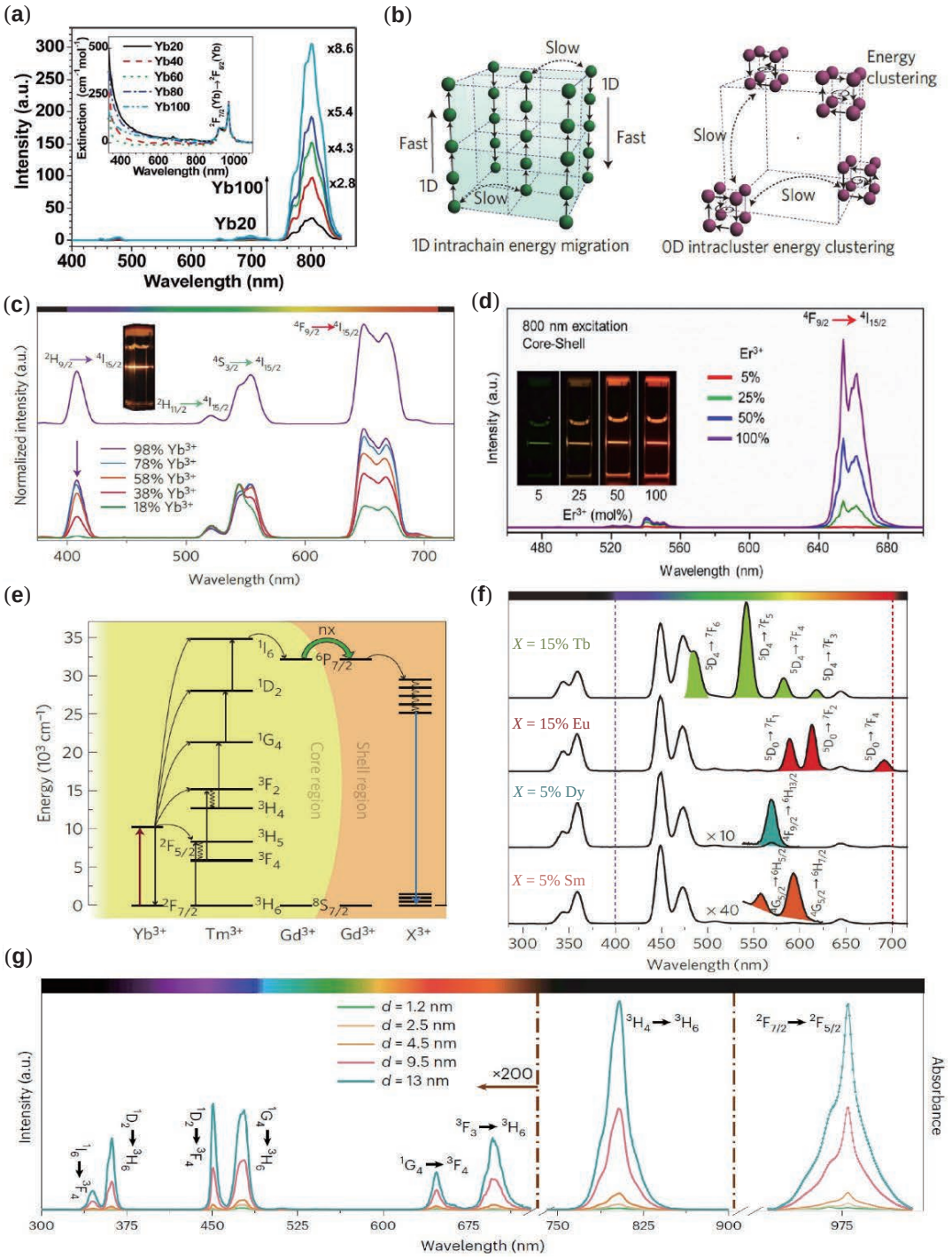

Figure 5 **a.** UCL spectra of colloidal $NaYF_4$ nanocrystals co-doped with 2% Tm^{3+} and various concentrations of Yb^{3+} ions (20%–100%) under diode laser excitation at 975 nm. The absorbance of all samples has been normalized at 975 nm for the $^2F_{7/2}\rightarrow{}^2F_{5/2}$ transition of Yb^{3+} ions, as shown in the inset [104]. **b.** Left: 1D isotropic energy migration; right: 0D intracluster energy clustering. The migration of excitation energy can be effectively minimized by the energy clustering in discrete sublattices. **c.** The upconversion emission spectra of $KYb_2F_7{:}2Er^{3+}$ (top) and $KYb_2F_7{:}2Er^{3+}$,0–80Lu^{3+} (bottom) nanoparticles obtained under a 980 nm laser excitation. Inset: a typical photograph of $KYb_2F_7{:}Er^{3+}$ nanocrystals [105]. **d.** Upconversion spectra of the core-shell nanocrystals with variable Er^{3+} dopant concentrations in the core ($NaYF_4{:}X\ Er^{3+}$, X = 5%, 25%, 50%, and 100%). The inset shows the upconversion emission photos of colloidal dispersion of core-shell nanocrystals showing the enhanced emission with an increase in dopant concentration [110]. **e.** Proposed energy transfer mechanisms in the core-shell nanoparticle. **f.** Emission spectra of the as-prepared $NaGdF_4$@$NaGdF_4$ core-shell nanoparticles doped with different activators (activator emissions are highlighted with color) [115]. **g.** UCL (solid line) and absorbance (line with data-point symbols) spectra of $NaYF_4$@$NaYF_4$:99%Yb^{3+},1%Tm^{3+} (*d*)@$NaYF_4$ CSS nanoparticles (dispersed in hexane) with various thicknesses (*d*); the spectra between 300 and 700 nm are multiplied 200-fold to facilitate comparison with the NIR UCL at 800 nm [116]. Reproduced with permission from Refs. [104,105,110,115,116]. Copyright©2010 American Chemical Society, Copyright©2013 Springer, Copyright©2017 American Chemical Society, Copyright©2011 Springer Nature, and Copyright©2024 Springer Nature.

3.1.4 Suppression of surface-related deactivations

The efficiency of UCL in LnNPs is strongly influenced by surface-related deactivation processes, which are particularly prominent at the nanoscale due to high surface-to-volume ratios. Quenching pathways include direct non-radiative relaxation of surface-adjacent dopants and energy migration from the particle core to surface defects or high-energy vibrational environments (Figure 6a). These loss channels are further exacerbated by surface-bound ligands and aqueous solvents with high phonon energies.

The most widely adopted strategy to suppress surface quenching is the construction of core-shell architectures, where an inert or active shell physically isolates the dopants from the surrounding environment. Three major design principles guide these architectures: (1) identical host materials in the core and shell, (2) heterostructured compositions with matched lattices, and (3) shells doped with functional ions to create active-core/active-shell systems. Homogeneous core-shell systems, such as $NaYF_4$:Yb^{3+},Er^{3+}@$NaYF_4$, benefit from epitaxial growth and reduced interfacial defects. Quintanilla et al. [117] reported 7.4- and 29.6-fold enhancements in UCL from Er^{3+}- and Tm^{3+}-doped $NaYF_4$ nanocrystals, respectively, by depositing a thin (~2 nm) $NaYF_4$ shell. This approach has been extended to other host materials [118,119]. Notably, Wang et al. [120] demonstrated a >450-fold increase in UCL from 10 nm $NaGdF_4$:Yb^{3+},Tm^{3+} nanoparticles coated with a 2.5 nm $NaGdF_4$ shell (Figure 6b and c). Heterostructured core-shell systems, such as $NaYF_4$:Yb^{3+},Er^{3+}@$NaGdF_4$, combine high UCL efficiency with multimodal imaging capabilities, leveraging the MRI contrast properties of Gd^{3+} ions [121,122]. Wang et al. [123] reported a ~300-fold increase in UCL in 10–13 nm $NaYF_4$:Ln^{3+}@CaF_2 nanocrystals (Figure 6d), while Chen et al. [104] achieved a 35-fold enhancement in NIR-to-NIR emission and a quantum yield of 0.6% using a CaF_2 shell on $NaYbF_4$:Tm^{3+} cores at 0.3 W/cm^2 excitation. CaF_2 coatings outperform $NaYF_4$ in resisting aqueous quenching and limiting lanthanide ion leakage [38].

Silica shells, although less effective, have also shown moderate improvements in UCL stability in systems such as Y_2O_3:Yb^{3+}, Tm^{3+} [124], $NaYF_4$:Yb^{3+},Tm^{3+}, or $NaYF_4$:Yb^{3+},Er^{3+} [125] nanoparticles. Systematic investigations of shell thickness in $NaYF_4$:Ln^{3+}@$NaGdF_4$ nanocrystals have confirmed the importance of optimized epitaxial interfaces for luminescence enhancement [126-130].

Finally, active-core/active-shell architectures, where both core and shell are doped with lanthanides, offer enhanced excitation retention and minimized cross-relaxation. Vetrone et al. [131] demonstrated that $NaGdF_4$:Yb^{3+},Er^{3+}@$NaGdF_4$:Yb^{3+} particles significantly outperform both inert-shelled and core-only systems (Figure 6e). Related systems such as $BaGdF_5$@$BaGdF_5$:Yb^{3+} and CaF_2@$NaYF_4$:Yb^{3+} also show superior luminescence due to spatial confinement of energy donors and acceptors [80,132]. These advances highlight the importance of dopant spatial distribution in reducing deleterious energy transfer and enhancing overall UCL efficiency.

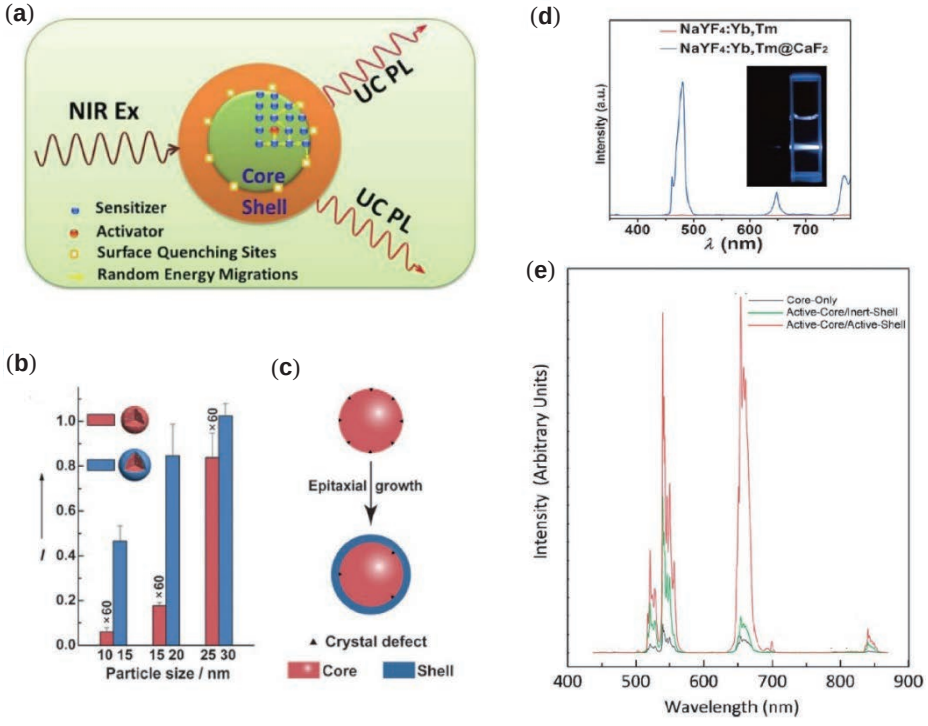

Figure 6 **a.** Schematic illustration of a cross-section of a core-shell structure and random energy migration among lanthanide ions in the core nanoparticles. **b.** Upconversion emission intensity comparison of $NaGdF_4$:$25Yb^{3+}$,$0.3Tm^{3+}$ nanoparticles of different sizes, without and with a thin protection layer, in cyclohexane solutions (4 and 8 mm for core and core-shell particles, respectively). **c.** How surface defects of the core particle may be partially retained as volume defects in the resulting core-shell particles [120]. **d.** UC emission spectra and digital photographs (inset) of $NaYF_4$:Yb, Tm and $NaYF_4$:Yb,Tm@CaF_2 [123]. **e.** UCL spectra of colloidal $NaGdF_4$:Er^{3+},Yb^{3+} (core-only), $NaGdF_4$:Er^{3+},Yb^{3+}/$NaGdF_4$ (active-core/inert shell), and $NaGdF_4$:Er^{3+},Yb^{3+}/$NaGdF_4$:Yb^{3+} (active-core/active-shell) nanoparticles following excitation with 980 nm radiation [119]. Reproduced with permission from Refs. [123,119]. Copyright©2012 Wiley-VCH and Copyright©2008 Wiley-VCH.

3.1.5 Surface-plasmon coupling

Noble-metal nanoparticles have garnered substantial interest owing to their pronounced light absorption and scattering characteristics, particularly in the visible spectral region. Localized surface plasmon resonance (LSPR), arising from the collective oscillations of free electrons in confined metal nanostructures upon resonant interaction with incident photons, leads to the generation of intense, localized electromagnetic fields. These plasmons can propagate along metal surfaces and are capable of effectively concentrating electromagnetic energy at the nanoscale. Consequently, metallic nanostructures have been proposed as potent light-trapping elements that can be coupled with UCNPs to significantly enhance photon-matter interactions and energy conversion efficiency.

The intensity I of UCL from a typical lanthanide-doped nanocrystal can be approximated by the expression:

$$I = \phi \cdot \sigma_s \cdot \eta_{ET} \cdot \varphi_a, \quad (1)$$

where ϕ is the photon flux of the incident light, σ_s is the absorption cross-section of the sensitizer ion, η_{ET} is the energy-transfer efficiency from the sensitizer to the activator, and φ_a is the luminescence quantum yield of the activator. Notably, the direct absorption of the activator is often negligible due to its intrinsically weak absorption cross-section.

Surface plasmons can modulate UCL through three primary mechanisms: (1) enhancement of sensitizer absorption via electric-field coupling, (2) acceleration of the activator's radiative decay rate, and (3) facilitation of energy transfer between sensitizer and activator ions [133]. The local electric field intensity $|E|^2$ associated with LSPR is directly proportional to the photon flux experienced by the UCNPs:

$$\phi \propto |E|^2. \quad (2)$$

As such, the placement of UCNPs in close proximity to metallic nanostructures can significantly amplify excitation efficiency via field enhancement, yielding increased UCL through improved interaction between the plasmonic near-field and the UCNP transition dipoles [134]. The plasmonic response is highly dependent on the structural parameters of the metal nanostructure, including its size, shape, and composition. Optimizing these characteristics is thus essential for maximizing UCL enhancement. Since the first demonstration in 2009—where Ag nanowires were assembled with $NaYF_4$:Yb^{3+},Er^{3+} UCNPs via solvent evaporation—substantial progress has been made in the field of plasmon-enhanced upconversion [135]. Subsequent studies involving silver nanowires [136], single gold nanoparticles [137], and gold island films [138] have reported luminescence enhancement factors of up to 5.

More sophisticated plasmonic architectures have yielded significantly higher enhancement factors. For instance, Paudel et al. [139] employed lithographically defined nanopillar arrays on gold substrates, which exhibited resonant plasmonic behavior matched to the UCNP excitation frequency. Finite-difference time-domain (FDTD) simulations predicted an elevenfold increase in local excitation intensity compared to smooth gold films. Similarly, Saboktakin et al. [140] developed multilayer structures comprising metal, oxide, and UCNP layers, demonstrating that the oxide spacer thickness and metal composition critically influence UCL, with reported enhancement factors of 5.2 for Au and 45 for Ag nanoparticles (Figure 7a).

A particularly remarkable example was demonstrated by Zhang et al. [141], who designed a three-dimensional nanoantenna array consisting of periodic SiO_2 pillars decorated with Au nanostructures. By precisely tuning the pillar height to 75 nm, the plasmon resonance was aligned to 920 nm excitation, resulting in a dramatic 310-fold increase in UCL over a large area (Figure 7b). Beyond field enhancement and radiative rate modulation, surface plasmons can also impact the energy transfer kinetics between lanthanide ions. Sun et al. [142] reported a 6-fold enhancement in energy transfer efficiency from Yb^{3+} to Er^{3+} using engineered gold pyramid arrays (Figure 7c). Their comparative analysis on different substrate morphologies successfully deconvoluted the contributions from electromagnetic field enhancement, quenching effects, and energy transfer dynamics.

In addition to planar and structured substrates, core-shell UCNPs modified with noble metals also exhibit considerable promise, particularly in biological settings where colloidal stability and spatial control are vital. For example, Zhang et al. [143]

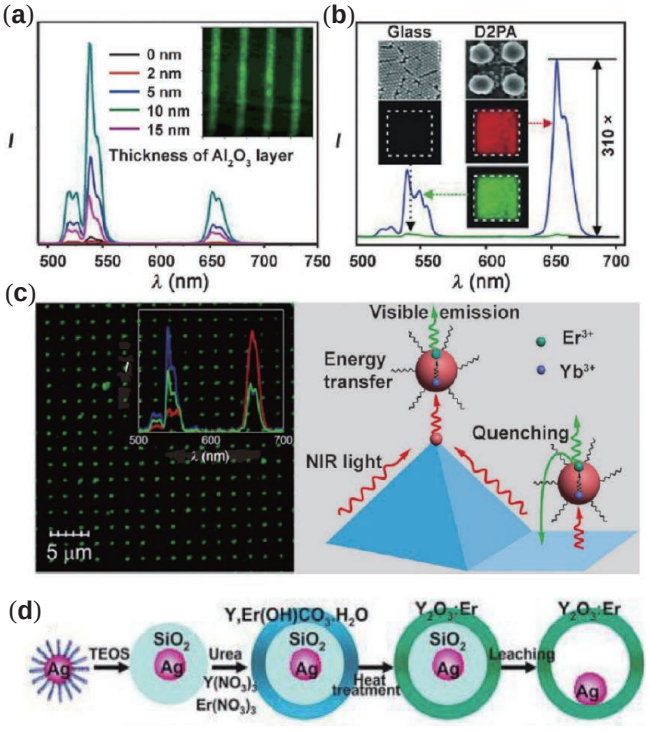

Figure 7 **a.** Green emission enhancement in patterned Au/Al_2O_3/$NaYF_4$:Yb^{3+},Er^{3+} thin films [140]. **b.** Luminescence enhancement in the green (550 nm) and red (660 nm) emission through use of a disk-coupled dot-on-pillar antenna array (D2PA) [141]. **c.** Upconversion emission enhancement using $NaYF_4$:Yb^{3+},Er^{3+} particles coupled with patterned gold pyramids. Left: the confocal image. Inset: corresponding emission spectra of the patterned nanostructures. Right: simplified schematic representation of the energy transfer, upconversion, and quenching processes taking place in the hybrid system [142]. **d.** Synthetic procedure of the Ag@SiO_2@Y_2O_3:Er^{3+} nanostructures [143]. Reproduced with permission from Refs. [140-142]. Copyright©2012 American Chemical Society, Copyright©2012 Wiley-VCH, and Copyright©2014 American Chemical Society.

optimized the silica spacer thickness in $Ag@SiO_2@Y_2O_3:Er^{3+}$ structures to achieve a fourfold emission enhancement (Figure 7d). Ge et al. [144] further validated the efficacy of this configuration by demonstrating a 9.5-fold increase in green emission (~549 nm) from $Au@SiO_2@Y_2O_3:Yb^{3+},Er^{3+}$ nanoparticles, using a 30 nm gold core.

3.1.6 Dye-sensitized upconversion

The inherently low absorption cross-sections of Ln^{3+} ions, stemming from parity-forbidden 4f–4f transitions, significantly limit their ability to harvest excitation light directly. To address this fundamental constraint, organic dyes with broadband and tunable absorption profiles—exhibiting absorption cross-sections several orders of magnitude greater than those of lanthanide ions—have been extensively employed as sensitizers in dye-functionalized UCNPs systems [145,146].

Zou et al. [147] demonstrated that a carboxyl-modified cyanine dye (IR-806), when anchored in close proximity to $NaYF_4:Yb^{3+}$, Er^{3+} UCNPs, acted as an effective molecular antenna (Figure 8a). The dye harvested NIR light over a broad spectral window (740–850 nm), and subsequently transferred energy to the Yb^{3+} ions via a Förster resonance energy transfer (FRET) mechanism. This strategy enabled a substantial 3,300-fold enhancement in UCL intensity over the 720–1,000 nm excitation range (Figure 8a), attributed to the broadened absorption spectrum and improved light-harvesting efficiency of the hybrid system. Building on this, Garfield et al. [103] showed that increasing the Gd^{3+} content in the UCNPs host matrix modulated the excited-state dynamics of IR-806, promoting intersystem crossing (ISC) from the singlet (S_1) to the triplet (T_1) state. This shift aligned the dye's T_1 energy more closely with that of Yb^{3+} acceptor ions, enabling more efficient energy transfer and resulting in an extraordinary 33,000-fold enhancement in UCL brightness (Figure 8c and d).

To overcome the spectral mismatch between NIR dye emission and Yb^{3+} absorption, Chen et al. [148] developed an energy-cascaded architecture based on a core-shell structure, $NaYbF_4$:0.5% $Tm^{3+}@NaYF_4:Nd^{3+}$. In this design, the outer Nd^{3+}-doped shell absorbed 800 nm photons and transferred energy through a stepwise process to the inner core, enabling efficient multiphoton upconversion (Figure 8e). This configuration yielded an upconversion quantum yield of 4.8%—approximately 100-fold higher than typical yields reported for 800 nm-excited lanthanide nanostructures—and significantly reduced surface-induced quenching, a common issue in dye-sensitized core-only particles.

In a complementary approach, Zhang et al. [149] exploited the heavy atom effect of cesium and lutetium within $CsLu_2F_7:Yb^{3+}$, Er^{3+} nanocrystals to promote ISC in IR808 dye molecules anchored to the nanocrystal surface. This strategy achieved an ISC efficiency of 99.3% from S_1 to T_1 (Figure 8f) and led to a 1,309-fold enhancement in luminescence compared to unmodified $CsLu_2F_7:Yb^{3+},Er^{3+}$ nanocrystals. Notably, this enhancement was an order of magnitude higher than that observed in IR808-modified $NaYF_4:Yb^{3+},Er^{3+}$ systems under identical conditions. To further mitigate the interfacial energy transfer barrier between organic dyes and Yb^{3+} ions, Zhao et al. [150] tailored the dye structure by modifying the coordination sites within the π-conjugated backbone and minimizing the donor-acceptor distance inside the UCNPs framework. Using sulfonated indocyanine green (disulfo-ICG) as the antenna dye, they achieved a 2,413-fold increase in UCL intensity under 808 nm excitation compared to conventional UCNPs excitation at 980 nm (Figure 8g and h). This remarkable enhancement was attributed to a 72.1% energy transfer efficiency from the triplet state of disulfo-ICG to Yb^{3+} ions. The reduction in dye-to-ion distance, coupled with the enhanced heavy atom effect, increased the T_1-state population and significantly improved T_1-state-mediated upconversion performance.

In total, these advancements highlight the transformative potential of dye-sensitized strategies in addressing the intrinsic limitations of lanthanide photophysics, enabling broadband, high-efficiency upconversion systems with promising applications in biophotonics, sensing, and photovoltaics.

3.2 Strategies to boost downconversion luminescence

Lanthanide-doped materials possess unique DCL properties that make them highly suitable for biomedical imaging in the second NIR window (NIR-II, 1,000–1,700 nm). These materials are capable of efficiently converting high-energy photons into longer-wavelength emissions in the NIR-II region, enabling deeper tissue penetration owing to reduced photon scattering and absorption by biological tissues at these wavelengths. Moreover, the intrinsically sharp and narrow emission lines of Ln^{3+} ions help minimize spectral overlap and background interference, significantly improving the signal-to-noise ratio. Their high photostability and negligible autofluorescence further enhance imaging precision, making them attractive candidates for high-contrast, deep-tissue imaging.

Despite these advantages, the luminescence efficiency of LnNPs in the NIR-II region remains suboptimal, posing a key challenge for their broader application in bioimaging and theranostics. Efforts to improve NIR-II emission efficiency have primarily focused on three main strategies: tailoring the host matrix, mitigating luminescence quenching, and enhancing photon absorption. This section emphasizes the first two aspects, specifically exploring the rational design of host materials and structural modifications aimed at boosting DCL performance.

3.2.1 Host matrices

The choice of host matrix plays a critical role in determining the local crystal field environment of embedded lanthanide ions. By carefully tuning the lattice structure and symmetry, one can manipulate the probability of 4f–4f transitions, thereby modulating emission intensity and wavelength. The introduction of non-luminescent dopants into the host lattice can disrupt crystal field symmetry, leading to enhanced radiative transition probabilities [151-153].

Zhong et al. [154] reported the development of Zn-doped α-$NaYbF_4:Ln^{3+}$ nanoparticles, in which Zn^{2+} incorporation significantly modulated the crystal field and promoted multiphonon relaxation (Figure 9a). This strategy yielded an order-of-magnitude DCL enhancement in NIR-II compared with undoped analogues (Figure 9b and c). Similarly, incorporating Zr^{4+} into β-$NaGdF_4:Ln^{3+}$ led to a comparable increase in

luminescence efficiency. To further enhance DCL in the NIR-IIb region (1,500–1,700 nm), Zhong et al. [155] engineered a core-shell architecture comprising $NaYbF_4$:2%Er,2%Ce@$NaYF_4$. The introduction of Ce^{3+} as a co-dopant facilitated nonradiative energy relaxation of the Er^{3+} from $^4I_{11/2}$ to $^4I_{13/2}$ levels, resulting in a pronounced increase in population of the $^4I_{13/2}$ state and yielding strong emission at 1,550 nm. The quantum yield of this erbium-based rare-earth nanoparticle (Er-LnNPs) system reached up to 2.73%, a considerable improvement over conventional formulations (Figure 9d–f).

In a parallel effort, Yang et al. [156] revealed that the cubic-phase α-$NaLnF_4$ matrix, in contrast to its hexagonal-phase β-$NaLnF_4$ counterpart, markedly enhanced the DCL of Tm^{3+}-doped probes. The α-phase matrix enabled nearly two orders of magnitude improvement in emission intensity at 1,632 nm (Figure 9g). This enhancement was attributed to the higher phonon energy of the α-phase structure, which facilitated efficient nonradiative relaxation from the $^3H_4$ to the $^3F_4$ level of Tm^{3+}, increasing electron population at the emissive $^3F_4$ level (Figure 9h). Additionally, enhanced cross-relaxation among Tm^{3+} ions and more effective energy transfer processes between sensitizers and activators within the α-phase matrix contributed to the observed luminescence intensification.

This matrix engineering strategy has also been extended to other lanthanide ions, such as Er^{3+} and Ho^{3+}, producing emission bands centered at 1,530 and 1,180 nm, respectively. These findings highlight the potential of α-phase rare-earth fluorides in enabling multi-channel NIR-II imaging with improved brightness and wavelength versatility. In particular, the Tm^{3+}-based probes emitting at 1,632 nm offer promising avenues for deep-tissue imaging applications and for the design of multiplexed fluorescence imaging systems operating in the NIR-IIb region.

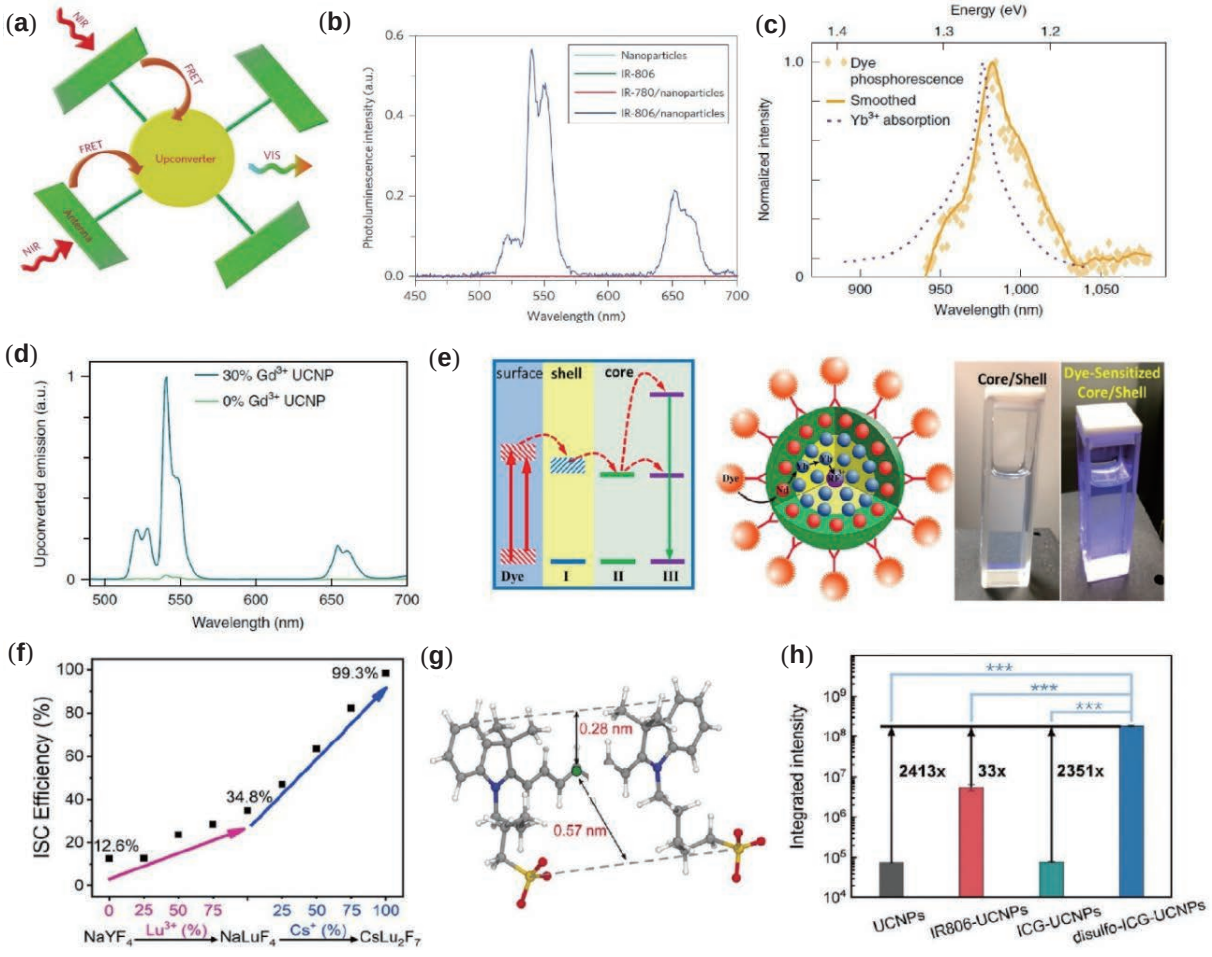

Figure 8 **a.** Principal concept of the dye-sensitized nanoparticle. **b.** Steady-state emission spectra of $NaYF_4$:Yb^{3+},Er^{3+} nanoparticles (cyan line, no spectrum produced), IR-806 (green line, no spectrum produced), $NaYF_4$:Yb^{3+},Er^{3+} nanoparticles/IR-780 (red line), and $NaYF_4$:Yb^{3+},Er^{3+} nanoparticles/IR-806 (blue line) in $CHCl_3$ excited by a 2 mW, 800 nm laser [147]. **c.** Time-gated triplet phosphorescence spectrum of IR806 on $NaGdF_4$ nanoparticles at 80 K (no Yb^{3+} or Er^{3+} present), overlaid with the NIR portion of the UCNPs absorption spectrum (at room temperature). **d.** Upconverted emission from dye-sensitized UCNPs with 30% Gd^{3+} (blue line) and with 0% Gd^{3+} (green line) [103]. **e.** Scheme of energy-cascaded upconversion in dye-sensitized fluoride core-shell nanocrystals [148]. **f.** ISC efficiency of the IR808 on the surface of a series of NCs from $NaYF_4$ to $CsLu_2F_7$ with different concentrations of Lu^{3+} and Cs^+ [149]. **g.** The optimized geometry for Cy7 coordinated to Yb^{3+}. The lengths marked by the black arrows indicated the distance between the fluorescence core and the surface of UCNPs. **h.** The integrated intensity of UCNPs and dye-UCNPs upon excitation at 980 and 808 nm, respectively [150]. Reproduced with permission from Refs. [103,147-150]. Copyright©2012 Springer Nature, Copyright©2018 Springer Nature, Copyright©2015 American Chemical Society, Copyright©2021 Wiley-VCH, and Copyright©2023 Wiley-VCH.

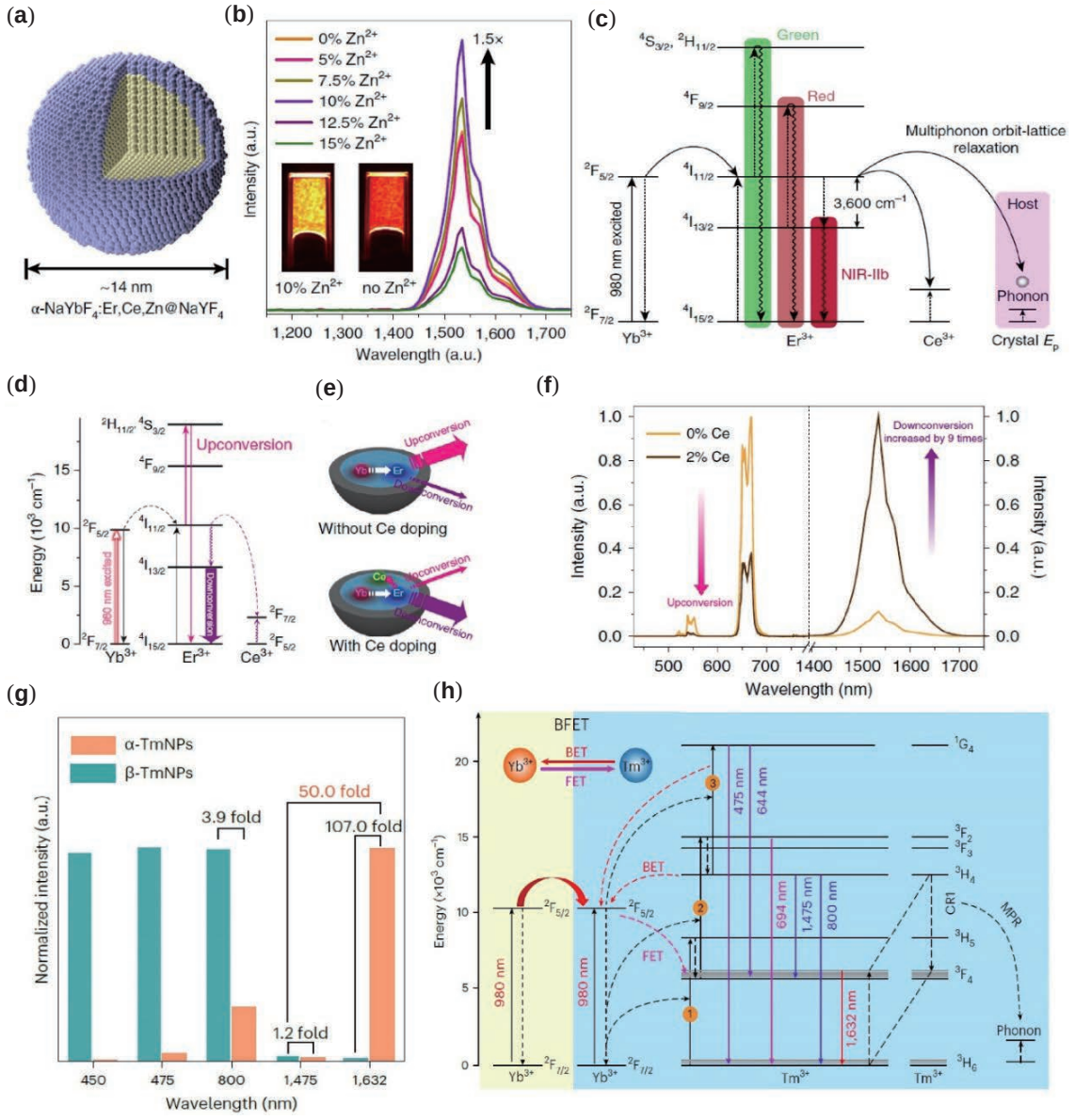

Figure 9 **a.** Schematic design of core-shell Zn-doped α-ErNPs. **b.** DCL spectra of Zn-doped α-ErNPs with different Zn^{2+} concentrations (0%, 5%, 7.5%, 10%, 12.5%, and 15%, nominal doping concentration). The insets show NIR-IIb luminescence images of α-ErNPs with 10% and 0% Zn^{2+} doping. **c.** Simplified energy-level diagrams depicting the energy transfer involved in α-ErNPs on 980 nm excitation [154]. **d.** Simplified energy-level diagrams depicting the energy transfer between Yb^{3+},Er^{3+}, and Ce^{3+} ions. **e.** Schematic illustration of the proposed energy-transfer mechanisms in Er-LnNPs with and without Ce^{3+} doping. **f.** Upconversion and DCL spectra of the Er-LnNPs with 0% and 2% Ce^{3+} doping [155]. **g.** Typical luminescence emission intensities in the visible and NIR regions of α-TmNPs and β-TmNPs under 980 nm laser excitation. **h.** Proposed energy transfer mechanism of NIR-IIb fluorescence amplification in α-TmNPs [156]. Reproduced with permission from Refs. [154,156]. Copyright©2019 Springer Nature and Copyright©2023 Springer Nature.

3.2.2 Surface defect suppression

Epitaxial growth of inert shells is a widely adopted strategy to mitigate surface defect-induced quenching and enhance NIR DCL efficiency in lanthanide-doped nanocrystals. Various host materials, including $NaYF_4$, $NaLuF_4$, $NaGdF_4$, and CaF_2, have been systematically investigated as shell candidates with tunable thicknesses [110,157]. For instance, Zhong et al. [155] optimized the $NaYF_4$ shell thickness on $NaYbF_4$:Er^{3+},Ce^{3+}@$NaYF_4$ core-shell nanocrystals, identifying an optimal thickness of ~7 nm for maximal NIR-II DCL intensity. However, the ideal shell thickness is not universal and varies across compositions. A 13.2 nm $NaLuF_4$ shell was reported as optimal for $NaErF_4$:Ce^{3+}@$NaYbF_4$, while a thinner 3.6 nm $NaYF_4$ shell was sufficient for $NaErF_4$ [158]. In a comparative study, Li et al. [159] evaluated a series of α- and β-phase $NaErF_4$@$NaLnF_4$ (Ln = Y, Lu, Gd) structures and found $NaYF_4$ to be the most effective shell material for enhancing DCL. They demonstrated that a 3 nm shell could substantially suppress surface quenching, achieving an absolute quantum yield of ~10.2% under 808 nm excitation at 0.1 W/cm^2. More recently, Mi et al. [160] developed $NaYbF_4$:Er^{3+},Ce^{3+},Zn^{2+} core nanocrystals coated with a CaF_2 shell. Increasing particle size from 19.1 nm to 80.9 nm led to a marked

rise in absolute quantum yield at ~1,530 nm from 21.6% to 48.6%. Beyond improving emission efficiency, core-shell architectures also permit higher doping concentrations of activator ions, previously limited by nonradiative cross-relaxation. Johnson et al. [110] demonstrated that increasing Er^{3+} content in $NaErF_4$@$NaLuF_4$ nanocrystals enhanced DCL intensity under 808 nm excitation, challenging the longstanding notion that high activator concentration inevitably leads to luminescence quenching. These results highlight the critical importance of rational shell design in optimizing LnNPs for high-performance NIR-II imaging.

3.2.3 Sensitizer

1) Ion sensitization

Conventional Lanthanide-doped downconversion materials typically comprise a host lattice and activator ions. However, the narrow absorption cross-sections of Ln^{3+} ions—attributed to parity-forbidden 4f–4f transitions—limit excitation efficiency. Incorporating sensitizers with stronger light absorption and efficient energy transfer to activators is thus essential. Common sensitizers include lanthanide ions (e.g., Yb^{3+}, Nd^{3+}, Cr^{3+}), organic dyes, and QDs.

Yb^{3+} ions, with a strong absorption transition at 980 nm ($^2F_{7/2} \rightarrow {}^2F_{5/2}$), are widely used in both upconversion and downconversion processes [161]. Li et al. [162] developed a CSS architecture—$NaErF_4$@$NaYbF_4$@$NaYF_4$—which spatially separates the Er^{3+} activator and Yb^{3+} sensitizer. This structure enables higher activator doping levels and delivers a NIR-II absolute quantum yield of 18.7% under 980 nm excitation. Nevertheless, 980 nm excitation is suboptimal for biological imaging due to strong water absorption in this range, which can cause local overheating [163]. Nd^{3+} ions offer an attractive alternative due to their higher absorption cross-section at 808 nm ($^4I_{9/2} \rightarrow {}^2F_{5/2}$), a biologically safer excitation window [164]. Chen et al. [165] demonstrated NIR-II emissions at 1,050 and 1,330 nm from $NaGdF_4$:Nd^{3+}@$NaGdF_4$, achieving absolute quantum yields of 40% and 20% in hexane and water, respectively. Jiang et al. [166] further advanced the field by proposing a co-sensitization strategy involving Ho^{3+} and Nd^{3+} as sensitizers, Yb^{3+} as the energy transfer mediator, and a range of activators (e.g., Er^{3+}, Ho^{3+}, Pr^{3+}, Tm^{3+}). The resulting nanocrystals exhibited ultrabroadband excitation (350–850 nm) and strong NIR-II emission at 1,527 nm (Figure 10a). Ming et al. [167] introduced Cr^{3+}-sensitized LnNPs, which offer high absorption efficiency owing to Cr^{3+} ions' large molar extinction coefficient—14-fold higher than that of Yb^{3+} ions (Figure 10b). These Cr^{3+}-based fluoride nanostructures, featuring low phonon energy, serve both as hosts and sensitizers (Figure 10d), achieving for the first time nanoscale Cr^{3+}-mediated sensitization of six different Ln^{3+} activators with emissions spanning 900–1,700 nm. Their brightness exceeds that of conventional Yb^{3+}-sensitized nanoparticles by up to 370-fold (Figure 10c). Other transition metals, such as Mn^{2+} and Ni^{3+}, also exhibit promising sensitization capabilities, pointing to a broader, generalizable principle of transition-metal-mediated luminescence enhancement.

2) Quantum dots sensitization

Semiconductors have historically served as hosts for lanthanide ions, with early studies in the 1980s and 1990s exploring systems such as InP:Yb^{3+}, GaAs:Er^{3+}, and GaP:Nd^{3+} [168,169]. Recent advances have extended these systems to the QD regime [170-173]. However, weak interactions between Ln^{3+} ions and semiconductor lattices often limit doping concentrations and energy transfer efficiency [170]. To overcome these limitations, strategies such as surface grafting or constructing core-shell structures with QDs as the core and LnNPs as the shell have been explored. Zhang et al. [174] functionalized $NaYF_4$:Yb^{3+},Er^{3+} with Ag_2S QDs, leading to a ~10-fold increase in brightness and 17-fold enhancement in NIR-II emission at 1,550 nm. Swabeck et al. [175] developed InP@$LnXY_{1-x}F_3$@ShF_3 nanostructures (Ln = Yb^{3+}, Nd^{3+}; Sh = Lu^{3+}, Y^{3+}), in which InP QDs broadened visible light absorption while maintaining narrow-band emission from Yb^{3+} and Nd^{3+}, offering a viable strategy for LnNPs-based bioprobes.

3) Dye sensitization

Organic dyes offer broad and tunable absorption spectra and exhibit absorption cross-sections that are typically three orders of magnitude larger than those of Ln^{3+} ions, making them highly efficient energy donors. Among these, cyanine dyes are most widely employed. Shao et al. [176] constructed an organic–inorganic hybrid system by coating $NaYF_4$:Yb^{3+},Ln^{3+}@$NaYbF_4$@$NaYF_4$:Nd^{3+} nanoparticles with ICG, extending excitation from 700 nm to 860 nm with a Stokes shift >200 nm. This architecture yielded approximately fourfold enhancement in NIR-II emission across various lanthanides, including Nd^{3+} (1,060 nm), Ho^{3+} (1,165 nm), Pr^{3+} (1,310 nm), Tm^{3+} (1,460 nm), and Er^{3+} (1,530 nm), marking it as a versatile imaging platform.

Wang et al. [177] reported a fivefold increase in Er^{3+} emission at 1,520 nm using ICG. Other cyanine dyes, such as IR-808 [178,179] and IR-3C [180], have shown similar efficacy. Wang et al. [181] developed Alk-pi as a highly efficient antenna dye, achieving a 40-fold enhancement in NIR-II emission and enabling dynamic real-time vascular imaging. Wang et al. [182] proposed a novel sensitization strategy using bacterial chlorophyll as the antenna ligand for Er^{3+} ions (Figure 10e). The system exhibited a highly efficient triplet energy transfer (TET) mechanism, producing sharp NIR emission (half-width <32 nm) and a substantial Stokes shift of 760 nm (Figure 10f). This innovation enables high-resolution, multiplexed *in vivo* fluorescence imaging and expands the toolkit for biological sensing in the NIR-II window.

Furthermore, recent advancements have focused on optimizing dye sensitization for pure Er^{3+} systems and extending the approach to molecular complexes. For instance, to overcome the poor intrinsic absorption and surface quenching of small nanocrystals, Zhao et al. [183] demonstrated a direct energy transfer strategy from a surface dye to the Er^{3+} ions in sub-10 nm $NaErF_4$ nanoparticles, leading to simultaneous enhancement of both upconversion and NIR-II downconversion emission (1,530 nm). Beyond inorganic nanoparticles, molecular-based Erbium(III)-Phthalocyanine complexes (ErPc) have emerged as promising emitters [184]. By carefully tuning the electronic symmetry of the complex, the phthalocyanine ligand functions as an efficient antenna, enabling NIR-II emission beyond 1,500 nm (e.g., 1,550 nm) with an ultra-narrow bandwidth (<10 nm) and high quantum yield, which is ideal for high-resolution *in vivo* biosensing.

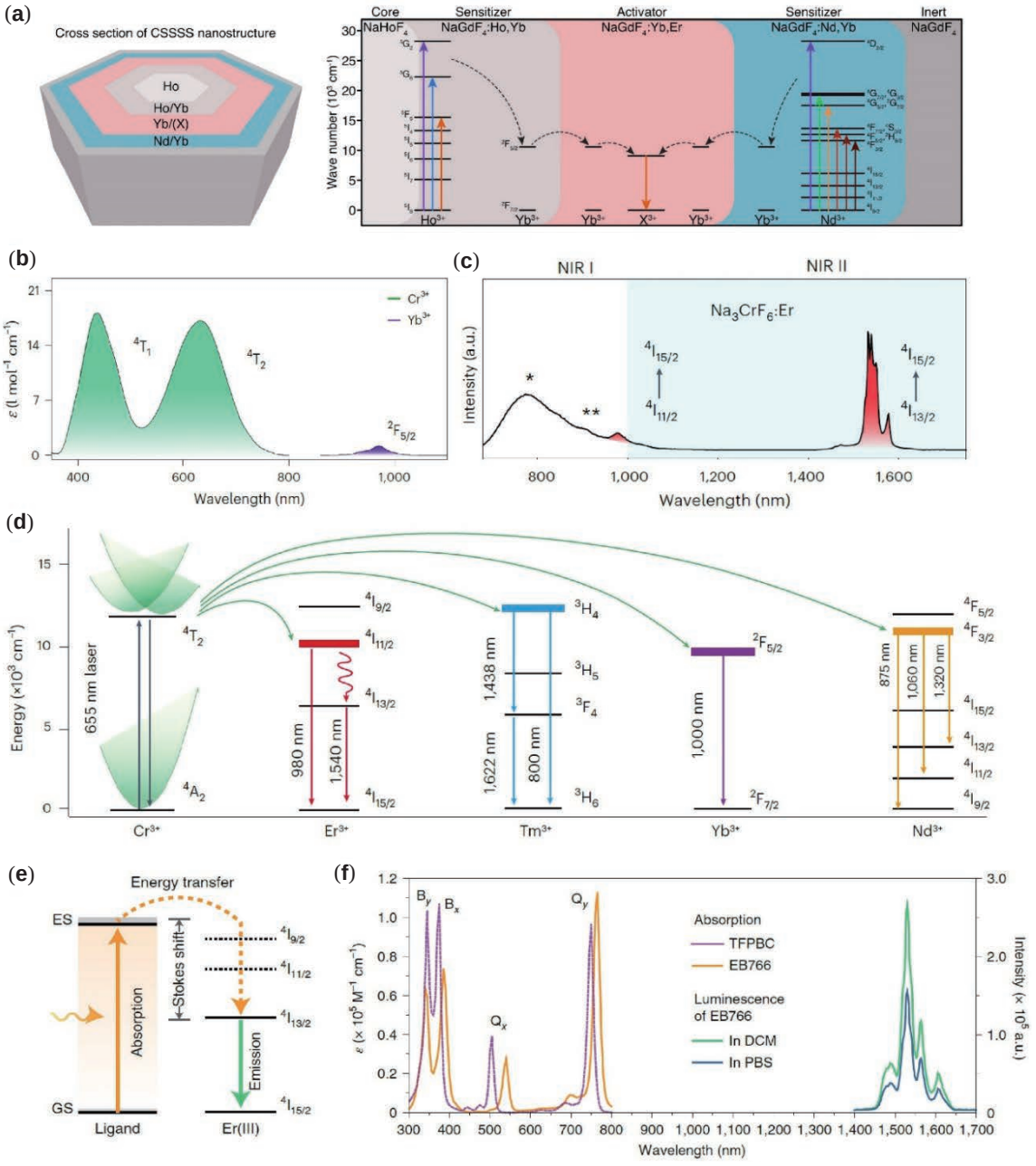

Figure 10 **a.** Illustrated cross-section of prepared CSSSS with symmetric penta-layer core-shell structure (X = Er, Ho, Pr, and Tm) [166]. **b.** Molar extinction coefficients of Cr^{3+} and traditional sensitizer ion (Yb^{3+}) in aqueous solutions. **c.** Luminescence emission spectra of Na_3CrF_6:Er (4.2 mol%) nanoparticles under 655 nm laser excitation (NIR-I, 700-1,000 nm). **d.** Proposed mechanism of efficient sensitization from Cr^{3+} to X^{3+} (X = Er, Tm, Yb, and Nd) [167]. **e.** Simplified diagram showing the luminescence sensitization of an Er(III) complex: ligand absorption, followed by energy transfer and metal-centered emission. **f.** Absorption spectra of TFPBC and EB766 in DCM (left) and the emission spectra of 10 μM EB766 in DCM and PBS (pH 7.4) under 760 nm excitation in the range from 1,400 nm to 1,700 nm (right). The emission spectra measurements were replicated three times. ε, molar extinction coefficient [182]. Reproduced with permission from Refs. [167,182]. Copyright©2024 Springer Nature and Copyright©2021 Springer Nature.

4. Biological applications

Lanthanide-doped luminescent materials are able to produce tunable anti-Stokes shift UCL and NIR downconversion emission, along with long luminescence lifetimes, narrow emission peaks, and stable fluorescence emission [185]. These unique spectral and optical properties endow them with highly promising properties for biological applications, particularly in bioimaging and biosensing, providing valuable tools for precision medicine and biomedical research.

4.1 Imaging and sensing

Bioimaging and sensing based on optical signals enable efficient

and accurate monitoring of physiological activities and dynamic changes in biomolecules, making them essential tools for non-invasive monitoring and disease diagnosis [186]. Currently, cutting-edge research on lanthanide-doped luminescent materials in the fields of biosensing and imaging encompasses critical areas such as nanothermometry, super-resolution imaging, and nano-mechanical sensing. This review will focus on these three applications and discuss how lanthanide-doped luminescence can offer innovative solutions in these fields.

4.1.1 *In vivo* imaging

LnNPs have become highly advantageous probes for *in vivo* optical imaging owing to their distinctive photophysical properties and exceptional performance in complex biological environments. Their defining features include large Stokes shifts, ultranarrow emission bandwidths, long emission lifetimes, and outstanding resistance to photobleaching, all of which contribute to high signal fidelity and minimal background interference [2,4]. Critically, many rare-earth fluorophores operate in the NIR (700–3,000 nm) spectral region, where reduced tissue absorption, diminished scattering, and suppressed autofluorescence enable superior penetration depth and enhanced imaging contrast, making them particularly well suited for deep-tissue visualization.

A unique property of lanthanide-based nanocrystals is their ability to exhibit UCL, in which multiple low-energy NIR photons are absorbed and converted into higher-energy emission (anti-Stokes shift). This allows excitation with tissue-penetrant NIR light while generating visible or NIR emission with low background noise, and has positioned UCNPs as valuable tools for high-contrast *in vivo* imaging and multimodal bioimaging platforms [22,23].

However, despite these advantages, upconversion imaging is increasingly being surpassed by direct NIR-region imaging—particularly in the NIR-II window—for deep-tissue applications. The intrinsic nonlinear nature of the upconversion process results in relatively low quantum efficiency and requires high excitation power densities, often at 980 nm, which can induce undesirable photothermal heating and compromise tissue safety during prolonged imaging [25]. Moreover, the upconversion emission is frequently located in the visible or NIR-I region (400–900 nm), where photon scattering and absorption by biological tissues remain substantial, limiting achievable penetration depth and spatial resolution. In contrast, DS emissions in the NIR-II region occur under lower excitation power, offer higher brightness and stability, and experience significantly reduced scattering, thereby affording clearer images with higher signal-to-noise ratios in deep biological tissues [2,5,187]. These considerations have driven a paradigm shift toward NIR-II-based imaging as the dominant strategy for high-performance *in vivo* visualization.

The NIR-II and its extended subregions (NIR-IIb/c, 1,500–3,000 nm) represent a transformative domain for *in vivo* imaging, offering unprecedented penetration depth and spatial resolution that surpass those achievable with both visible and upconversion-based approaches [188,189]. In this context, DS rare-earth nanocrystals have been intensively engineered to maximize emission within these biologically optimal windows.

For instance, Zhong et al. [155] synthesized Er/Ce co-doped $NaYbF_4$ nanocrystals, in which Ce^{3+} ions suppressed upconversion pathways while significantly enhancing downconversion emission at 1,550 nm (NIR-IIb), enabling rapid and high-resolution imaging of cerebral vasculature in live mice. Complementarily, Zhang et al. [190] developed Tm^{3+}-sensitized nanocrystals with both excitation and emission located in the NIR-II window (1,208 nm excitation, 1,525 nm emission), facilitating time-gated, high-fidelity *in vivo* optical information storage and decoding. Further advances have extended imaging capabilities into the NIR-IIb/c regime. Chang et al. [191] reported Tm^{3+} self-sensitized nanocrystals exhibiting bright emission in the 1,600–2,100 nm range under 800 nm excitation, achieving quantum yields suitable for deep-tissue bioimaging. Yu et al. [192] enhanced these performances by introducing cascade Nd^{3+}-sensitized energy transfer in highly Tm^{3+}-doped systems, attaining quantum yields exceeding 23% in the NIR-IIb/c region, which affords high-resolution whole-body imaging with exceptional clarity. Innovative structural engineering has also facilitated sophisticated functional imaging. Yang et al. [156] introduced cubic-phase Tm-based nanoparticles ($NaYF_4$:Yb^{3+},Tm^{3+}@$NaYbF_4$@$NaYF_4$) with amplified 1,632 nm emission, which, when integrated with Er^{3+}-doped nanocrystals (Figure 11a and b), facilitated non-invasive real-time multiplexed imaging of cerebrovascular dynamics. In parallel, Ho^{3+}-sensitized nanocrystals ($NaYF_4$:Ho^{3+},Ln^{3+}@$NaYF_4$) developed by Wang et al. [193] provided tunable emission spanning 1,000–2,200 nm under 1,143 nm excitation, further expanding the spectral versatility for deep-tissue visualization (Figure 11c and d).

Collectively, these developments illustrate that while upconversion imaging retains niche utility, particularly for background suppression and multimodal systems, NIR-II DS imaging offers a more favourable balance of penetration depth, spatial resolution, brightness, and biosafety. As a result, NIR-II-emissive rare-earth nanomaterials have emerged as the dominant platform for advanced *in vivo* imaging, reinforcing their central role in next-generation biomedical diagnostics, including vascular mapping, tumor visualization, neurological imaging, and real-time physiological monitoring.

4.1.2 Nanothermometry

Temperature is a vital parameter that regulates numerous biological processes, including metabolic activity, gene expression, immune responses, cell proliferation, and apoptosis [194]. As a result, accurate temperature sensing has attracted increasing attention in biomedical research [195]. Lanthanide-doped luminescent nanothermometers, which exploit the sensitivity of 4f electron transitions to temperature-dependent radiative and non-radiative relaxation, have become a rapidly growing area of study [196-198]. By integrating nanotechnology with optical sensing techniques, these nanothermometers offer highly sensitive, submicron-resolution temperature measurements with real-time feedback [199].

From a mechanistic perspective, the temperature sensitivity of LnNPs primarily originates from thermally induced population redistribution between thermally coupled excited states and the modulation of non-radiative relaxation processes [199]. In typical Er^{3+}-doped systems, the closely spaced levels $^2H_{11/2}$ and $^4S_{3/2}$ are separated by approximately 700–900 cm^{-1}, allowing thermal equilibrium to be established. According to Boltzmann statistics,

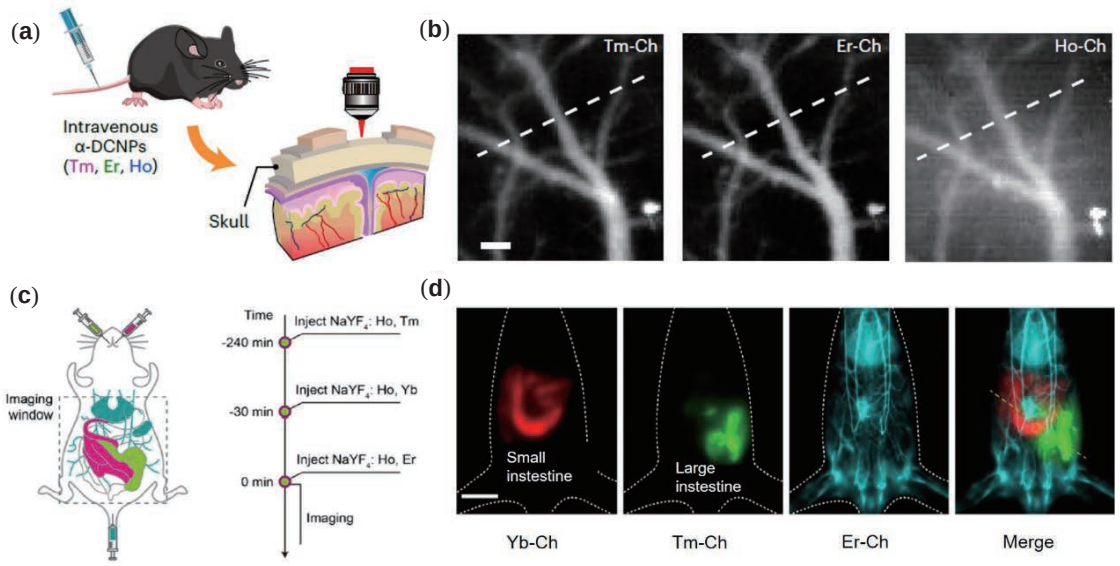

Figure 11 **a.** Schematic of the NIR-II imaging of blood vessels in the mouse brain through the intact skull. **b.** *In vivo* NIR-II images of mouse cerebral vessels obtained in three imaging channels after an intravenous injection of a mixture of α-TmNPs, α-ErNPs, and α-HoNPs. Scale bar, 100 μm [156]. **c.** Schematic illustration showing the three-channel imaging protocol *in vivo*. **d.** *In vivo* three-channel imaging results under 1,143 nm excitation. Scale bar: 10 mm [193]. Reproduced with permission from Refs. [156,193]. Copyright©2023 Springer Nature and Copyright©2025 American Chemical Society.

the population ratio of these two states exhibits an exponential dependence on temperature, leading to a predictable variation in the fluorescence intensity ratio (FIR) of their emissions [200]. In parallel, elevated temperatures enhance multiphonon relaxation, cross-relaxation, and back energy transfer processes through increased lattice vibrations, accelerating non-radiative decay and altering both emission intensity and excited-state lifetime. These combined effects form the fundamental physical basis for both ratiometric- and lifetime-based luminescence thermometry [197,201].

The first use of lanthanide-doped luminescent materials as versatile optical nanothermometers was reported in 2010, where the $NaYF_4$:Er^{3+},Yb^{3+} UCNPs were used to demonstrate that the ratio of fluorescence intensities at 525 nm ($^2H_{11/2} \rightarrow {}^4I_{15/2}$) and 545 nm ($^4S_{3/2} \rightarrow {}^4I_{15/2}$) of Er^{3+} ions exhibited a linear dependence on temperature [202]. This temperature-dependent fluorescence ratio enabled precise thermal sensing within living HeLa cells, covering a measurement range from 25 °C to 45 °C. The same thermally sensitive ratiometric band was further employed in a carbon-coated core-shell upconversion nanocomposite ($NaLuF_4$: Yb^{3+},Er^{3+}@$NaLuF_4$@Carbon), which was designed as a temperature-feedback photothermal agent (PTA) for real-time monitoring of microscopic temperature variations during the photothermal process (Figure 12a) [203]. This study revealed a pronounced discrepancy between the apparent and intrinsic temperatures of the PTA, with its microscopic temperature significantly exceeding the macroscopic level, providing critical guidance for achieving high-spatial-resolution photothermal ablation of tumors under low apparent temperature conditions, minimizing damage to surrounding healthy tissues. In addition to Er^{3+}, other Ln^{3+} ions such as Tm^{3+} (475 nm, $^1G_4 \rightarrow {}^3H_6$) and Ho^{3+} (645 nm, $^5F_5 \rightarrow {}^5I_8$) have also exhibited temperature-sensitive emissions [204]. However, these emissions are largely confined to the visible spectrum, which limits their effectiveness for deep tissue sensing due to photon scattering and absorption.

Luminescence nanothermometry in the NIR windows is favored for *in vivo* temperature detection due to minimized photon absorption and scattering, allowing for deeper tissue penetration and enhanced thermal sensing resolution [205-207]. In recent years, the thermally sensitive NIR fluorescence emissions of lanthanide ions, such as Tm^{3+} at 800 nm [208], Ho^{3+} at 1,190 nm [209], and Er^{3+} at 1,550 nm [210], have been investigated, making them attractive candidates for *in vivo* temperature mapping. It is worth noting that even in the NIR region, biosensing based on a single fluorescence signal is significantly influenced by various factors, including excitation light, probe concentration, and the complex physiological environment, all of which can compromise sensing accuracy. To address this, a self-calibrating ratiometric approach based on dual fluorescence signals has been developed for *in vivo* thermal sensing [211,212].

One example employed PbS QDs and Tm-doped nanoparticles to construct a same-wavelength dual-emission ratiometric luminescent nanothermometer. By utilizing time-resolved techniques to distinguish emissions with distinct lifetimes at NIR-I (810 nm), this probe achieved a thermal resolution of ~0.5 K and a sensitivity of ~5.6% K^{-1} *in vivo* (Figure 12b) [208]. To further improve tissue penetration depth and thermal sensitivity, our group developed an ultra-sensitive NIR-II ratiometric nanothermometer with self-calibration capabilities by incorporating Ag_2S QDs into Yb^{3+}-doped luminescent materials (Figure 12c) [213]. This thermometer takes advantage of the strong thermal responsiveness of fluorescence emission at 1,200 nm and the relative thermal stability of 980 nm emission, yielding precise ratiometric temperature measurements, with thermal sensitivity exceeding 6.5%/°C across the entire physiological temperature

range, and reaching a maximum value of 7.8%/°C at 43.5 °C. While fluorescence intensity-based nanothermometry offers real-time *in vivo* temperature monitoring, it remains susceptible to biological interference and concentration effects, and the accuracy of temperature detection requires further improvement.

Fluorescence lifetime is an intrinsic property that is unaffected by excitation conditions, probe concentration, penetration depth, or physiological environment [214]. Thus, lifetime-based nanothermometry is a powerful technique with the key potential to overcome the limitations associated with PL intensity ratio nanothermometry [196]. Currently, our group has investigated the thermal sensitivity of fluorescence lifetime by regulating the back energy transfer process from Yb^{3+} to Nd^{3+} ions and the energy migration process between Yb^{3+} ions in lanthanide-doped luminescent materials ($NaYF_4$@$NaYF_4$:Yb^{3+},Nd^{3+}@CaF_2) with a ternary structure (Figure 12d) [215]. The developed lifetime-based thermosensitive nanoprobes provide accurate temperature feedback even in harsh environments with pH ranging from 1 to 12 and across varying tissue thicknesses. Moreover, the potential of designed lifetime-based nanothermometry for *in vivo* diagnosis of murine inflammation and precise mapping of temperature distribution in nanoprobe-targeted areas has been demonstrated.

4.1.3 Super-resolution imaging

The breakthrough in super-resolution microscopy has enabled the nanoscale analysis of cell structures and subcellular organelles, significantly expanding the applications of optical microscopy in life sciences [216]. In this context, high-performance lanthanide-doped luminescent materials have emerged as a promising choice for real-time super-resolution imaging of nanoscale subcellular structures, bringing new momentum to the advancement of cell biology [217,218]. Initially, the visible-range upconversion fluorescence of Er^{3+}-doped luminescent materials was applied to real-time imaging at the single-vesicle level in living cells, enabling continuous tracking of intracellular UCNPs movements for up to 6 hours at the rate of 20 frames s^{-1} without interruption [219]. The same fluorescent emission was also utilized to construct 3D images of UCNPs in living cells through wide-field image sectioning [220]. However, the imaging resolution in these studies remains limited.

Stimulated emission depletion (STED) microscopy is a typical and powerful super-resolution technique that surpasses the diffraction limit by depleting luminescence emission [217,221-223]. The potential of UCNPs for low-power super-resolution STED microscopy was first demonstrated in $NaYF_4$:Yb^{3+},Tm^{3+} UCNPs

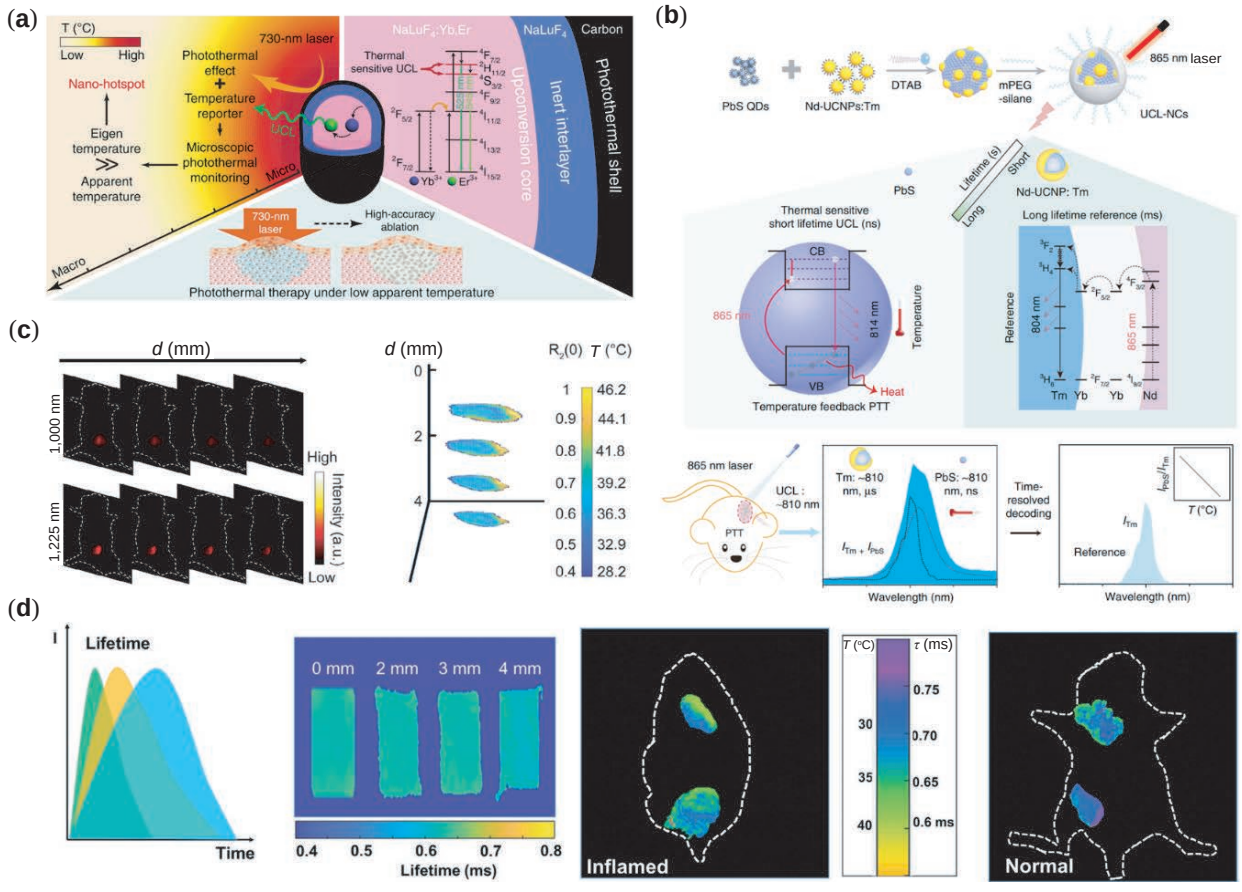

Figure 12 **a.** The schematic of csUCNP@Carbon illustrates its role in enabling precise PTT by using upconversion emission to monitor microscopic temperature under 730-nm irradiation [203]. **b.** Schematic diagram of precise *in vivo* wavelength-proportional temperature monitoring using time-resolved techniques [208]. **c.** NIR fluorescence imaging and temperature mapping of the NIR-II ratiometric nanothermometer at 1,000 and 1,225 nm across different mouse body regions [213]. **d.** Lifetime-based thermoluminescence imaging using nanoprobes in inflamed and normal mice, independent of tissue penetration depth [215]. Reproduced with permission from Refs. [213,215]. Copyright©2023 Wiley-VCH and Copyright©2020 Wiley-VCH.

highly doped with 8% Tm^{3+}, achieving single-particle imaging with a resolution of 1/36 of the excitation wavelength [218]. Similarly, by harnessing the strong cross-relaxation in highly doped Tm^{3+} in $NaYF_4$:18%Yb^{3+},10%Tm^{3+} UCNPs, which induces population inversion between the metastable $^3H_4$ energy level and the $^3H_6$ ground state, an impressive 96% optical depletion of UCL at 455 nm was achieved [224]. This facilitated STED super-resolution imaging of immunostained fixed cytoskeletal structures, with a resolution of approximately 82 nm (Figure 13a). While the depletion wavelength in these studies remains within the upconversion emission, achieving long-term, autofluorescence-free super-resolution imaging in the NIR optical window under low-power continuous-wave (CW) laser depletion remains a challenge. For overcoming this limitation, the quasi-four-level Nd-activated DS nanoparticles were fabricated, realizing background-suppressed STED super-resolution imaging in the all-NIR spectral band with near-unity (>98.8%) luminescence depletion at 1,064 nm under a saturation intensity of ~19 kW/cm^2. The all-NIR regime allows high-resolution visualization of intracellular microtubule structures down to 57 nm and achieves a consistent ~70 nm resolution deep within brain tissues without requiring aberration correction (Figure 13b) [221].

Despite the rapid development of STED, a diffraction-free fluorescence imaging technique, it is still fundamentally limited by factors such as high saturation intensity illumination and the limited photon budget of the probes [216]. To address this issue, novel super-resolution imaging techniques have been explored [225]. One is the surface-migration emission depletion (SMED), which utilizes the gadolinium sublattice to directly transfer energy from the luminescent center to the surface quencher, achieving efficient emission loss through surface migration in both spatial and energy domains (Figure 13c) [223]. By employing a dual-beam CW laser scheme (975 nm excitation and 730 nm depletion), this approach achieves over 95% emission depletion efficiency at a low saturation intensity of 18.3 kW/cm^2, offering autofluorescence-free, non-re-excited background super-resolution imaging with a saturation intensity three orders of magnitude lower than traditional fluorophores. Moreover, based on the cascading amplification depletion effect in lanthanide upconversion systems, a universal stimulated-emission induced excitation depletion (STExD) microscopy has been reported (Figure 13d) [222]. In this approach, emission inhibition across a wide range of emitters, including Nd^{3+}, Yb^{3+}, Er^{3+}, Ho^{3+}, Pr^{3+}, Eu^{3+}, Tm^{3+}, Gd^{3+}, and Tb^{3+}, in $NaYF_4$:Nd^{3+} NPs was obtained through cutting off the excitation chain. As a result, this method affords multi-chromatic nanoprobe imaging with a lateral resolution down to 34 nm, as well as subcellular imaging of actin filaments with immunolabeling.

4.1.4 Nanomechanical sensing

Mechanical forces play a key role in various biological processes, including cellular sensing, signal transduction, tissue growth, and disease progression [226,227]. Accurately measuring mechanical signals within living organisms holds the potential to deepen understanding of biological mechanisms and enable effective

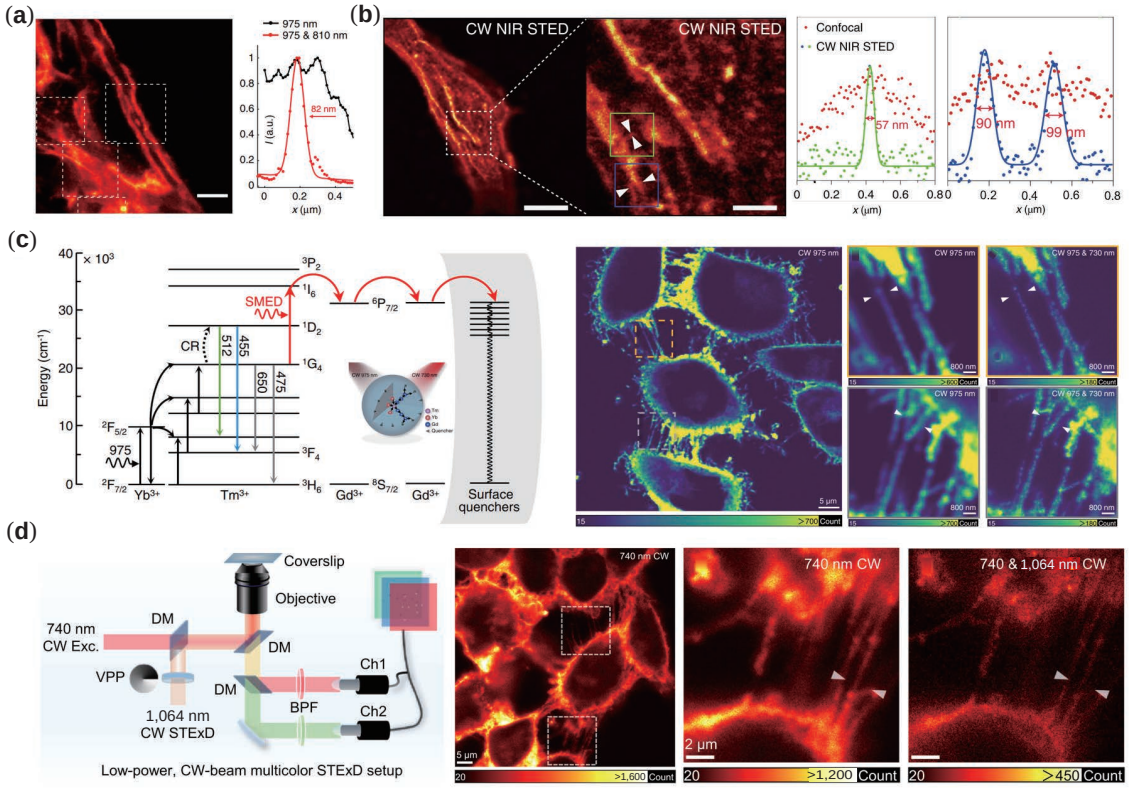

Figure 13 Super-resolution *in vivo* imaging achieved employing lanthanide-doped luminescent materials via STED microscopy **a** UCL [224], **b** DCL [221], **c** SMED microscopy [223], and **d** STExD microscopy [222]. Reproduced with permission from Ref. [221]. Copyright©2023 Springer Nature.

interventions [228,229]. Optical stress nanosensors offer a powerful tool for remotely monitoring force signals in living organisms with high sensitivity and spatial resolution [230,231]. A particularly intriguing approach to mechanical signal detection involves the mechanical luminescence of lanthanide-doped luminescent materials, which primarily arises from piezoelectric effects and crystal field interactions [232]. Through strong electron-lattice coupling, mechanical stress generates a piezoelectric field that modulates charge carrier dynamics. The released carriers are temporarily trapped by transient lattice defects before recombining with luminescent centers, ultimately producing fluorescent emission [185,232]. Over the past decades, the mechanical luminescence properties of rare-earth emitters have been demonstrated in various host lattices, including CaZnOS [233], $Ca_2Nb_2O_7$ [234], $SrZn_xS_yO$ [235], and $(Sr,Ba)Si_2O_2N_2$ [236].

In fluoride hosts, $NaYF_4$ nanocrystals co-doped with Yb^{3+} and Er^{3+} exhibit enhanced force tunability through energy coupling with d-metal Mn^{2+}, enabling precise tracking of stress-induced spectral responses, including variations in fluorescence intensity and shifts in emission peak positions, within the range from 100 nN to 10 μN [237]. Furthermore, in β-$NaGdF_4$ nanocrystals, the upconversion fluorescence emission of Eu^{3+} ions has also been found to be highly sensitive to mechanical force changes [238]. However, these studies are confined to visible emissions and limited force ranges. To address these limitations, highly Tm^{3+}-doped avalanching nanoparticles (ANPs) have been employed as nanomechanical sensors that can be remotely addressed by deeply penetrating NIR light, allowing for the detection of forces from piconewtons to micronewtons with a dynamic range exceeding four orders of magnitude [239]. The mechanical sensitivity of the photon-avalanching process is characterized using atomic force microscopy in conjunction with single-nanoparticle optical spectroscopy, demonstrating its exceptional force responsiveness. Additionally, different optical force-sensing modalities, including mechanobrightening and mechanochromism, were demonstrated by manipulating Tm^{3+} concentrations and energy transfer within the nanosensors. This work further emphasizes the potential of lanthanide-doped fluorides in force-sensing applications.

It is worth noting that recently, lanthanide-doped luminescent materials have seen significant success as nanomechanical sensors in the application of *in vivo* force sensing (Figure 14) [240]. This study incorporates $NaY_{0.8}Yb_{0.18}Er_{0.02}F_4$@$NaYF_4$ nanoparticles into polystyrene microspheres to develop a non-toxic, ingestible, optically readable nanomechanical sensor for the quantitative analysis of luminal forces, with applications in *in vivo* muscle mechanics research. Through *in vitro* studies combining optical microscopy and atomic force microscopy, it was found that the ratio of red to green light emission changes linearly and hysteresis-free in response to applied forces. In living *Caenorhabditis elegans* (*C. elegans*) models, it was observed that adult worms generate bite forces of approximately 10 μN during feeding, with the force generation pattern aligning with muscle activity in the feeding organ. Additionally, the measured bite force corresponds to Hertzian contact stresses within the pressure range required to lyse the bacterial food. This work demonstrated the feasibility of lanthanide-associated nanomechanical sensors for *in vivo* mechanistic quantification.

4.2 Therapy

Precise cancer treatment remains a major challenge and continues to be a central focus in biomedical research. Leveraging the unique photophysical properties of lanthanide-doped luminescent materials to trigger light-activated therapeutic processes or controlled drug release has become a research hotspot in tumor optical therapy. This section highlights recent advances in the application of these nanomaterials in PDT, photothermal therapy (PTT), and light-activated multimodal treatments [241].

4.2.1 Photodynamic therapy

PDT is a minimally invasive cancer treatment that utilizes photochemical reactions for site-specific therapy, relying on the

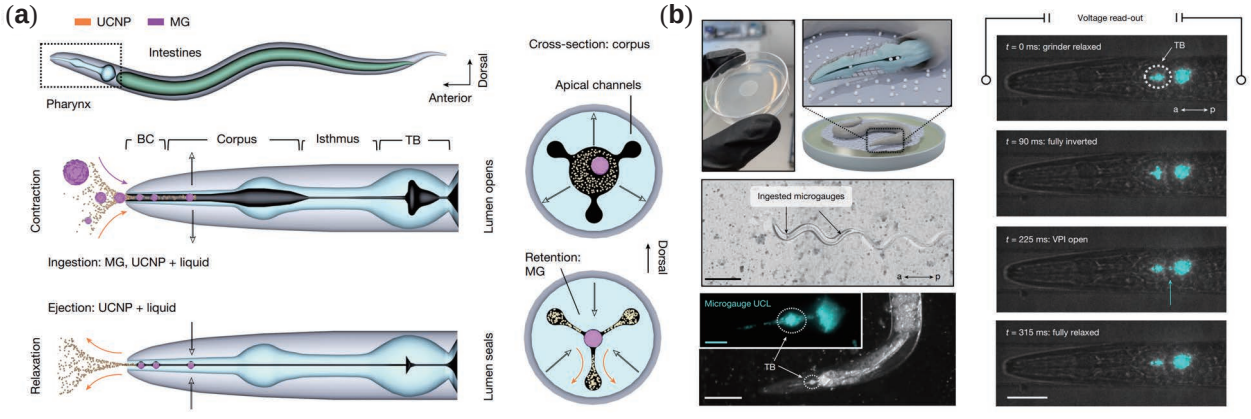

Figure 14 **a.** Schematic of muscle movements in *C. elegans* during pharyngeal contraction (top) and relaxation (bottom). Black arrows indicate muscle movement direction, while orange and purple arrows represent UCNP and microtubule motion, respectively. **b.** Microgauge ingestion and transport in *C. elegans*, showing consumption, localization in the intestine, and serotonin-stimulated movement, with UCL (cyan) highlighting particle transport. Buccal cavity (BC), microgauge (MG), terminal bulb (TB) [240]. Reproduced with permission from Ref. [240]. Copyright©2025 Springer Nature.

synergistic action of photosensitizers (PSs), specific-wavelength light excitation, and oxygen molecules [242-244]. However, most PSs are activated by visible light, limiting their penetration depth *in vivo* [245]. Lanthanide-doped luminescent materials with anti-Stokes shift upconversion fluorescence emission, capable of converting NIR light into UV or visible light, serve as an ideal partner for enhancing the tissue penetration depth of PDT treatment [246]. Moreover, their potential in tumor PDT has been fully validated in various UCNPs, which have been meticulously designed as PS carriers and light transducers [225,247-249]. Recently, research in this field has focused on pursuing higher efficiency, greater precision, and improved safety in PDT treatment [250].

Efficient PDT. In UCNPs-mediated PDT systems, PSs such as Chlorin e6 (Ce6) [251-253], Merocyanine 540 (MC540) [254], zinc phthalocyanine (ZnPc) [255,256], rose bengal (RB) [257], methylene blue (MB) [258], MnO_2 [259] have been extensively studied. Since the loading capacity of PSs and the energy transfer efficiency between UCNPs and PSs are critical factors influencing PDT efficacy, researchers have optimized surface charge modulation to enhance PS loading and shorten the distance between UCNPs and PSs, thereby improving energy conversion efficiency [252,260]. Beyond single-PSs-doped systems, a co-encapsulation strategy involving MC540 and ZnPc has been developed (Figure 15a) [255]. This approach takes advantage of the multicolor emission capability of UCNPs under a single 808 nm excitation source, enabling the simultaneous activation of two distinct PSs to generate a sufficient amount of reactive oxygen species (ROS) for enhanced therapy efficacy. In addition to conventional organic small-molecule PSs, various semiconductors, such as ZnO [261] and titanium dioxide (TiO_2) [262,263], as well as metal nanomaterials including metal QDs [264] and metal-organic frameworks (MOFs) [265,266], with high-efficiency ROS generation capabilities, have also been integrated with UCNPs to establish highly effective PDT platforms. Among these, MOFs have attracted significant attention due to their tunable structures and high porosity, which not only prevent PS aggregation and self-quenching but also promote the diffusion of ROS from the framework to the lesions, thereby enhancing ROS utilization efficiency [267,268]. Thus, UCNPs-MOF heterostructures, developed based on the spectral overlap between the UV emission of UCNPs under NIR excitation and the absorption spectrum of MOFs, have been proven to achieve deep tissue penetration while maintaining efficient ROS generation, resulting in highly effective PDT [266,269-271].

Precise PDT. Targeted delivery of therapeutic agents to tumors *in vivo* is crucial for achieving precise cancer treatment [272,273]. To achieve targeted PDT, various tumor-specific recognition molecules, such as folic acid (FA) [274,275], tumor-associated antibodies [276], and peptides [253], have been conjugated to the surface of UCNPs. These molecules can effectively recognize and bind to specific receptors on the surface of tumor cells, thereby ensuring precise delivery of UCNPs-mediated PDT agents to the tumor cells [185]. To further prevent nonspecific binding of recognition molecules to normal cells, UCNPs-mediated PDT strategies responsive to tumor microenvironments, such as low pH and high H_2O_2, have been extensively developed [259,277]. For instance, a DNA/UCNPs nanocomposite was designed, where DNA shielding blocks premature interactions and reconfigures in the acidic tumor microenvironment to expose FA, enabling targeted binding and FRET-mediated singlet oxygen generation (Figure 15b) [251]. Given that mitochondrial damage is critical for PDT-induced tumor cell death, various mitochondrial-targeting strategies have also been developed for enhancing ROS-mediated tumor therapy [271,278,279]. Additionally, benefiting from the multi-wavelength fluorescence emission of lanthanide-doped luminescent materials, real-time, non-invasive *in vivo* imaging can be achieved while simultaneously activating the PS, facilitating monitoring and guidance of PDT for precise therapy [263,280,281]. For example, Zuo et al. [263] present a novel "off-on" controlled upconversion system ($NaErF_4$@$NaYF_4$@$NaYbF_4$:0.5%Tm@$NaYF_4$) with photoswitchable dual-wavelength emission for imaging-guided PDT (Figure 15c). Under 980 nm excitation, strong UV-blue emission is activated to induce PDT, whereas 800 nm excitation suppresses UV-blue emission, leaving only red emission (660 nm) for real-time imaging. This work provided a unique photoswitching capability that enables precise spatial and temporal control over PDT while simultaneously monitoring the therapeutic process, demonstrating its potential for image-guided and precise PDT.

Safe PDT. In UCNPs-mediated PDT systems, both the physicochemical properties of therapeutic agents and external laser irradiation are crucial factors influencing their biological safety [185]. Currently, a variety of biofriendly ligands, such as phospholipids, polyethylene glycol (PEG), silane coatings, chitosan, and proteins, have been employed for modifying UCNPs [282-284], which not only improve the stability and dispersion of UCNPs in biological environments but also contribute to their overall safety and effectiveness in therapeutic applications. To minimize potential damage caused by laser irradiation, the bio-friendly 808 nm laser is increasingly preferred over the 980 nm laser, which is more likely to induce thermal damage in biological tissues [214]. Additionally, significant efforts have also been made to reduce the excitation power required for effective photosensitization [285-287]. A representative study presents a novel NIR photosensitization method using lanthanide inorganic nanoparticles to directly sensitize the triplet excited states of porphyrin-based and phthalocyanine-based PSs, avoiding ISC (Figure 15d) [286]. This approach reduces the required NIR power for singlet oxygen generation to ~10–80 mW/cm^2, over 100 times lower than traditional methods, offering a safer and more efficient alternative for UCNPs-mediated PDT applications.

4.2.2 Photothermal therapy

PTT is a noninvasive treatment that utilizes PTAs to convert absorbed light into heat, inducing localized hyperthermia (above 42 °C) to ablate tumors or infected tissues [288]. While PTT shows promise, its effectiveness is often hindered by the limited tissue penetration of visible light (400–700 nm), suboptimal photothermal efficiency and biocompatibility of existing PTAs, and potential heat damage to surrounding healthy tissues [289,290]. Benefiting from their unique spectral properties, lanthanide-doped luminescent materials have gained significant attention for improving PTT efficacy while mitigating photothermal damage-related side effects [284,291]. Nowadays, various UCNPs-PTAs composites, combining lanthanide-doped lumi-

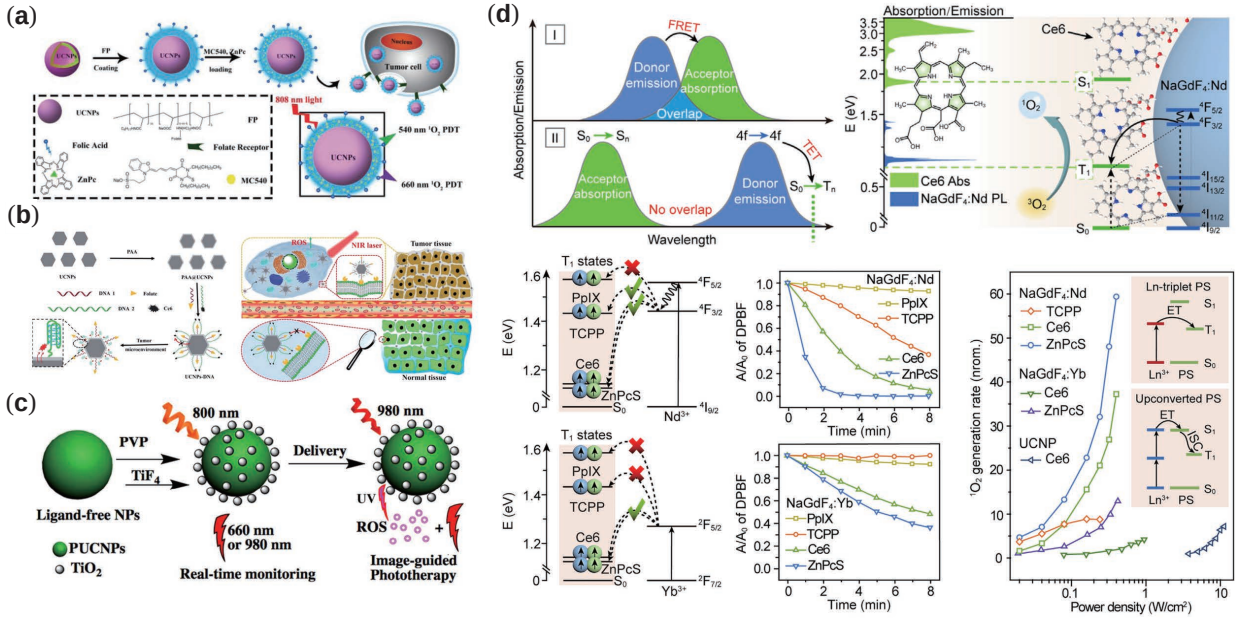

Figure 15 **a.** Schematic illustrating the enhanced PDT efficiency of MC540 and ZnPc dual PSs [255]. **b.** Illustration of precise tumor targeting and specific PDT achieved via DNA-modified UCNPs@PAA–DNA [251]. **c.** Diagram of photoswitchable PDT using PUCNPs@TiO_2 for real-time monitoring and image-guided therapy [263]. **d.** Schematic of direct lanthanide-TET between the 4f excited state of a lanthanide ion and the triplet state of an organic phosphor (up) and efficient irradiation-dependent singlet-oxygen generation under 980 nm irradiation at 3.73 W/cm^2 (down) [286]. Reproduced with permission from Refs. [255,263]. Copyright©2019 Royal Society of Chemistry and Copyright©2018 American Chemical Society.

nescent materials with organic or inorganic PTAs, such as Au nanoparticles, Ag nanoparticles, Fe_3O_4 nanoparticles, graphene oxide (GO), Cu_xS, and organic light absorbers, have been extensively developed and have demonstrated their feasibility for *in vivo* tumor PTT [241,292-295]. For instance, Au nanoparticles, which exhibit strong thermal effects due to surface plasmon resonance, were coupled with UCNPs, achieving efficient PTT [296]. Liu et al. [297] developed polydopamine (PDA)-coupled $NaYF_4$:Yb^{3+},Er^{3+}@$NaYF_4$:Yb^{3+} nanoparticles for NIR light-mediated PTT. Lv et al. [298] selected CuS as the PTA and developed a strategy for its *in situ* growth on the surface of $NaYF_4$:Yb^{3+},Er^{3+}@$NaYF_4$:Nd^{3+},Yb^{3+} nanoparticles, enabling green fluorescence emission from Er^{3+} under 800 nm excitation to guide PTT.

The NIR fluorescence emission of lanthanide-doped luminescent materials facilitates the realization of high-resolution, low-background real-time *in vivo* imaging-guided PTT, enhancing therapeutic precision [241,299]. A PTT nanoplatform (UCNPs@CS@Ag_2Se) was developed by *in situ* growth of ultrasmall Ag_2Se nanodots on chitosan-coated UCNPs (Figure 16a) [300]. Leveraging the strong NIR absorption of Ag_2Se for photothermal conversion and the 980 nm fluorescence emission of Yb^{3+} under 808 nm excitation, this system permits NIR-I imaging-guided PTT with a photothermal conversion efficiency of 37.6%. However, due to the limited tissue penetration depth and imaging resolution of NIR-I luminescence, researchers have shifted their focus to NIR-II fluorescence, which offers lower tissue absorption and scattering for more precise imaging navigation [301]. Li et al. [302] prepared a hydrophilic $NaLuF_4$ NRs@PDA therapeutic probe via the microemulsion method. This probe achieved simultaneous NIR-II fluorescence emission (>1,500 nm) and a high photothermal conversion efficiency of 40.18% under 980 nm excitation, finally demonstrating excellent NIR-II imaging-guided PTT for cancer treatment. However, utilizing the same excitation light source for both imaging and treatment could result in nonspecific activation of the photothermal effect during drug delivery, potentially leading to thermal damage to normal tissues. To solve this issue, our group presents a novel lanthanide-based PTT agent consisting of prussian blue (PB)-coated $NaErF_4$@$NaYF_4$@$NaNdF_4$ CSS nanocrystals encapsulated in a phospholipid PEG micelle [303]. This agent displays distinct imaging and hyperthermia capabilities under different NIR light activations. The Er^{3+}-rich core ($NaErF_4$) emits NIR-II luminescence (1,525 nm) for high-resolution imaging, while the Nd^{3+}-doped $NaNdF_4$ shell converts NIR light (~808 nm) into heat for PTT. With a light-to-heat conversion efficiency of 50.5%, the agent significantly reduced U14 tumor size in BALB/c mice by approximately 12-fold after a single PTT treatment. This work demonstrates the potential of lanthanide-doped luminescent materials as effective PTT agents.

In PTT, maintaining an optimal temperature at the treatment site is critical for effective cancer cell destruction while minimizing damage to surrounding healthy tissues [288]. Typically, the temperature is kept between 42 °C and 45 °C to target tumors, but overheating can lead to unintended injury to normal tissues, causing side effects and lowering therapeutic accuracy. The precise monitoring and control of temperature during PTT is necessary to avoid excessive heating and ensure targeted treatment [304,305]. Given the difficulty of using traditional contact-based temperature measurements in confined tumor areas, real-time, non-invasive temperature feedback is essential for maximizing PTT efficiency and minimizing harm to normal cells [306].

Recently, lanthanide-mediated PTT agents with remote real-time temperature feedback have been developed to precisely regulate treatment temperature at the lesion site [307]. One representative work fabricated a temperature-feedback $NaLuF_4$:Yb^{3+},Er^{3+}@Na-@$NaLuF_4$@Carbon composite for real-time microscopic temperature monitoring in PTT via the ratiometric fluorescence signal of Er^{3+} at 525 and 545 nm (I_{525}/I_{545}) [203]. This approach enabled highly efficient tumor ablation while minimizing harm to normal tissues. Similar temperature-feedback mechanisms have also been applied to perform tumor PTT using Cit-CuS-composited PTT agents [308] and intratumoral GSH-activatable PTT agents [309]. Furthermore, due to the unique advantages of NIR II *in vivo* optical imaging and efficient sensing, Liu et al. [310] developed LNPs-Au agents with excellent photothermal activity and temperature-sensing performance (Figure 16b). The incorporation of Au NPs with superior photothermal properties further allows for *in situ*, non-invasive, high-resolution, and high-precision temperature monitoring, offering a powerful tool for optimizing PTT.

4.2.3 Optogenetic therapy

UCNPs have opened a new avenue for deep-tissue optogenetic control by overcoming the fundamental limitation of poor tissue penetration by visible light. These nanotransducers absorb tissue-penetrant NIR photons (commonly at ~980 or ~800 nm) and emit wavelength-specific visible light (for example, blue or green) that can directly drive light-sensitive actuators such as channelrhodopsins (ChR) (Figure 17a). This approach enables minimally invasive, wireless optical manipulation of cells in deep tissues and intact animals, converting NIR illumination into localized, biologically relevant excitation with high spatiotemporal precision. Foundational demonstrations showed that lanthanide-based luminous nanomaterials could activate ChR *in vivo* upon NIR irradiation, establishing UCNPs-mediated optogenetics as a viable strategy for remote neural control [311].

Subsequent work refined both the biological application and the materials platform for therapeutic and neuroscientific use. In pioneering *in vivo* studies, Chen and colleagues used UCNPs for transcranial NIR stimulation of the brain, achieving dopamine release (Figure 17b and c), modulation of brain oscillations, suppression of chemically induced seizures through inhibition of hippocampal excitatory neurons, and recall of memories from genetically defined ensembles—demonstrating that UCNPs-mediated optogenetics can produce physiologically and behaviourally meaningful effects in deep brain structures [312]. To address the intrinsically low upconversion efficiency of conventional UCNPs, materials engineering has focused on structural and photophysical enhancements [313]. Dye-sensitized core-active-shell architectures reported by Wu et al. [314] markedly increased luminescence output and shifted the excitation window toward a more biocompatible, deeper-penetrating 800 nm regime, thereby improving the practicality and safety of transcranial stimulation.

Beyond basic neuroscience, UCNPs-based optogenetics is being translated towards regenerative medicine and oncology. For peripheral nerve repair, Yan et al. [315] conjugated acetylcholine-modified UCNPs to bias membrane depolarization in motor neurons, promoting axonal regeneration and neuromuscular junction remodelling. In cancer models, hybrid UCNPs-MOFs constructs have been devised to convert NIR light into visible activation of photo-responsive ion channels (Figure 17d), coupling optogenetic control with ion-based therapies to permit non-invasive manipulation of tumor cell physiology (Figure 17e and f) [316]. Together, these advances illustrate how rare-earth materials can extend optogenetics from a laboratory technique toward therapeutic modalities capable of deep-tissue, wireless control—provided that ongoing challenges in efficiency, targeting, long-term biocompatibility, and clinical translation are addressed.

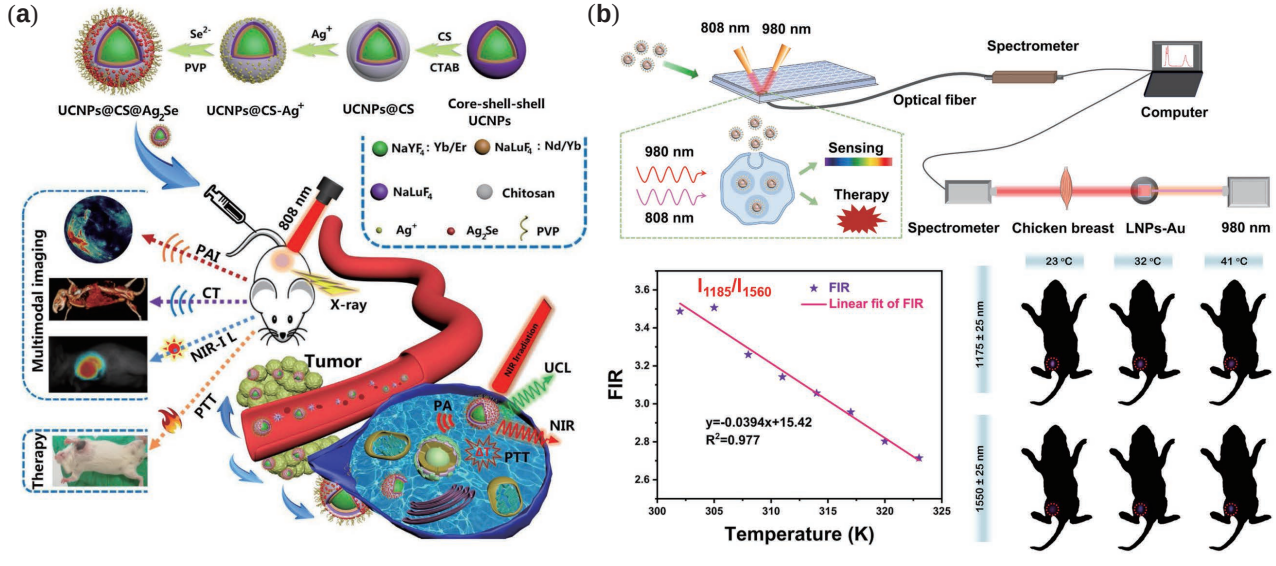

Figure 16 **a.** Schematic diagram of the preparation of UCNPs@CS@Ag_2Se nanocomposites for multimodal imaging-guided cancer PTT [300]. **b.** Schematic diagram of photothermal temperature resolution and high-precision feedback using NIR-II ratiometric fluorescence (up), with the ratiometric fluorescence-temperature curve (lower left) and *in vivo* temperature feedback (lower right) [310]. Reproduced with permission from Refs. [300,310]. Copyright©2019 Elsevier and Copyright©2022 Elsevier.

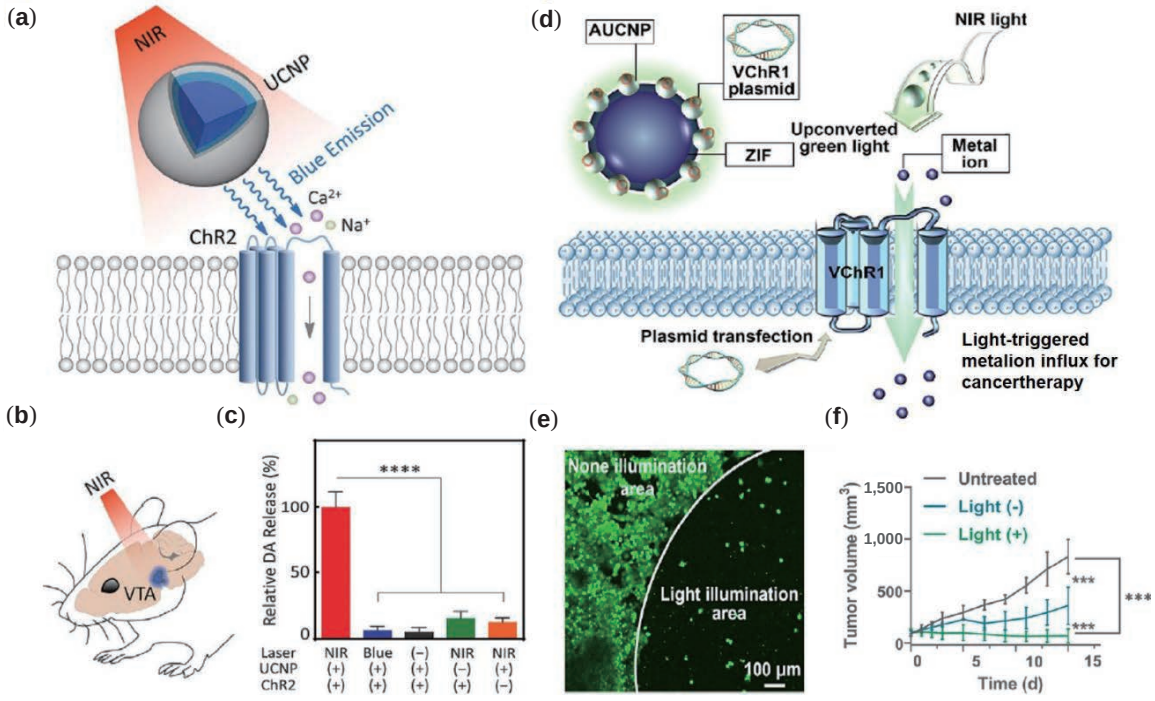

Figure 17 **a.** Schematic principle of UCNPs-mediated NIR upconversion optogenetics. **b.** *In vivo* experimental scheme for transcranial NIR stimulation of the VTA in anesthetized mice. **c.** Cumulative DA release within 15 s after the start of transcranial stimulation under the five conditions [312]. **d.** Scheme illustrating the mechanism for cancer optogenetic therapy based on ZIF@AUCNP@VChR1 nanocomposites. **e.** Confocal PL images of calcein-AM-stained 4T1 cancer cells pretreated with Zn-ZIF@AUCNP@VChR1 in different areas. **f.** Tumor growth curves of the 4T1 tumors post various treatments [316]. Reproduced with permission from Ref. [316]. Copyright©2024 American Chemical Society.

4.2.4 Multimodal treatment

Numerous preclinical and clinical studies have demonstrated that monotherapies often fall short of expectations due to the inherent aggressiveness of cancer, the development of drug resistance, and patient-specific variations [297]. As a result, combining multiple treatment modalities has become an essential direction in cancer therapy to effectively manage tumor progression while minimizing the risk of metastasis and recurrence [317]. In addition to PTT and PDT introduced above, lanthanide-based nanocomposites also hold great potential for radiotherapy (RT), gene therapy, and immunotherapy [318-320]. Their unique properties enable precise therapeutic delivery and synergistic effects, laying the foundation for the development of multifunctional tumor treatment platforms designed to achieve potent tumor eradication and long-term prevention of recurrence.

1) Immunotherapy

Cancer immunotherapy has revolutionized tumor treatment, offering hope for halting progression, eliminating tumors, and improving survival [321]. However, long-term success is limited by challenges like insufficient immune cells and immunosuppression [322]. Lanthanide-mediated phototherapy combined with immunotherapy can fully utilize the tumor-killing effects of phototherapy and the ability of immunotherapy to inhibit tumor recurrence and metastasis, offering promising potential for more effective and comprehensive cancer treatment [241]. In fact, the ability of phototherapy to reverse "cold" tumors into "hot" tumors has been indicated by extensive studies [243,294,323,324]. In addition to the immune activation induced by phototherapy itself, the collaboration with other immune-regulating approaches provides a powerful strategy for designing Lanthanide-mediated multimodal treatments, enhancing therapeutic efficacy through synergistic effects [325]. For instance, Zhou et al. [326] developed UCNPs@ysSiO$_2$ loaded with bacterial lipopolysaccharide (LPS) and ICG, where ICG-mediated photothermal effects and photo-controlled LPS release synergistically activated microglia. This approach presents a promising PTT/immunotherapy strategy for brain-related malignancies. In addition, a PDT-immunotherapy synergy was achieved by camouflaging lanthanide-based PDT agents with macrophage membranes. This design depletes colony-stimulating factor 1 (CSF1) to disrupt macrophage-cancer interactions and, when combined with PSs, induces synergistic PDT and macrophage polarization-driven immune responses (Figure 18a) [327]. Similarly, a macrophage membrane-decorated UCNPs nanocarrier (UCNPs@mSiO$_2$-PFC/Ce6@RAW-Man/PTX) was developed for targeted PDT/immunotherapy multimodal treatment on 4T1-xenografted mice, demonstrating potential for enhanced PDT and macrophage-mediated immunotherapy [328].

2) Radiotherapy

RT, a widely used clinical treatment, employs high-energy radiation to damage cancer cell DNA, impairing their ability to replicate and inducing cell death [329,330]. Lanthanide-doped nanomaterials, owing to their high atomic numbers, are highly valued for their strong X-ray attenuation capabilities, making them promising candidates to enhance RT by increasing localized radiation doses to tumors [320,331,332]. However, single-modality RT faces challenges such as insufficient treatment efficacy, severe side effects from high radiation doses, and tumor

recurrence [333]. In recent years, X-ray-induced bright and persistent fluorescence emission in the UV-visible and NIR regions of lanthanide materials has been discovered [334-336]. These tunable multi-band emissions have been widely exploited to activate PSs, PTAs, and various therapeutic precursors, enabling enhanced X-ray-induced PDT, PTT, and other modal therapies [337,338]. For example, Zhang et al. [257] developed a straightforward yet highly effective nanocomposite by integrating β-$NaGdF_4$:Tb^{3+} NPs with the PS-RB. Under X-ray excitation, the nanoparticle emission perfectly matched RB's absorption, achieving an exceptional FRET efficiency of 99.739%. This optimized energy transfer maximized singlet oxygen production, significantly enhancing therapy. Notably, the combined RT/PDT therapy inhibited 90% of HepG2 tumor growth *in vivo* with an X-ray dose as low as 1.5 Gy (1 Gy = 1 J/kg). The RT/PTT synergistic therapy was achieved by integrating CuS with UCNPs, which not only induced highly localized radiation dose enhancement but also exhibited efficient thermal ablation, leading to complete tumor eradication within 120 days without noticeable recurrence [293]. Beyond the collaboration of PSs and PTAs, gas precursors have also been employed to develop novel multimodal treatments. The integration of an immunogenic cell death (ICD) inducer—CO gas therapy—with RT has been realized using the X-ray-activated fluorescence emission of lanthanide-doped luminescent materials as a mediator [339]. This strategy synergistically combined the direct tumor-killing effect of RT with the X-ray-triggered, *in situ* controllable release of CO gas, establishing a soft X-ray-activated RT/gas therapy/immunotherapy paradigm. Additionally, X-ray-responsive, depth-independent NO gas on-demand release strategies have also been developed to perform the synergistic RT/gas therapy/immunotherapy multimodal treatment [337,340-342]. However, gas therapy, particularly NO, is only effective at therapeutic concentrations in the micromolar range. To address this limitation, X-ray-activated on-demand release strategies for peroxynitrite ($ONOO^-$), a more cytotoxic reactive nitrogen species, have been reported, achieving $ONOO^-$-induced radiosensitization and synergistic immunomodulation [343-345]. A recent study developed an X-ray-activated nanosystem by integrating an NO donor, a TGF-β inhibitor, and UCNPs (Figure 18b) [346]. This "one-two punch" strategy synergistically integrates $ONOO^-$-mediated radiosensitization via X-ray-triggered on-demand release with tumor-associated neutrophil (TANs) polarization-induced tumor microenvironment remodeling. By revealing the role of TANs reprogramming in enhancing RT efficacy, this approach ultimately realizes effective radioimmunotherapy for metastatic colorectal cancer.

3) Gene therapy

Gene therapy is a cutting-edge approach that modifies genetic material to treat or prevent diseases, offering potential for correcting faulty genes and treating cancers and genetic disorders [347,348]. Lanthanide-doped luminescent materials, acting as photo-responsive nanocarriers for diverse genetic cargos, including small interfering RNA (siRNA) and clustered regularly interspaced short palindromic repeats (CRISPR)/Cas9 systems, allow for NIR light-controlled precise release of therapeutic genes at specific targets [349-351]. This strategy holds promise for enhancing spatiotemporal control, improving therapeutic efficacy, and minimizing off-target effects in gene therapy. Recently, He et al. [352] presented a synergistic treatment combining siRNA and PDT using upconversion nano-onions (UCNOs), which feature a UCNPs core and multiple functional layers: an inner layer of RB conjugated with polyethylenimine 600, a middle layer of diselenide-linked PEI 600 containing siRNA and R8 peptide, and an outer hyaluronic acid (HA) layer for targeted delivery (Figure 18c). Upon 808 nm irradiation, 540 nm luminescence emitted by UCNPs was allowed to activate RB to generate ROS, subsequently triggering UCNOs disassembly and siRNA release. This resulted in efficient gene silencing *in vitro* and tumor growth suppression *in vivo*. Additionally, the photo-controlled CRISPR-Cas9 gene editing and synergistic PDT have been successfully achieved in a NIR light-activated nanophotonic system, where the UCNPs served as carriers for plasmid delivery and nanotransducers (Figure 18d) [353]. The gene editing and PDT processes were triggered by visible light at 460 and 650 nm, respectively, converted from 980 nm NIR excitation. The synergistic anti-tumor effects were obtained through combining precise gene editing with minimal off-target effects and enhanced PDT, providing potential for gene-related multimodal therapy.

4) Photoechogenic sonotheranostics

Upconversion-driven ultrasonic imaging and sonotherapy are promising directions. Mowat et al. [331] reported the design and action of upconversion-enabled photoinflatable nanoparticles for *in situ* NIR-triggered ultrasound imaging to guide ultrasound-mediated drug delivery. The nanoparticle design included UCNPs core and an organic shell carrying gas generator molecules and drugs. The upconverting core transformed low-energy NIR photons into UV photons, which, by photolysis of the gas generator, produced carbon dioxide to inflate the tumor-accumulated nanoparticles into microbubbles for sonotheranostics. This hybrid nanoparticle also enabled upconversion optical imaging using different NIR laser power. The use of low-frequency (10 MHz) ultrasound produced the collapse of microbubbles to release drugs deep inside the tumor through cavitation-induced transport.

5. Commercial and potential medical applications

In vitro diagnostics (IVD) have become pivotal in modern healthcare due to their ability to provide rapid, accurate, and cost-effective diagnostic results [354,355]. Unlike traditional laboratory-based testing, IVD platforms deliver timely clinical information with minimal technical expertise, making them highly suitable for point-of-care testing (POCT). These platforms are especially advantageous for on-site disease screening and monitoring owing to their portability, low operational costs, and ease of use. The growing demand for decentralized diagnostics in resource-limited and emergency settings has driven the rapid expansion of IVD technologies in clinical medicine, infectious disease surveillance, and personalized healthcare.

Lanthanide-doped luminescent materials have emerged as powerful tools in IVD applications due to their large Stokes or anti-Stokes luminescence, narrow emission bandwidths, long luminescence lifetimes, and excellent photostability [356,357]. These features contribute to their remarkable optical performance, particularly under complex biological conditions. First, many lanthanide-based materials can be excited in the NIR

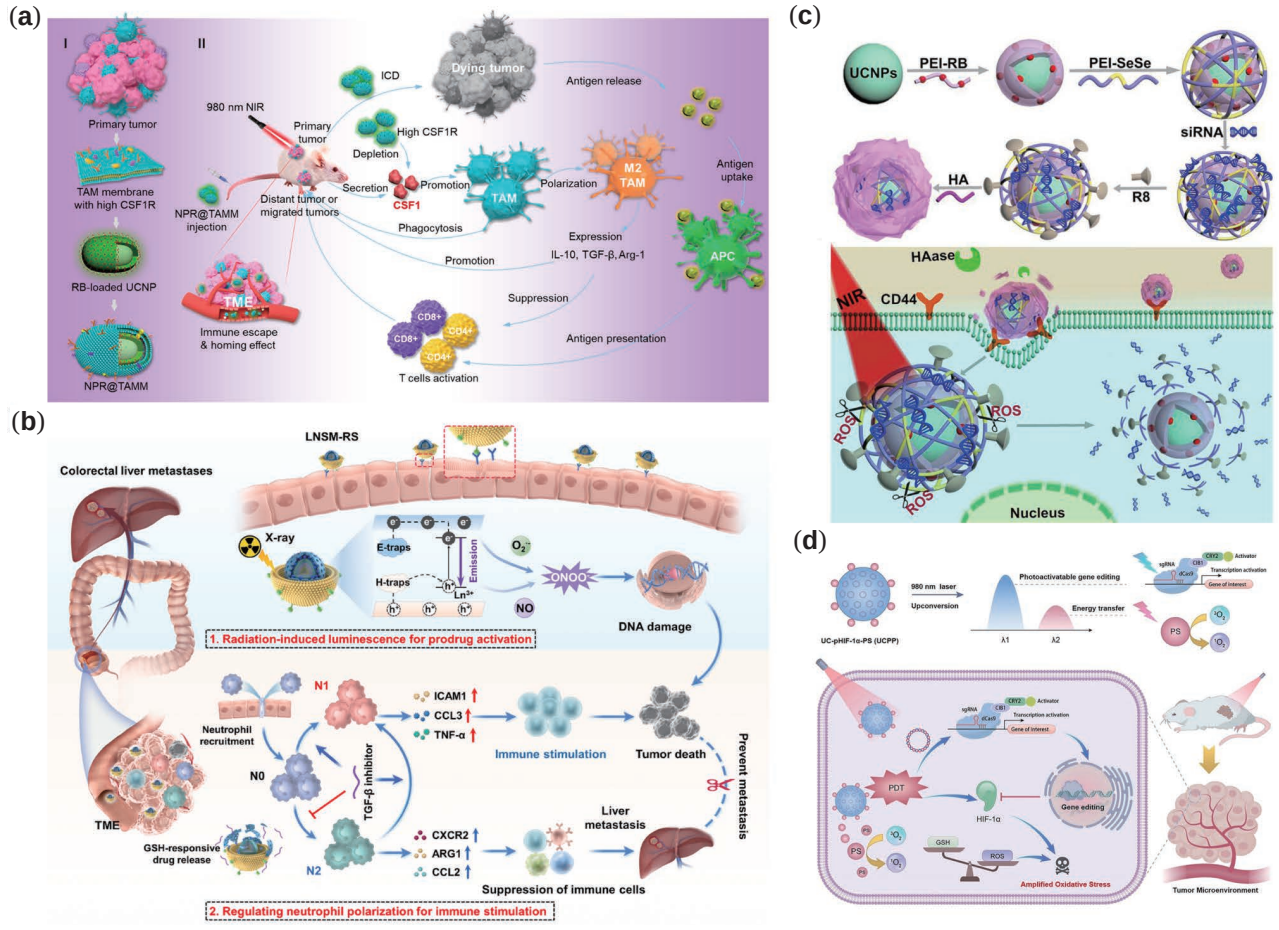

Figure 18 Schematic diagrams illustrating various multimodal treatments. **a.** Lanthanide-based PDT agents camouflaged with tumor-associated macrophage membranes to enhance the synergy of photodynamic immunotherapy [327]. **b.** An X-ray-activated nanosystem enhancing radioimmunotherapy through $ONOO^-$-mediated radiosensitization and TAN polarization-induced tumor remodeling for improved colorectal cancer treatment [346]. Synergistic PDT and gene therapy strategy through the sequentially responsive release of **c** PS RB and siRNA [352] as well as **d** upconversion emission triggered CRISPR-Cas9 gene editing and PSs release [353]. Reproduced with permission from Refs. [327,346,352,353]. Copyright©2021 American Chemical Society, Copyright©2025 Elsevier, Copyright©2019 Elsevier, and Copyright©2025 American Chemical Society.

region, which minimizes background interference from biological autofluorescence typically induced by UV or visible light excitation. This NIR excitation significantly improves the signal-to-noise ratio and reduces photodamage to biological samples. Second, UCL, a nonlinear process where low-energy NIR photons are converted into higher-energy visible emissions, further reduces signal interference. Since proteins, nucleic acids, and lipids generally exhibit strong fluorescence under UV or visible excitation, UCL allows for background-free detection by avoiding the excitation of these endogenous chromophores. Third, time-resolved fluorescence (TRF) techniques take advantage of the long emission lifetimes of lanthanide ions, which typically range from microseconds to milliseconds. In contrast, background fluorescence from biological components decays within nanoseconds. By introducing a short delay between excitation and detection, TRF effectively suppresses short-lived background signals, leading to significantly enhanced assay sensitivity. Together, these properties make lanthanide-doped luminescent materials ideal candidates for high-performance fluorescence-based IVD platforms, especially in assays requiring high sensitivity, low detection limits, and multiplexing capabilities [358,359].

Several commercial IVD platforms have successfully applied lanthanide-doped luminescent materials, particularly in the form of UCL and TRF. These technologies have enabled high-sensitivity, low-background assays, especially suitable for detecting low-abundance biomarkers in complex biological matrices. The use of lanthanide-based reporters in lateral flow assays (LFAs) and immunoassay analyzers has facilitated the development of quantitative POCT as well as automated clinical diagnostics. For example, companies such as Hotgen Biotech (China), Cisbio Bioassays (France), and Uniogen (Finland) have developed and commercialized lanthanide-based IVD products using either upconversion nanoparticles or TRF chelates. Their platforms have been applied to detect infectious diseases, tumor markers, and inflammatory indicators, and are deployed in hospitals, outpatient clinics, and decentralized settings. These examples highlight the global translational potential of lanthanide luminescent technologies and mark an important step toward broader clinical adoption beyond laboratory-scale applications.

To further expand the applicability of lanthanide-doped luminescent materials in IVD, considerable efforts have been devoted to developing flexible, miniaturized, and low-cost detection platforms. In particular, lanthanide-enhanced microfluidic platforms and LFAs have emerged as promising formats that combine the optical advantages of rare-earth materials with user-friendly operation and point-of-care (POC) readiness. These platforms are highly compatible with simple fabrication techniques and portable detectors, making them well-suited for use in decentralized and resource-limited settings.

5.1 Microfluidic platforms

5.1.1 Paper-based microfluidics

Paper-based microfluidic analytical devices (μPADs) have emerged as attractive platforms for IVD due to their simplicity, low cost, and compatibility with POCT [360-362]. These devices rely on capillary action to autonomously transport fluids, eliminating the need for external pumps or complex instrumentation. Paper substrates also offer advantageous properties, including biodegradability, biocompatibility, tunable pore sizes, and adjustable capillary flow rates, which collectively enable diverse fluidic control strategies and versatile biosensor configurations. These features make μPADs especially suitable for decentralized testing scenarios such as home-based health monitoring and diagnostics in resource-limited environments.

The integration of lanthanide-doped luminescent materials into μPADs has further enhanced their diagnostic utility. These materials exhibit anti-Stokes emission under NIR excitation, effectively minimizing background fluorescence and increasing signal-to-noise ratios in complex biological samples. Their long luminescence lifetimes support TRF detection, allowing temporal discrimination from short-lived background signals. Additionally, their narrow emission bandwidths permit spectral multiplexing, making them ideal for multi-analyte detection. The coupling of these properties with smartphone-based readout systems enables quantitative, real-time analysis, promoting the practical implementation of μPADs in POCT [363,364].

The historical development of paper-based microfluidic platforms began with a pivotal study by Martinez et al. [365] in 2007, who introduced a photolithography-based method for patterning hydrophilic channels separated by hydrophobic barriers on chromatography paper. In their fabrication process, the paper substrate was uniformly coated with SU-8 photoresist, exposed to UV light through a photomask to selectively crosslink the resist, and subsequently developed to form fluidic pathways. Capillary-driven fluid flow along the defined channels enabled multiplexed assays using minimal sample volumes, and assay results could be directly visualized by colorimetric changes without external instrumentation (Figure 19a and b). This early demonstration established paper as a viable substrate for low-cost, disposable, and portable diagnostic devices.

While colorimetric μPADs offer simplicity and visual interpretability, their sensitivity is generally limited by background interference from paper substrates and low signal output. To address this limitation, He et al. [366] proposed a proof-of-concept device termed UC-μPAD by incorporating UCNPs into a simple paper platform (Figure 20a). Hydrophobic barriers were drawn on standard office printing paper using a permanent marker to define circular test zones, each requiring only ~4 μL of sample. UCL at 547 nm was recorded under 980 nm NIR excitation, which significantly suppressed autofluorescence and scattering from the paper. This system demonstrated highly sensitive detection of matrix metalloproteinase-2 at a limit of 8.3 pg/mL (1 pg/mL = 1×10^{-12} g/mL), highlighting the feasibility of coupling UCNPs with paper-based devices for enhanced fluorescence diagnostics.

Building on this foundational work, further developments expanded the functionality of UCNP-integrated μPADs toward more sensitive and specific bioassays. Wu et al. [367] developed a

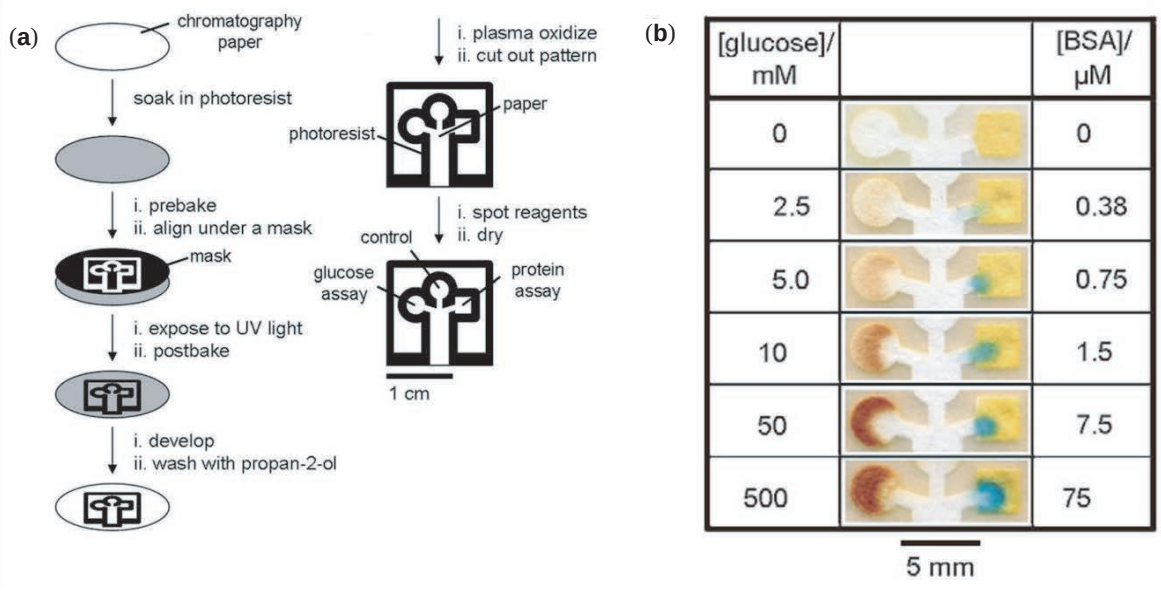

Figure 19 **a.** Diagram depicting the method for patterning paper into millimeter-sized channels. **b.** Glucose and protein detection assays by using varying concentrations of glucose and BSA [365]. Reproduced with permission from Ref. [365]. Copyright©2007 Wiley-VCH.

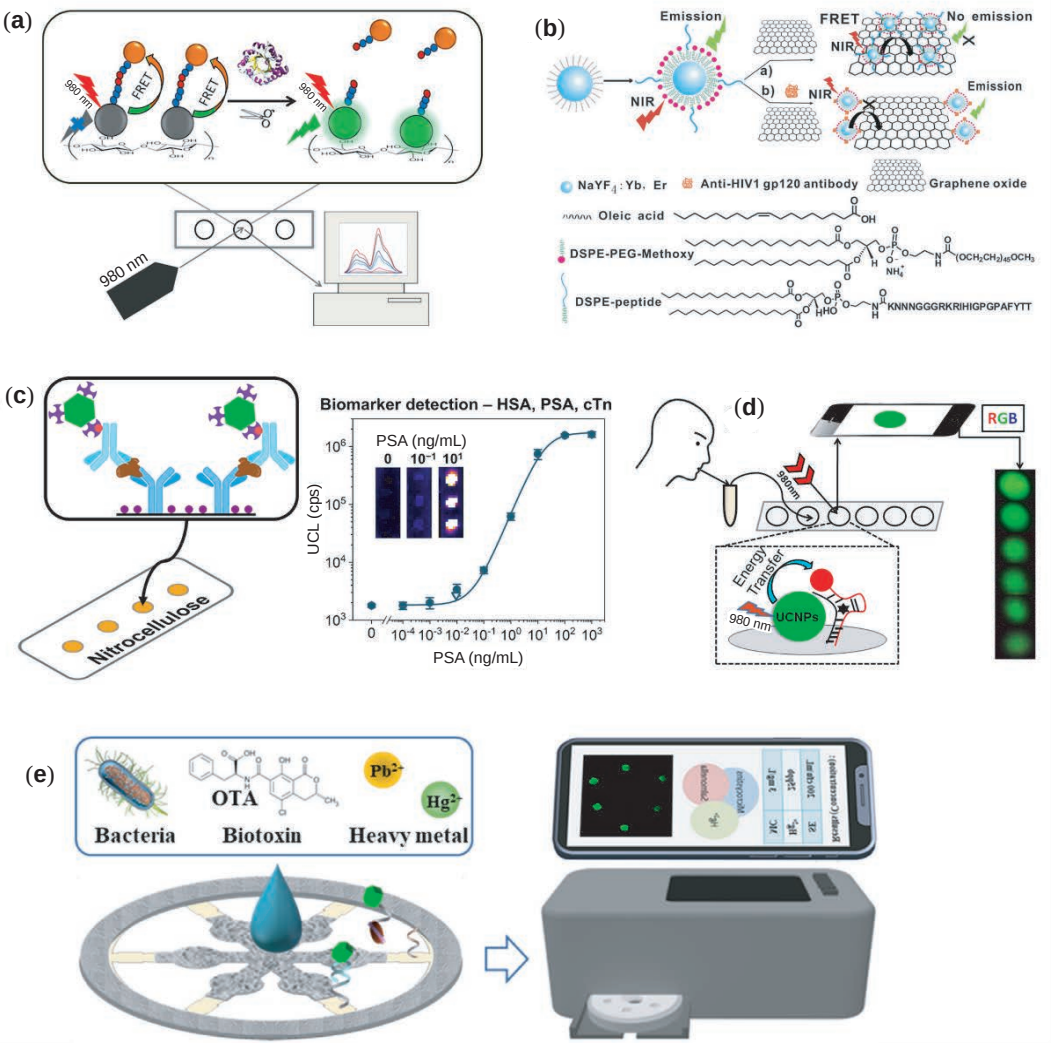

Figure 20 **a.** Schematic illustration of the UC-μPAD for the MMP-2 assay [366]. **b.** Schematic illustration of the upconversion biosensor for the detection of anti-HIV-1 gp120 antibody [367]. **c.** Scheme and detection performance of the dot-blot immunoassay [368]. **d.** Schematic illustration of the UCNPs-based paper device for cocaine field testing [370]. **e.** Schematic illustration of a paper disc for multiplex detection [369]. Reproduced with permission from Ref. [369]. Copyright©2021 Elsevier.

fluorescence resonance energy transfer-based paper biosensor using peptide-functionalized UCNPs for the detection of HIV antibodies in serum samples (Figure 20b). In this system, GO was employed as a luminescence quencher to suppress the background signal, and specific recognition between antibodies and peptide epitopes effectively disrupted the energy transfer, thereby restoring fluorescence intensity. The biosensor exhibited a detection limit of 2 nM (1 nM = 1 × 10^{-9}mol/L) and demonstrated excellent selectivity in complex biological matrices, including human serum. This work illustrated that UCNP-based FRET platforms, when integrated with paper substrates, can significantly enhance diagnostic specificity and robustness, offering an alternative to traditional fluorophores in clinical immunoassays.

In an effort to achieve reliable and accurate quantitative biomarker analysis, Máčala et al. [368] employed UCNPs as high-sensitivity optical reporters in a dot-blot immunoassay designed for detecting multiple clinically relevant protein biomarkers, including human serum albumin, prostate-specific antigen, and cardiac troponin (Figure 20c). The assay achieved impressively low detection limits of 0.19 ng/mL for HSA, 9.4 pg/mL for prostate specific antigen, and 0.62 ng/mL for cardiac troponin (cTn), reflecting a substantial improvement over conventional colorimetric or organic dye-based assays. Furthermore, excellent accuracy and reproducibility were demonstrated, with recovery rates ranging from 79% to 123% in urine and from 89% to 117% in serum samples. These results confirmed that UCNPs offer not only enhanced sensitivity but also excellent batch-to-batch consistency and reproducibility when used in paper-based platforms. Such performance highlights their suitability for clinical diagnostics requiring low detection thresholds, precise quantification, and operational stability across different biological sample types.

To address the growing demand for multiplexed diagnostic assays, Jin et al. [369] developed a paper-based analytical platform that employed aptamer-functionalized UCNPs for the simultaneous detection of diverse environmental and biological contaminants (Figure 20e). These targets included foodborne pathogens such as *Salmonella* (detected at concentrations as low

as 115 CFU/mL, where CFU represents colony-forming unit), mycotoxins like Ochratoxin A and Microcystin-LR (with limits of detection around 3 ng/mL), and heavy metal ions such as Hg^{2+} and Pb^{2+} (detected at 20 and 4 nM, respectively). The system exploited the sharp and distinct emission peaks of different UCNPs to allow spectral separation of multiple signals within a single test zone, thereby enabling reliable multicolor readouts without spectral overlap. Additionally, the anti-Stokes nature of UCNPs' luminescence effectively minimized background interference from both the paper substrate and sample matrix. This multiplexing capability significantly enhances the analytical throughput of paper-based diagnostics and extends their application potential to scenarios requiring parallel quantification of multiple biomarkers or contaminants, including environmental surveillance, clinical screening, and food safety analysis.

A further evolution of UCNPs-integrated μPADs involves the incorporation of smartphone-based detection systems to improve portability, accessibility, and ease of use. Aydindogan et al. [370] reviewed the growing body of research on smartphone-enabled analytical platforms and emphasized how coupling functional nanoparticles, including UCNPs, with mobile imaging capabilities can offer cost-effective and scalable alternatives to conventional fluorescence readers. These platforms utilize smartphone cameras, built-in image analysis software, and wireless communication features to enable rapid, decentralized diagnostics. In a representative study, He et al. [371] developed a UCNPs-based μPAD for the detection of cocaine in saliva, using aptamer-modified probes and capturing the fluorescence signal directly through a smartphone camera under 980 nm excitation (Figure 20d). The system demonstrated high specificity, minimal sample preparation requirements, and a user-friendly interface suitable for on-site POCT. By eliminating the need for bulky instrumentation and trained personnel, smartphone-integrated diagnostic tools significantly lower the barrier to implementation and hold promise for real-time health monitoring, public safety screening, and decentralized clinical diagnostics.

Together, these advances illustrate a clear trajectory in which UCNPs-integrated μPADs have evolved from early proof-of-concept devices into increasingly sophisticated diagnostic platforms with capabilities for quantitative, multiplexed, and portable analysis. By leveraging the unique optical properties of lanthanide-doped materials, such as UCL and TRF, and combining them with the low cost and fabrication simplicity of paper-based devices, these systems provide scalable and adaptable solutions. Their application spans clinical diagnostics at the point of care, field-based environmental testing, and rapid screening in emergency or low-resource settings. Integration with digital technologies, including smartphone-based imaging, further enhances their accessibility and potential for widespread adoption.

Although substantial progress has been made, several challenges must still be addressed to enable broader clinical and commercial translation. Future efforts should prioritize the refinement of UCNPs' surface modification techniques to improve biorecognition [372,373], along with optimization of μPAD designs to enhance fluid handling and reagent stability [374,375]. Standardization in device fabrication is also needed to ensure reproducibility across production batches. In addition, the development of robust and user-friendly signal quantification tools that are compatible with mobile devices will be essential for deployment in real-world settings without specialized personnel [376]. Advancing this field will require close collaboration among chemists, engineers, clinicians, and data scientists to bridge the gap between research innovation and practical application [377].

5.1.2 Chip-based microfluidics

Chip-based microfluidics, also referred to as lab-on-a-chip (LOC) systems, represents a major advancement in miniaturized analytical platforms [378,379]. These systems utilize microfabricated channels and chambers on substrates such as glass, polydimethylsiloxane, or thermoplastics to manipulate fluids with high precision at the microscale. In contrast to paper-based devices (μPADs), chip-based microfluidics offers superior control over fluid flow, reaction timing, and reagent mixing, enabling the execution of more complex bioanalytical processes. The integration of external actuation mechanisms, including electrokinetic driving, pressure-based pumping, or digital droplet manipulation, further enhances their automation capabilities and analytical throughput. These features have led to their broad adoption in biomedical diagnostics, pharmaceutical screening, and environmental monitoring.

The incorporation of lanthanide-doped luminescent materials into chip-based microfluidic systems enhances their analytical performance [380]. UCNPs offer several advantages for microfluidic biosensing, including high photostability, resistance to photobleaching, and sharp emission peaks that facilitate multiplexed detection. Their excitation in the NIR region significantly reduces autofluorescence from biological samples and substrate materials, resulting in higher signal-to-noise ratios compared to conventional fluorophores. Moreover, their long emission lifetimes enable TRF measurements, which effectively suppress short-lived background signals. These optical features make UCNPs ideal for applications requiring high sensitivity, low detection limits, and real-time monitoring within confined microenvironments.

While paper-based platforms are particularly advantageous for low-cost, field-deployable diagnostics, chip-based systems are more suitable for scenarios demanding reproducibility, precision, and compatibility with automated instrumentation. Applications of UCNPs in chip-based microfluidics span a wide range of biomedical functions, including immunoassays, nucleic acid amplification tests, and single-cell analysis. The ability to operate in well-controlled environments with defined reaction conditions positions these systems as promising candidates for the development of integrated POC diagnostics and continuous physiological monitoring tools.

Recent advancements in UCNPs-integrated chip-based microfluidics have expanded their roles well beyond conventional biosensing. These systems now encompass functions such as high-quality UCNPs probe synthesis, biomarker quantification, temperature sensing, immune cell modulation, circulating tumor cell analysis, and clinical diagnostics. This section highlights representative progress in these directions, illustrating how UCNPs-based microfluidic platforms are evolving toward integrated, high-performance biomedical devices.

A key challenge in the development of UCNP-based bioassays lies in achieving uniformity and optical precision during probe

synthesis. Traditional batch synthesis often results in size variability and inconsistent luminescence. To address this, Liu et al. [381] utilized a droplet microfluidic platform to produce multicolor UCNPs-doped polymer microspheres with highly controlled sizes and emission properties (Figure 21b). By adjusting the droplet generation and photopolymerization conditions, microspheres with distinct emission bands were fabricated in a continuous flow, enabling their application in protein detection and multiplexed analysis. This strategy demonstrated how microfluidics can serve not only as an analytical platform but also as a fabrication tool for high-performance luminescent probes.

Beyond material synthesis, chip-based microfluidic platforms have been successfully applied to clinically relevant biomarker detection. One notable example involved the use of digital microfluidics for detecting prostate-specific antigen [382], where magnetic bead enrichment was coupled with UCNPs-based fluorescent readout (Figure 21a). The PDMS-based chip incorporated dedicated chambers for magnetic capture and signal amplification. UCNPs, with their NIR excitation and sharp emission, significantly suppressed background interference, yielding a detection limit of 1.04 pg/mL. The platform demonstrated high specificity and consistent recovery in patient serum samples. Compared to conventional bead-based immunoassays, this approach improved sensitivity by more than an order of magnitude and offered potential for integration with automated laboratory and POC systems.

In another development, UCNPs-functionalized microfluidic chips were applied to viral diagnostics. A multilayer chip structure incorporated a series of filtration and enrichment zones that concentrated viral nucleocapsid proteins from biological fluids [383] (Figure 21c). Detection was performed using UCNPs probes functionalized with viral-specific antibodies and excited under 980 nm irradiation. The resulting fluorescence signals were captured via compact optical readers or mobile phone-based platforms. The assay achieved detection limits in the low picogram per milliliter range, outperforming many commercially available lateral flow devices. The overall process required under 15 min from sample loading to result acquisition, demonstrating strong potential for rapid diagnostic applications in both clinical and emergency settings.

Beyond diagnostics, UCNPs-integrated microfluidic platforms have also been applied to immune cell regulation, offering new possibilities for immunotherapy. The ability to precisely modulate immune cell behavior within a confined microfluidic environment enables controlled investigation of signaling pathways and facilitates the development of optimized therapeutic strategies for cancer, autoimmune disorders, and vaccine design. For instance, one study [384] employed a microfluidic system combined with lanthanide-doped luminescent particles to achieve light-driven activation of immune cells (Figure 22a). By using upconversion-based optical stimulation, immune responses were triggered in a spatially and temporally resolved manner. This approach not only provided insights into intracellular communication but also enabled high-throughput immune profiling with reduced reagent consumption. Such platforms demonstrate promising utility in cell-based immunotherapy screening and offer a new direction for personalized immune regulation technologies.

The detection and characterization of circulating tumor cells are essential for early-stage cancer diagnostics, as these cells serve as key indicators of tumor metastasis. Conventional methods for circulating tumor cell isolation often require complex sample preparation and large volumes of blood, limiting their feasibility in routine clinical workflows. Microfluidic devices, due to their ability to precisely handle small fluid volumes, have emerged as attractive platforms for CTC analysis. In a representative study

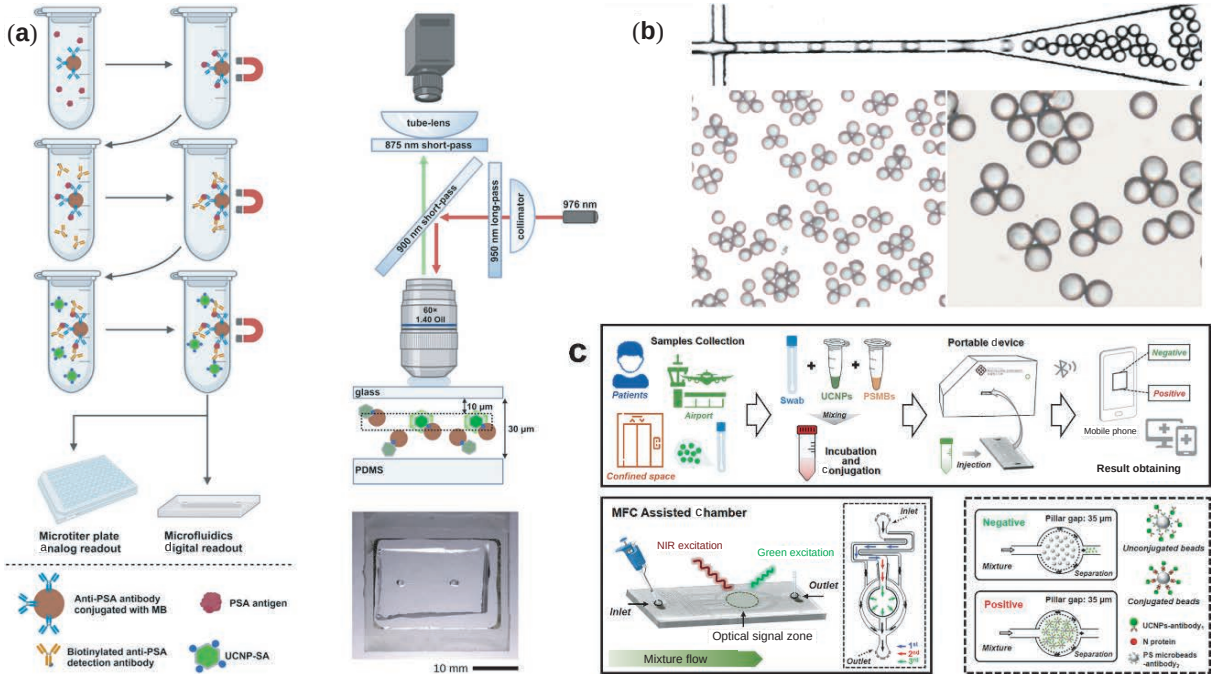

Figure 21 **a.** Principle of the immunoassay [382]. **b.** Bright field microscopy images showing the production of hydrogel using a microfluidic device [381]. **c.** Schematic diagram of the diagnostic platform [383].

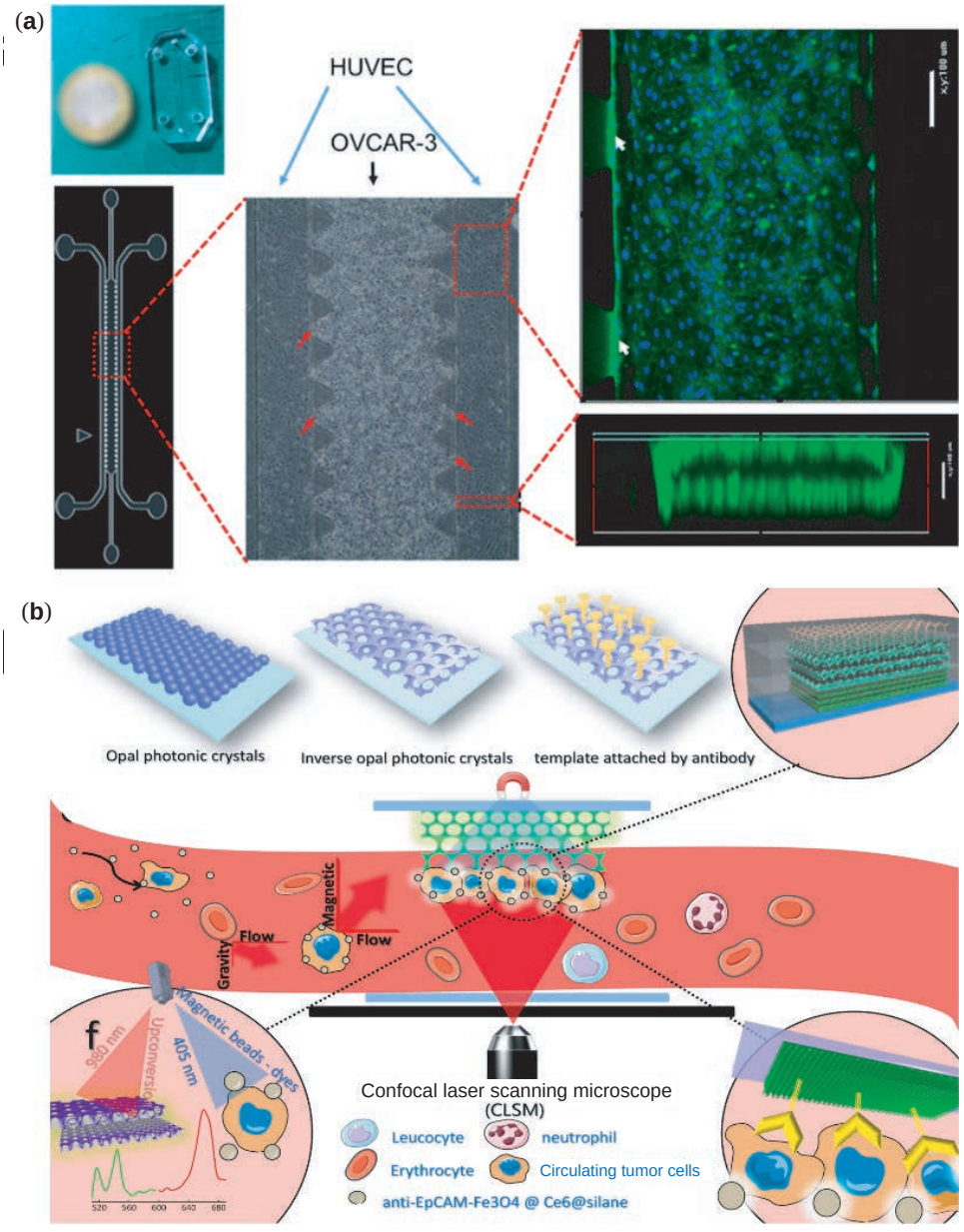

Figure 22 **a.** Photograph and schematic of the microfluidic device [384]. **b.** Schematic diagram of a microfluidic device for capturing and identifying CTCs simultaneously [385]. Reproduced with permission from Refs. [384,385]. Copyright©2019 American Chemical Society and Copyright©2022 Elsevier.

[385], surface-functionalized microchannels were employed to selectively capture CTCs from patient-derived samples (Figure 22b). Simultaneously, UCNPs provided real-time visualization of captured cells and enabled downstream therapeutic intervention. Light-activated photodynamic effects mediated by UCNPs were further used to induce selective apoptosis of tumor cells within the chip, integrating diagnosis and therapy into a single platform. These results highlight the potential for wearable or implantable microfluidic devices that not only monitor metastatic progression but also deliver localized treatment in real time.

Beyond molecular and cellular diagnostics, UCNPs have also been explored as luminescent nanothermometers for *in situ* temperature monitoring within microfluidic environments. Precise thermal control is critical in biochemical reactions, particularly in nucleic acid amplification, enzyme activity assays, and cell culture applications. One system [386] utilized the temperature-dependent emission intensity ratios of UCNPs to construct a microfluidic platform capable of continuous, spatially resolved temperature sensing. This allowed for the accurate measurement of local temperature variations during bioassays, ensuring reproducibility and enhancing the reliability of results. Such integration is especially valuable in wearable microfluidic devices, where body heat or environmental fluctuations may influence diagnostic outcomes. The ability to simultaneously monitor biochemical reactions and thermal conditions greatly enhances the functionality and adaptability of microfluidic biosensing systems.

Together, these applications demonstrate that the integration of UCNPs into chip-based microfluidics has significantly expanded the scope of LOC technologies. From molecular biomarker

detection to real-time physiological monitoring, immune modulation, and localized cancer therapy, UCNPs-enhanced platforms are paving the way toward multifunctional, miniaturized diagnostic tools. Looking forward, several research priorities should be addressed to further advance the field. These include improving the biocompatibility of UCNPs through surface engineering to reduce cytotoxicity, enhancing the stability and reproducibility of microfluidic devices during large-scale production, and incorporating artificial intelligence and machine learning for real-time signal analysis and device control. The continued convergence of material science, biomedical engineering, and clinical research will be crucial for developing next-generation UCNPs-based microfluidic systems capable of meeting the demands of POC diagnostics and personalized medicine. [387-389]

5.2 Lateral flow assays

LFAs represent one of the most widely adopted formats in POC diagnostics, owing to their ease of use, low production cost, and rapid turnaround time [390]. These assays operate on a capillary-driven fluid transport mechanism through porous materials, typically nitrocellulose membranes, allowing for visually interpretable results without the need for complex instrumentation. LFAs have been extensively applied for the detection of infectious agents, pregnancy hormones, cardiac markers, and drug residues, both in clinical settings and in at-home testing scenarios.

While LFAs and μPADs share certain material similarities (cellulose-based substrates), their design philosophies and application contexts differ considerably. μPADs emphasize programmable microchannel design and multiplexing flexibility through customized fluid routing, whereas LFAs prioritize lateral fluid flow across a single strip, enabling simple one-directional assays. Additionally, μPADs are often designed for lab-in-a-chip functionality and integrated with external readout systems, whereas LFAs are optimized for rapid, standalone testing with minimal user intervention. As a result, LFAs are generally more suitable for consumer-grade diagnostics and large-scale public health screening, while μPADs offer greater versatility for research-oriented or custom clinical applications.

A standard LFA strip typically consists of four functional components sequentially mounted on an adhesive backing card: the sample pad, the conjugate pad, the nitrocellulose membrane, and the absorbent pad [391,392]. The sample pad receives the biological specimen (e.g., serum, saliva, or urine) and initiates fluid flow via capillary action. The conjugate pad contains detection probes that are rehydrated upon contact with the sample. As the fluid migrates laterally along the nitrocellulose membrane, target analytes bind to immobilized capture molecules in defined test and control lines, producing detectable signals. The absorbent pad ensures continuous flow by maintaining a capillary pressure gradient. This modular architecture enables compact, low-cost construction and supports scalable production.

Despite their broad utility, traditional LFAs suffer from limited sensitivity and semiquantitative readouts, primarily due to their reliance on colorimetric signals (e.g., gold nanoparticles). To overcome these challenges, lanthanide-doped luminescent materials have recently been integrated into LFAs to improve analytical performance. These materials offer distinct advantages such as sharp emission peaks, excellent photostability, long luminescence lifetimes, and low background interference. Notably, two classes of lanthanide-based detection strategies have gained prominence: UCL using NIR excited UCNPs, and TRF based on long-lifetime lanthanide chelates. These strategies significantly enhance the sensitivity, multiplexing capability, and dynamic range of LFAs, enabling their use in more demanding clinical applications while maintaining ease of use and cost-effectiveness.

The development of upconversion- and TRF-enhanced LFAs has significantly expanded their applicability in biomedical diagnostics, offering superior sensitivity, multiplexing capability, and improved signal-to-noise ratios compared to conventional gold nanoparticle-based LFAs. These advancements have addressed key challenges in detecting low-abundance biomarkers in complex biological matrices, particularly in whole blood and serum samples. Recent studies have demonstrated the integration of UCNPs and TRF probes into LFAs for infectious disease detection, cancer biomarker screening, hormone level monitoring, and environmental analysis, paving the way for next-generation POC diagnostics.

One of the primary applications of UCNPs-enhanced LFAs is in infectious disease diagnostics, where early and ultra-sensitive detection is critical for timely medical intervention. The integration of UCNPs with NIR excitation has improved fluorescence readout efficiency and minimized interference from autofluorescence in biological samples. A recent study [358] demonstrated that the use of UCNPs-based probes in LFAs for whole blood detection provided significantly enhanced emission intensity compared to conventional fluorescent markers such as QDs and organic dyes (Figure 23a). This improvement facilitated lower detection limits for viral antigens, making it feasible for UCNPs-LFAs to rival polymerase chain reaction assays in terms of sensitivity while maintaining the rapid turnaround and portability of conventional lateral flow tests. Similar enhancements have been observed in LFAs for bacterial pathogens, including tuberculosis and drug-resistant Staphylococcus aureus, demonstrating their broad potential in microbiological diagnostics.

Beyond infectious diseases, UCNPs- and TRF-based LFAs have also been extensively studied for cancer biomarker detection, particularly in the quantification of circulating tumor DNA (ctDNA) and tumor-associated proteins. A study [393] utilizing europium-based TRF microspheres for the detection of CA199, a key biomarker for pancreatic cancer, demonstrated that TRF-LFAs could achieve detection limits nearly fourfold lower than conventional colorimetric LFAs (Figure 23b). The time-gated nature of TRF readouts further minimized non-specific background fluorescence, enhancing assay precision. Given the increasing demand for non-invasive cancer screening tools, TRF- and UCNPs-based LFAs offer a promising alternative for rapid and quantitative liquid biopsy applications, reducing reliance on invasive tissue sampling.

Another significant advancement in the field has been the use of oriented antibody immobilization in TRF-LFAs, which has led to substantial improvements in detection sensitivity. A recent study [394] on C-peptide detection in serum utilized a TRF-LFA platform with optimized antibody orientation, achieving a detection limit of 0.005 ng/mL—an order of magnitude lower

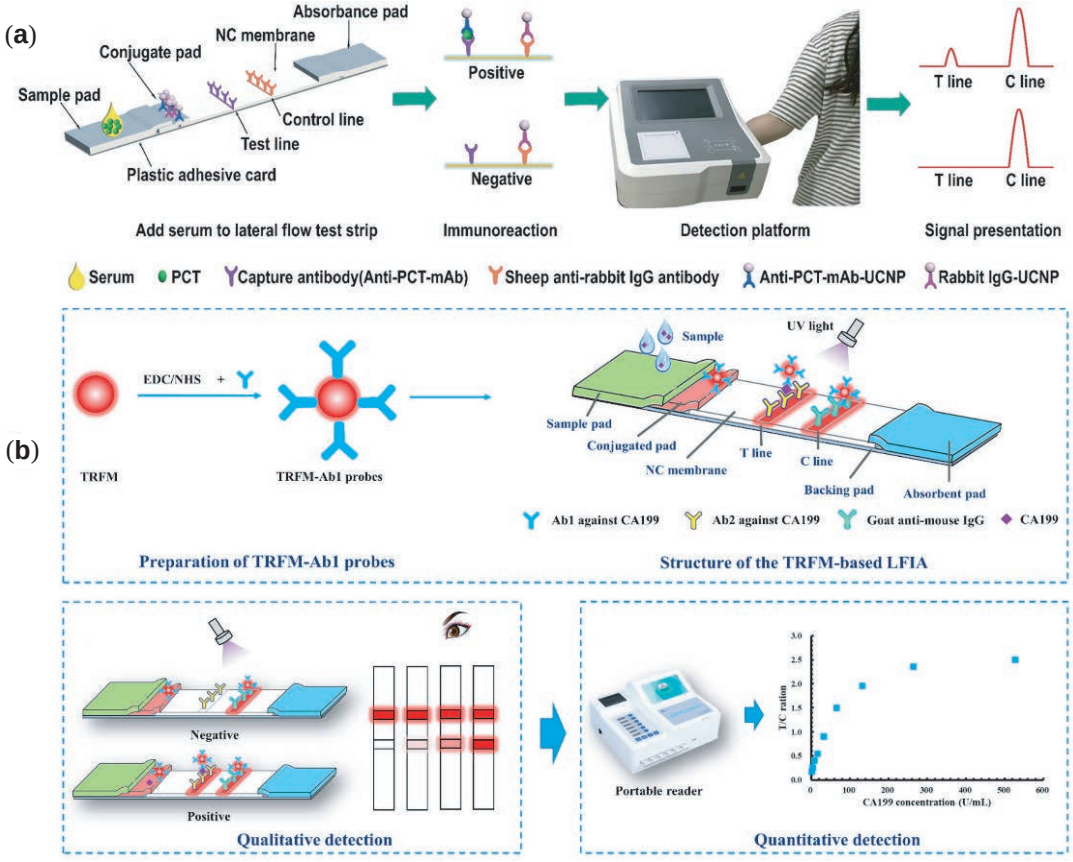

Figure 23 **a.** Schematic illustration of NIR-to-NIR UCNP-based LFAs for detection of sepsis biomarker [358]. **b.** Schematic of the TRFM-based LFIA [393]. Reproduced with permission from Ref. [358]. Copyright©2020 American Chemical Society.

than conventional TRF-LFIAs. The enhanced antigen-binding efficiency provided by precise antibody alignment resulted in improved assay reproducibility and specificity, demonstrating the potential of TRF-LFAs for clinical biomarker quantification.

UCNPs-LFAs have also been explored for hormone and small-molecule analysis, particularly in areas requiring highly sensitive and quantitative readouts [395]. Traditional pregnancy tests based on gold nanoparticles provide qualitative or semi-quantitative results, limiting their clinical utility in hormone level monitoring. The integration of UCNPs probes has enabled real-time fluorescence-based quantification of human chorionic gonadotropin, thyroid-stimulating hormone, and cortisol, allowing for continuous monitoring in clinical and at-home settings. Similar advances have been applied to the detection of illicit drugs and pharmaceutical residues in forensic toxicology, where UCNPs-LFAs have shown remarkable specificity and sensitivity for substances such as opioids, amphetamines, and benzodiazepines.

Beyond human health applications, UCNPs-LFAs have demonstrated broad applicability in food safety and environmental monitoring, particularly for the detection of pesticide residues, heavy metals, and bacterial toxins [396]. The ability of UCNPs probes to generate a stable fluorescence signal under NIR excitation has enabled the development of portable, field-deployable detection systems for agricultural and environmental surveillance. These assays have demonstrated detection limits that are orders of magnitude lower than conventional colorimetric LFAs, highlighting their potential for regulatory compliance and public health monitoring.

While UCNPs-enhanced LFAs have achieved significant advancements in sensitivity, multiplexing, and quantitative accuracy, several challenges continue to limit their broader clinical implementation. One of the main obstacles is the limited availability of compact and low-cost detection hardware that supports NIR excitation or TRF measurements. This shortage restricts the deployment of UCNPs-based LFAs in decentralized and resource-limited environments. In addition, material-related issues such as inconsistencies in nanoparticle synthesis, variability in surface functionalization, and unstable bioconjugation can lead to batch-to-batch fluctuations and hinder reproducibility [397]. Many platforms also lack standardized calibration protocols and validated clinical workflows, which are critical for regulatory approval and clinical acceptance. To address these limitations, future efforts should focus on developing scalable nanoparticle manufacturing, improving bioconjugation chemistry, and creating portable, user-friendly detection systems. Strong interdisciplinary collaboration among material scientists, engineers, and clinicians will be essential to transition UCNPs-based LFA technologies from proof-of-concept systems into reliable diagnostic tools for routine medical practice [376,398].

5.3 Clinical translation

Lanthanide-doped luminescent materials, particularly those based on upconversion and TRF, have shown remarkable performance

in preclinical biomedical applications. Their unique optical properties, such as NIR excitation, minimal background interference, high photostability, and long emission lifetimes, make them ideal candidates for *in vivo* imaging, therapeutic interventions, and biomarker detection in small-animal models. Numerous studies have demonstrated their utility in deep-tissue imaging, fluorescence-guided surgery, PDT, and *in vivo* biosensing [399,400], underscoring their tremendous translational potential. However, despite extensive preclinical success, no UCNPs- or TRF-based technologies have progressed to human clinical trials.

Although several lanthanide-containing pharmaceuticals—most notably gadolinium-based contrast agents (GBCAs)—have been approved for clinical use, these agents are molecular lanthanide chelates with rapid renal clearance and well-established pharmacokinetics [401]. Their clinical behavior differs fundamentally from the lanthanide-doped inorganic nanocrystals discussed in this review. Nanoparticle-based systems such as UCNPs, downconversion particles, and persistent luminescent probes exhibit slow degradation, prolonged retention in organs, and uncertain long-term biosafety, explaining why none of them have yet advanced to human testing.

A central barrier to clinical translation is the lack of comprehensive long-term biosafety data. Because these inorganic nanoparticles are not readily metabolized or excreted, they may accumulate in the liver, spleen, and lymphatic system, raising concerns about chronic toxicity and immune or metabolic interference [402]. Most current toxicological studies are limited to acute or short-term rodent experiments, and long-term biodistribution or clearance studies—particularly in large animals—remain scarce [403]. Regulatory agencies such as the FDA require robust datasets on pharmacokinetics, organ distribution, immune responses, and genotoxicity before permitting human trials, yet such standardized data are not yet available.

Beyond biosafety concerns, successful clinical translation must also be guided by clearly defined regulatory pathways. Future development of lanthanide-doped luminescent nanomaterials should align with established approval frameworks, including the FDA Investigational New Drug (IND) process and the European Medicines Agency (EMA) guidelines for nanomedicine-based products. Compliance with good manufacturing practice (GMP) requirements, scalable production, batch-to-batch consistency, and strict quality control are essential prerequisites for regulatory evaluation and subsequent clinical approval. In parallel, the establishment of standardized methodologies for physicochemical characterization (e.g., particle size distribution, surface charge, coating stability), pharmacokinetics, biodistribution profiling, and long-term toxicity assessment is urgently required to ensure data reproducibility, cross-study comparability, and regulatory confidence.

Compounding these challenges is the absence of regulatory frameworks tailored to luminescent nanomaterials. Unlike gold nanoparticles or iron oxide agents, which have established approval pathways, lanthanide-doped nanomaterials lack reference standards, toxicological classification criteria, and harmonized guidance documents [404,405]. Without clear regulatory benchmarks or validated clinical data, even highly promising preclinical results cannot be translated into clinical action.

In light of these limitations, one promising strategy to accelerate clinical translation is the integration of lanthanide-doped luminescent materials into medical devices. Compared to systemically administered agents, device-embedded luminescent materials present lower biosafety risks because the nanoparticles can be confined within encapsulated or surface-bound architectures, minimizing direct *in vivo* exposure. This approach may simplify regulatory requirements and enable applications such as implantable sensors, optical diagnostic tools, and wearable biosensing patches [406].

5.3.1 Lanthanide-based medical devices

Lanthanide-doped luminescent materials have increasingly attracted interest for integration into advanced medical devices, offering a promising avenue to circumvent the limitations of systemic administration and *in vivo* toxicity encountered in conventional clinical translation. Unlike imaging agents or therapeutic nanoparticles that require intravenous injection and systemic distribution, the incorporation of lanthanide emitters into localized, surface-bound, or implantable devices allows their unique optical properties to be exploited in a confined and controlled context. This strategy significantly enhances biosafety and enables high-performance diagnostics or monitoring while avoiding long-term retention in the body.

Recent studies have demonstrated the feasibility of integrating UCNPs into biomedical devices for real-time monitoring and diagnostic purposes. A notable example, published in *Advanced Materials* (2023) [407], reported the development of an implantable microfluidic-luminescent system for continuous monitoring of hydrogen peroxide (H_2O_2) in tumor metastasis (Figure 24). To overcome the challenge of poor tissue penetration and probe toxicity, the researchers designed a system in which the luminescence-based sensing element was physically separated from deep tissue regions. The device, subcutaneously implanted in rats, comprised a magnetically actuated micropump, a luminescent detection chamber, and microtubing that transferred fluid samples (such as peritoneal ascites or blood) from within the body to the surface detection module. In the chamber, a ratiometric UCNPs probe composed of IR820-sensitized $NaYF_4$:Yb,Er@$NaYF_4$:Yb particles was employed to detect hydroxyl radicals (•OH), a product of H_2O_2 reduction. The UCNPs' emission intensity ratio changed in response to ROS concentration, with IR820 encapsulated in DSPE-PEG to exclude nonspecific interference from other ROS. This system achieved real-time detection with a temporal resolution of 0.01 s and was operational *in vivo* for over 20 days without systemic nanoparticle distribution, paving the way for minimally invasive long-term biochemical monitoring in cancer progression and therapy response.

Complementing this approach, Hou et al. [408] reported in *Nature Biomedical Engineering* (2023) the development of a swallowable capsule dosimeter capable of simultaneously monitoring X-ray dose, gastrointestinal pH, and temperature during cancer RT (Figure 25). The 18 mm × 7 mm capsule incorporated persistent luminescent $NaLuF_4$:Tb@$NaYF_4$ nanoscintillators, a pH-responsive polyaniline film, and integrated wireless electronics. Upon exposure to X-rays, the nanoscintillators emitted persistent luminescence that was transmitted via a flexible optical fiber to an external detector, enabling accurate, real-time dose

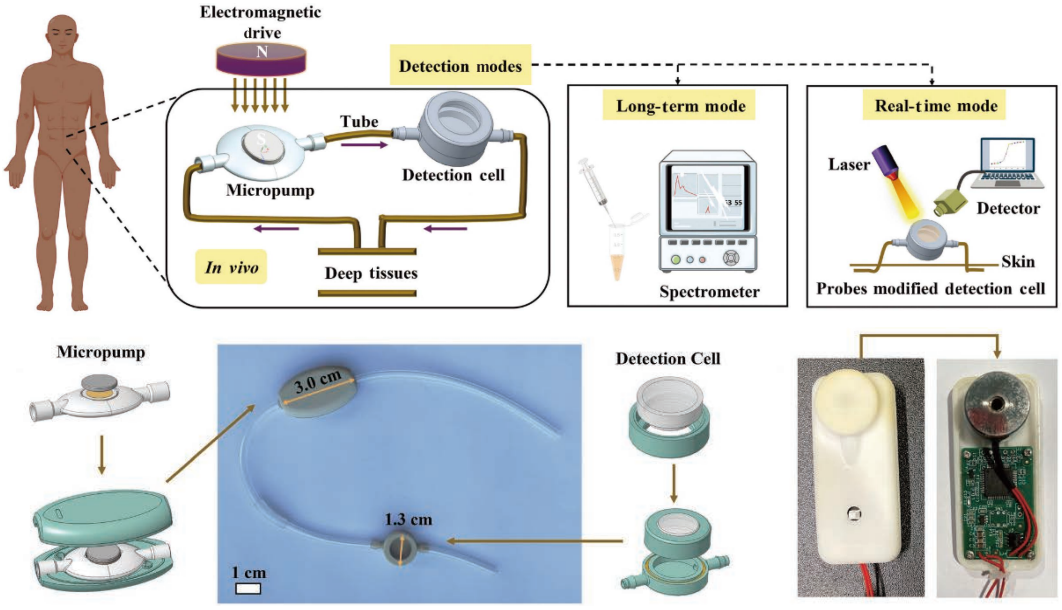

Figure 24 The developed detection modes and relevant devices [407]. Reproduced with permission from Ref. [407].Copyright©2023 Wiley-VCH.

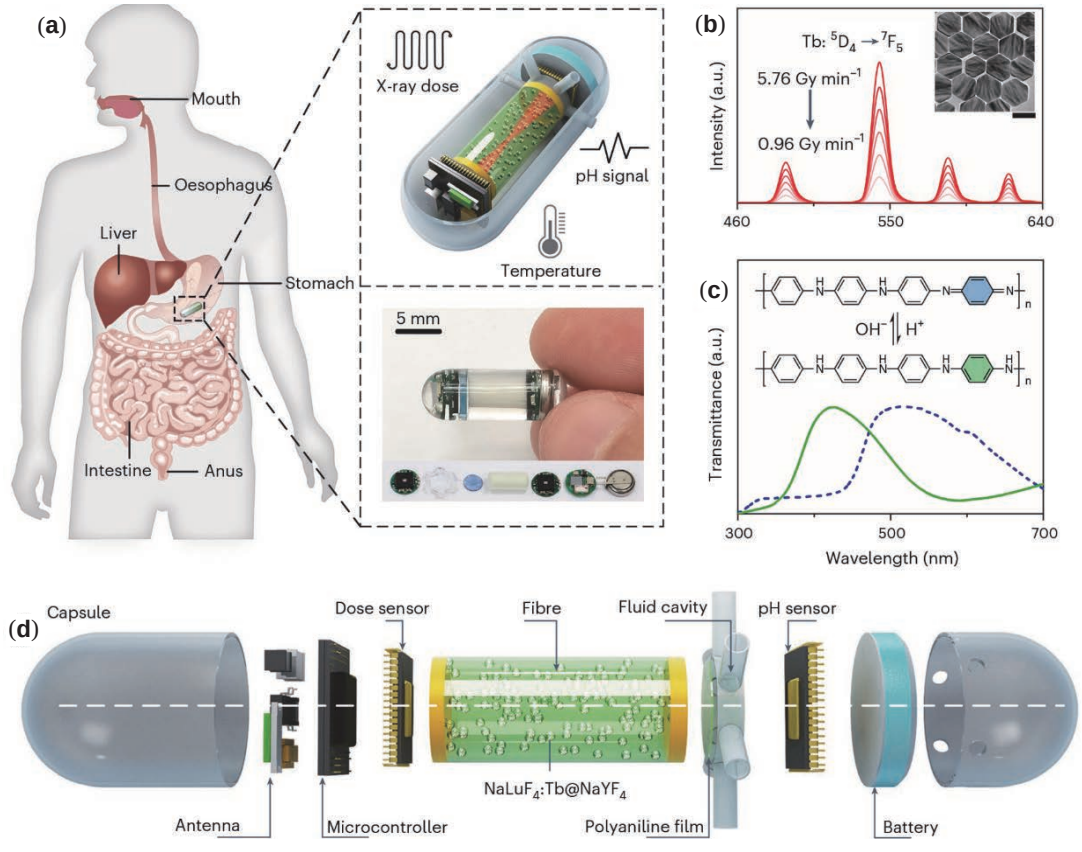

Figure 25 **a.** The dosimeter in schematic and real views. **b.** Radioluminescence spectra of nanoscintillators irradiated with different dose rates. **c.** Transmission spectra of the polyaniline film recorded in acidic and basic solutions. **d.** The all-in-one capsule dosimeter in an exploded three-dimensional view [408]. Reproduced with permission from Ref. [408]. Copyright©2023 Springer Nature

readouts. Simultaneously, this afterglow emission also served as an excitation source for internal pH sensing, thereby eliminating the need for external light sources. The capsule dynamically sampled gastric fluids during its transit, and machine learning algorithms were used to correct for afterglow decay and thermal influences, enhancing signal interpretation. *In vivo* tests in rabbits demonstrated high sensitivity in detecting both radiation dose (error <0.01 Gy/min(1 Gy/min = 1 J/(kg·min))) and pH shifts (resolution of 0.02 pH units), confirming its potential as a real-time, minimally invasive tool for RT monitoring.

Together, these innovations illustrate how lanthanide-based optical materials can be seamlessly integrated into functional medical devices, offering new pathways for clinical translation by mitigating the biocompatibility and safety concerns associated with systemic administration. Device-based applications represent a compelling strategy to unlock the clinical potential of lanthanide-doped luminescence, enabling real-time, localized, and longitudinal health monitoring with high sensitivity and precision.

The integration of lanthanide-doped luminescent materials into medical devices offers a strategically advantageous route for clinical translation. Unlike systemically administered nanoparticles, device-bound UCNPs or TRF materials can localize luminescent components to a confined environment, thereby minimizing toxicity, avoiding systemic circulation, and simplifying regulatory pathways. As illustrated by recent implantable and ingestible prototypes, this approach enables long-term, high-sensitivity biosensing without necessitating direct exposure of luminescent agents to internal tissues or organs.

To capitalize on this potential, future work should prioritize the co-design of luminescent materials and medical-grade device platforms. This includes engineering robust encapsulation strategies for UCNPs or TRF probes to ensure stability, developing microfluidic or fiber-optic interfaces for efficient biofluid sampling and light delivery, and advancing wireless, battery-free designs for real-time data transmission. Furthermore, early engagement with clinical collaborators and regulatory authorities will be critical to define standardized safety evaluation protocols and identify use cases with high unmet medical need.

Importantly, many of the barriers that impede systemic applications, such as long-term biocompatibility and unclear elimination pathways, are less problematic in confined device-based contexts. As such, the medical device route provides a viable and accelerated path for realizing the clinical benefits of lanthanide luminescent technology. With continued interdisciplinary collaboration and application-focused innovation, luminescent device platforms may become the first wave of lanthanide-based technologies to enter routine clinical use.

5.3.2 Device compatibility for point-of-care diagnostics

A pivotal advantage of LnNPs lies in their intrinsic compatibility with simplified, low-cost detection devices, which is a fundamental requirement for the realization of decentralized POC diagnostics [409]. Unlike conventional organic fluorophores or QDs, which often necessitate expensive excitation sources (e.g., high-power UV/Vis lamps) and highly sensitive detectors (e.g., photomultiplier tubes) to overcome background noise, LnNPs offer unique optical properties that facilitate instrument miniaturization [410].

First, the ability to excite LnNPs using NIR light allows for the utilization of compact, commercially available CW laser diodes as excitation sources. These components are significantly smaller, cheaper, and more energy-efficient than the excitation hardware required for traditional fluorescence, drastically reducing the overall footprint of the diagnostic device. Second, the exceptionally long luminescence lifetimes of LnNPs (ranging from microseconds to milliseconds) enable the implementation of time-resolved photoluminescence (TRPL) detection [411]. By applying a simple time-gating mechanism, the long-lived signal from LnNPs can be temporally separated from the short-lived (<10 ns) autofluorescence inherent to biological matrices and support materials [7]. This "optical silence" allows for the elimination of complex and costly optical filters. Consequently, high-sensitivity detection can be achieved using standard, cost-effective complementary metal-oxide-semiconductor (CMOS) sensors or charge-coupled devices (CCD), rather than expensive photon-counting detectors.

A specific example of this compatibility is the integration of LnNPs with smartphone-based platforms. Recent advancements have demonstrated that the built-in cameras of smartphones, when coupled with simple add-on accessories (such as a 980 nm laser diode and a basic long-pass filter), can serve as sophisticated readout units for LFAs and microfluidic chips. For instance, recent studies have highlighted the development of smartphone-based sensors that utilize the UCL of LnNPs for the background-free quantification of biomarkers, bridging the gap between laboratory-grade sensitivity and consumer-electronics portability [412,413]. This seamless integration with ubiquitous mobile technology underscores the immense commercial potential of LnNPs in making high-performance diagnostics accessible in resource-limited settings.

6. Discussion and perspectives

6.1 Current limitations

In this review, we summarize and discuss the methods to enhance the optical properties of lanthanide-doped luminescent materials and explore their emerging applications in biological and medical fields. Due to the exceptional optical properties, including long emission lifetimes, narrow emission bandwidths, and remarkable photostability, lanthanide-doped luminescent materials have garnered significant attention in optical detection and imaging, particularly in biological and medical fields.

In order to accelerate the practical implementation of lanthanide nanoprobes in biological and medical applications, the biocompatibility and long-term biosafety issues of lanthanide nanoprobes should also be taken into account. These factors must be addressed to facilitate their broader adoption in medicine. Ethical concerns regarding the use of luminescent materials in humans remain significant barriers.

6.1.1 Biocompatibility and long-term safety considerations

The biocompatibility of lanthanide-doped materials is a crucial determinant of their suitability for biomedical applications. While certain formulations have demonstrated low cytotoxicity *in vitro*, their interactions with biological systems remain complex and not fully understood. The potential for nanoparticle aggregation, unintended biodistribution, and interactions with cellular components necessitates comprehensive assessments to mitigate adverse effects. In particular, the absence of biodegradable frameworks in many lanthanide-based nanomaterials may lead to their accumulation in tissues and organs under chronic or repeated exposure, highlighting the need for more systematic evaluation of their long-term physiological impact.

Long-term biosafety, therefore, represents one of the most

critical and unresolved limitations impeding clinical translation. Because LnNPs are inorganic crystalline materials that degrade extremely slowly in physiological environments, they can persist in organs such as the liver, spleen, and lymphatic system for extended periods, raising concerns regarding chronic inflammation, immune activation, and metabolic disruption. Existing studies predominantly address acute or short-term toxicity in rodent models, whereas rigorous long-term assessments—particularly in large animals—remain scarce. Furthermore, the bioelimination pathways of these particles are still poorly defined, with inefficient renal or hepatobiliary clearance frequently reported. The absence of standardized regulatory protocols and reference materials further complicates cross-study comparisons. Collectively, these challenges underscore that long-term biosafety is not only an important concern but also a fundamental barrier that must be addressed before lanthanide-based luminescent materials can progress toward human clinical application.

6.1.2 Challenges in human application and regulatory constraints

Despite their promise in preclinical research, lanthanide-doped luminescent materials have yet to receive regulatory approval for human use, largely due to unresolved safety concerns and stringent requirements imposed by agencies such as the FDA. The potential risks associated with their long-term retention in the body, coupled with the absence of standardized toxicity assessments, present substantial regulatory hurdles. Furthermore, ethical considerations surrounding the introduction of inorganic nanomaterials into the human body necessitate rigorous risk-benefit evaluations, particularly in applications involving systemic administration.

6.2 Future directions

6.2.1 Material innovations

One of the foremost challenges limiting the clinical translation of lanthanide-doped materials is their inherently low absorption cross-section, which results in inefficient excitation and suboptimal luminescence output. To address this, recent research has focused on designing advanced host lattices, energy-transfer strategies, and nanostructuring techniques to improve their optical efficiency. Rationally engineered core-shell architectures, for instance, have demonstrated enhanced UCL by suppressing surface quenching and optimizing energy-migration pathways. Additionally, the integration of sensitizers such as organic dyes or plasmonic nanostructures has been explored to amplify absorption cross-sections, thereby increasing luminescence intensity under biologically relevant excitation conditions.

Beyond optical performance, the biocompatibility and biodegradability of lanthanide-based materials remain critical concerns for clinical applications. The development of biocompatible surface coatings and biodegradable host matrices is an essential step toward ensuring their long-term safety. Strategies such as the incorporation of silica, lipid, or polymeric coatings have shown promise in improving colloidal stability and reducing cytotoxicity. Moreover, efforts to design lanthanide-based materials that undergo controlled degradation and clearance through renal or hepatic pathways will be crucial to mitigating concerns related to long-term accumulation in biological tissues.

Importantly, AI-guided materials informatics, bioinformatics, and machine learning are emerging as powerful tools for designing next-generation photon conversion materials with enhanced performance. Recent studies clearly demonstrate their accelerating impact on optical materials discovery. Deep-learning models such as DeepMind's GNoME [414] predict the stability of vast numbers of hypothetical inorganic materials, offering guidance for identifying optimal host lattices and dopant configurations for lanthanide systems. Autonomous multi-agent platforms like Coscientist (or A-Lab/MatterGen) [415] further enable closed-loop ideation, experimentation, and optimization, rapidly proposing new high-efficiency compositions. Inverse-design frameworks that combine generative models with active learning can generate structures with targeted properties, providing efficient screening routes for materials with improved absorption cross-sections, reduced nonradiative loss, or controlled degradation behavior. Additionally, large-language-model-based symbolic regression is beginning to uncover interpretable structure–property relationships, offering new insights into nano–bio interactions relevant to biosafety.

6.2.2 Device integration

For lanthanide-doped luminescent materials to achieve clinical utility, their integration into existing medical devices and diagnostic platforms must be prioritized. The compatibility of these materials with conventional optical imaging and sensing systems offers a promising avenue for translation, particularly in the development of next-generation bioimaging probes, wearable sensors, and implantable devices. One particularly compelling direction involves the incorporation of LnNPs into fiber-optic and endoscopic imaging systems, leveraging their NIR excitation and emission for deep-tissue imaging with minimal background interference. Similarly, their integration into POC diagnostic assays, such as time-resolved luminescence-based lateral flow tests and microfluidic biosensors, has the potential to enhance sensitivity and multiplexing capabilities in disease detection. Additionally, the ability of lanthanide-doped materials to serve as optical contrast agents in multimodal imaging—combining luminescence with MRI, CT, or ultrasound—opens new possibilities for precision diagnostics and guided interventions.

6.2.3 Interdisciplinary collaboration

The successful translation of lanthanide-doped materials from laboratory research to clinical practice requires strong interdisciplinary collaboration among materials scientists, chemists, biologists, and medical professionals. Addressing the challenges of biocompatibility, safety, and regulatory approval necessitates a systematic approach that integrates nanomaterials research with toxicology studies, pharmacokinetics assessments, and clinical validation. Collaboration with regulatory agencies is essential to establishing standardized safety protocols and addressing the stringent requirements for medical approval. Given that lanthanide-doped materials have yet to receive FDA approval for human use, early engagement with regulatory bodies can facilitate the development of guidelines for their clinical evaluation. Moreover, partnerships with industry stakeholders will be instrumental in scaling up synthesis protocols, ensuring reproducibility, and

adapting these materials for practical medical applications.

By fostering synergies between disciplines, advancing material design, and aligning with clinical needs, lanthanide-doped luminescent materials hold the potential to revolutionize biomedical imaging and diagnostics. Strategic innovations in materials engineering, seamless integration into medical devices, and cross-disciplinary collaborations will be key to unlocking their full potential and accelerating their adoption in clinical medicine.

Authors' contributions Chang Jiang drafted Sects. 1–3 and 6. Xindong Wang drafted Sect. 5. Hui Li drafted Sect. 4.

Compliance and ethics The author(s) declare that they have no conflict of interest.

Funding This work was supported by the National Natural Science Foundation of China (51972084, 52272270, 52302118), the key Technology Research and Industrialization Demonstration Project of Qingdao (25-1-1-gjgg-1-gx), the Outstanding Young Scholars Project of the Natural Science Foundation of Heilongjiang Province, China (JJ2023JQ0025), the Opening Project of State Key Laboratory of Space Power Sources (YF07050123F2531), the Young Scientist Workshop (Harbin Institute of Technology) (AUGA5710094420), the Fundamental Research Funds for the Central Universities, China (AUGA5710052614, HIT.OCEF.2023041), and the Basic Research Program of Jiangsu (BK20251294).

References

1. Wang F, Liu X. Recent advances in the chemistry of lanthanide-doped upconversion nanocrystals. Chem Soc Rev. 2009; 38: 976.
2. Prodi L, Rampazzo E, Rastrelli F, Speghini A, Zaccheroni N. Imaging agents based on lanthanide doped nanoparticles. Chem Soc Rev. 2015; 44: 4922–52.
3. Liu Y, Tu D, Zhu H, Chen X. Lanthanide-doped luminescent nanoprobes: Controlled synthesis, optical spectroscopy, and bioapplications. Chem Soc Rev. 2013; 42: 6924.
4. Chen G, Yang C, Prasad PN. Nanophotonics and nanochemistry: Controlling the excitation dynamics for frequency up- and down-conversion in lanthanide-doped nanoparticles. Acc Chem Res. 2013; 46: 1474–86.
5. Li H, Wang X, Ohulchanskyy TY, Chen G. Lanthanide-doped near-infrared nanoparticles for biophotonics. Adv Mater. 2021; 33: 2000678.
6. Zhou B, Shi B, Jin D, Liu X. Controlling upconversion nanocrystals for emerging applications. Nature Nanotech. 2015; 10: 924–36.
7. Li H, Tan M, Wang X, Li F, Zhang Y, Zhao L, et al. Temporal multiplexed *in vivo* upconversion imaging. J Am Chem Soc. 2020; 142: 2023–30.
8. Zhu X, Wang X, Zhang H, Zhang F. Luminescence lifetime imaging based on lanthanide nanoparticles. Angew Chem Int Ed. 2022; 61: e202209378.
9. Wang F, Liu X. Multicolor tuning of lanthanide-doped nanoparticles by single wavelength excitation. Acc Chem Res. 2014; 47: 1378–85.
10. Koshevaya ED, Khramov EV, Svetogorov RD, Krasnov AG, Martakov IS, Shishkin II, et al. Stokes and anti-stokes luminescent rare-earth-doped tantalum oxide nanoparticles. Inorg Chem. 2023; 62: 10369–81.
11. Maciejewska K, Marciniak L. Multimodal Stokes and Anti-Stokes luminescent thermometers based on $GdP5O_{14}$ Co-doped with Cr^{3+} and Nd^{3+} ions. Chem Eng J. 2020; 402: 126197.
12. Zhu X, Su Q, Feng W, Li F. Anti-Stokes shift luminescent materials for bioapplications. Chem Soc Rev. 2017; 46: 1025–39.
13. Fan J, Han C, Yang G, Song B, Xu R, Xiang C, et al. Recent progress of quantum dots light-emitting diodes: Materials, device structures, and display applications. Adv Mater. 2024; 36: 2312948.
14. Chen M, Ma J, Feng Y, Wu Y, Hu G, Liu X. Advanced characterization enables a new era of efficient carbon dots electrocatalytic reduction. Coord Chem Rev. 2025; 535: 216612.
15. Baghdasaryan A, Dai H. Molecular gold nanoclusters for advanced NIR-II bioimaging and therapy. Chem Rev. 2025; 125: 5195–227.
16. Liu Q, Feng W, Yang T, Yi T, Li F. Upconversion luminescence imaging of cells and small animals. Nat Protoc. 2013; 8: 2033–44.
17. Zhao M, Li B, Fan Y, Zhang F. *In vivo* assembly and disassembly of probes to improve near-infrared optical bioimaging. Adv Healthc Mater. 2019; 8: 1801650.
18. Zhou L, Wang R, Yao C, Li X, Wang C, Zhang X, et al. Single-band upconversion nanoprobes for multiplexed simultaneous *in situ* molecular mapping of cancer biomarkers. Nat Commun. 2015; 6: 6938.
19. Michalet X, Pinaud FF, Bentolila LA, Tsay JM, Doose S, Li JJ, et al. Quantum dots for live cells, *in vivo* imaging, and diagnostics. Science. 2005; 307: 538–44.
20. Hong G, Antaris AL, Dai H. Near-infrared fluorophores for biomedical imaging. Nat Biomed Eng. 2017; 1: 10.
21. Wu S, Han G, Milliron DJ, Aloni S, Altoe V, Talapin DV, et al. Non-blinking and photostable upconverted luminescence from single lanthanide-doped nanocrystals. Proc Natl Acad Sci USA. 2009; 106: 10917–21.
22. Chen C, Wang F, Wen S, Su QP, Wu MCL, Liu Y, et al. Multi-photon near-infrared emission saturation nanoscopy using upconversion nanoparticles. Nat Commun. 2018; 9: 3290.
23. Mettenbrink EM, Yang W, Wilhelm S. Bioimaging with upconversion nanoparticles. Adv Photonics Res. 2022; 3: 2200098.
24. Zhang KY, Yu Q, Wei H, Liu S, Zhao Q, Huang W. Long-lived emissive probes for time-resolved photoluminescence bioimaging and biosensing. Chem Rev. 2018; 118: 1770–839.
25. Yi Z, Luo Z, Qin X, Chen Q, Liu X. Lanthanide-activated nanoparticles: A toolbox for bioimaging, therapeutics, and neuromodulation. Acc Chem Res. 2020; 53: 2692–704.
26. Bagheri A, Arandiyan H, Boyer C, Lim M. Lanthanide-doped upconversion nanoparticles: Emerging intelligent light-activated drug delivery systems. Adv Sci. 2016; 3: 1500437.
27. Du K, Feng J, Gao X, Zhang H. Nanocomposites based on lanthanide-doped upconversion nanoparticles: Diverse designs and applications. Light Sci Appl. 2022; 11: 222.
28. Liu B, Chen Y, Li C, He F, Hou Z, Huang S, et al. Poly(acrylic acid) modification of Nd^{3+}-sensitized upconversion nanophosphors for highly efficient UCL imaging and pH-responsive drug delivery. Adv Funct Mater. 2015; 25: 4717–29.
29. Wang L, Han S, Li C, Tu D, Chen X. Lanthanide-doped inorganic nanoprobes for luminescent assays of biomarkers. Acc Mater Res. 2023; 4: 193–204.
30. Huang P, Zheng W, Zhou S, Tu D, Chen Z, Zhu H, et al. Lanthanide-doped LiLuF4 upconversion nanoprobes for the detection of disease biomarkers. Angew Chem Int Ed. 2014; 53: 1252–7.
31. Liu Y, Tu D, Zhu H, Ma E, Chen X. Lanthanide-doped luminescent nanobioprobes: From fundamentals to biodetection. Nanoscale. 2013; 5: 1369–84.
32. Liu Y, Meng X, Bu W. Upconversion-based photodynamic cancer therapy. Coord Chem Rev. 2019; 379: 82–98.
33. Tian G, Zhang X, Gu Z, Zhao Y. Recent advances in upconversion nanoparticles-based multifunctional nanocomposites for combined cancer therapy. Adv Mater. 2015; 27: 7692–712.
34. Xu J, Xu L, Wang C, Yang R, Zhuang Q, Han X, et al. Near-infrared-triggered photodynamic therapy with multitasking upconversion nanoparticles in combination with checkpoint blockade for immunotherapy of colorectal cancer. ACS Nano. 2017; 11: 4463–74.
35. Boyer JC, Vetrone F, Cuccia LA, Capobianco JA. Synthesis of colloidal upconverting $NaYF_4$ nanocrystals doped with Er^{3+}, Yb^{3+} and Tm^{3+}, Yb^{3+} via thermal decomposition of lanthanide trifluoroacetate precursors. J Am Chem Soc. 2006; 128: 7444–5.
36. Ye X, Collins JE, Kang Y, Chen J, Chen DTN, Yodh AG, et al. Morphologically controlled synthesis of colloidal upconversion nanophosphors and their shape-directed self-assembly. Proc Natl Acad Sci USA. 2010; 107: 22430–5.
37. Zhong Y, Tian G, Gu Z, Yang Y, Gu L, Zhao Y, et al. Elimination of photon quenching by a transition layer to fabricate a quenching-shield sandwich structure for 800 nm excited upconversion luminescence of Nd^{3+}-sensitized nanoparticles. Adv Mater. 2014; 26: 2831–7.
38. Shen J, Chen G, Ohulchanskyy TY, Kesseli SJ, Buchholz S, Li Z, et al. Tunable near infrared to ultraviolet upconversion luminescence enhancement in (α-$NaYF_4$:Yb,Tm)/CaF_2 core/shell nanoparticles for *in situ* real-time recorded biocompatible photoactivation. Small. 2013; 9: 3213–7.
39. Mai HX, Zhang YW, Sun LD, Yan CH. Size- and phase-controlled synthesis of monodisperse $NaYF_4$:Yb,Er nanocrystals from a unique delayed nucleation pathway monitored with upconversion spectroscopy. J Phys Chem C. 2007; 111: 13730–9.
40. Ehlert O, Thomann R, Darbandi M, Nann T. A four-color colloidal multiplexing nanoparticle system. ACS Nano. 2008; 2: 120–4.
41. Chan EM, Han G, Goldberg JD, Gargas DJ, Ostrowski AD, Schuck PJ, et al. Combinatorial discovery of lanthanide-doped nanocrystals with spectrally pure upconverted emission. Nano Lett. 2012; 12: 3839–45.
42. You W, Tu D, Li R, Zheng W, Chen X. "Chameleon-like" optical behavior of lanthanide-doped fluoride nanoplates for multilevel anti-counterfeiting applications. Nano Res. 2019; 12: 1417–22.
43. Ke J, Lu S, Li Z, Shang X, Li X, Li R, et al. Multiplexed intracellular detection based on dual-excitation/dual-emission upconversion nanoprobes. Nano Res. 2020; 13: 1955–61.
44. Yi G, Lu H, Zhao S, Ge Y, Yang W, Chen D, et al. Synthesis characterization and biological application of size-controlled nanocrystalline $NaYF_4$:Yb,Er infrared-to-visible up-conversion phosphors. Nano Lett. 2004; 4: 2191–6.
45. Heer S, Kömpe K, Güdel HU, Haase M. Highly efficient multicolour upconversion emission in transparent colloids of lanthanide-doped $NaYF_4$ nanocrystals. Adv Mater. 2004; 16: 2102–5.
46. Li Z, Zhang Y, Jiang S. Multicolor core/shell-structured upconversion fluorescent nanoparticles. Adv Mater. 2008; 20: 4765–9.

47. Li Z, Zhang Y. An efficient and user-friendly method for the synthesis of hexagonal-phase $NaYF_4$:Yb,Er/Tm nanocrystals with controllable shape and upconversion fluorescence. Nanotechnology. 2008; 19: 345606.
48. Chen Y, Johnson E, Peng X. Formation of monodisperse and shape-controlled MnO nanocrystals in non-injection synthesis: Self-focusing via ripening. J Am Chem Soc. 2007; 129: 10937–47.
49. Hayashi H, Hakuta Y. Hydrothermal synthesis of metal oxide nanoparticles in supercritical water. Materials. 2010; 3: 3794–817.
50. Wang F, Han Y, Lim CS, Lu Y, Wang J, Xu J, et al. Simultaneous phase and size control of upconversion nanocrystals through lanthanide doping. Nature. 2010; 463: 1061–5.
51. Zhang F, Wan Y, Yu T, Zhang F, Shi Y, Xie S, et al. Uniform nanostructured arrays of sodium rare-earth fluorides for highly efficient multicolor upconversion luminescence. Angew Chem. 2007; 119: 8122–5.
52. Jiao M, Jing L, Liu C, Hou Y, Huang J, Wei X, et al. Differently sized magnetic/upconversion luminescent $NaGdF_4$:Yb,Er nanocrystals: Flow synthesis and solvent effects. Chem Commun. 2016; 52: 5872–5.
53. Malekzadeh M, Mane VV, Xuan Z, Ohulchanskyy TY, Swihart MT. Laser pyrolysis synthesis of upconverting lanthanide-doped $NaYF_4$ nanocrystals for anticounterfeiting applications. ACS Appl Nano Mater. 2023; 6: 3704–17.
54. León JJ, Oetiker N, Torres N, Bruna N, Oskolkov E, Lei P, et al. Microbial green synthesis of luminescent terbium sulfide nanoparticles using *E. Coli*: A rare earth element detoxification mechanism. Microb Cell Fact. 2024; 23: 248.
55. Oetiker N, León JJ, Swihart M, Chen K, Pfeifer BA, Dutta A, et al. Unlocking nature's brilliance: Using Antarctic extremophile Shewanella baltica to biosynthesize lanthanide-containing nanoparticles with optical up-conversion. J Nanobiotechnol. 2024; 22: 637.
56. Chen D, Huang P, Yu Y, Huang F, Yang A, Wang Y. Dopant-induced phase transition: A new strategy of synthesizing hexagonal upconversion $NaYF_4$ at low temperature. Chem Commun. 2011; 47: 5801.
57. Lei P, An R, Yao S, Wang Q, Dong L, Xu X, et al. Ultrafast synthesis of novel hexagonal phase NaBiF4 upconversion nanoparticles at room temperature. Adv Mater. 2017; 29: 1700505.
58. Fu J, Hu X, Luan F, Li G, Guo D. Optimum synthesis and properties of $NaBiF_4$: Yb/Er upconversion nanoparticles. Ceram Int. 2019; 45: 24365–74.
59. Debasu ML, Riedl JC, Rocha J, Carlos LD. The role of Li^+ in the upconversion emission enhancement of $(YYbEr)_2O_3$ nanoparticles. Nanoscale. 2018; 10: 15799–808.
60. Pei S, Ge X, Sun L. Metal ions doping for boosting luminescence of lanthanide-doped nanocrystals. Front Chem. 2020; 8: 610481.
61. Devi S, Luwang MN. Deciphering the role of temperature in Li^+ co-dopant occupancy in $BaYF_5$:Yb^{3+},Er^{3+} up-converting nanocrystals and its structure–property relationship. J Chem Phys. 2021; 154: 094707.
62. Chukova O, Nedilko SA, Nedilko SG, Voitenko T, Slepets A, Androulidaki M, et al. Strong Eu^{3+} luminescence in La1-*x*-*y*Er_x/2Eu_x/2Ca_yVO4 nanocrystals: The result of co-doping optimization. J Lumin. 2022; 242: 118587.
63. Ming J, Xie Z, Wu J, Zhang F. Synthesis of transition metal-sensitized lanthanide near-infrared luminescent nanoparticles. Nat Protoc. 2025.
64. Yi GS, Chow GM. Water-soluble $NaYF_4$:Yb,Er(Tm)/$NaYF_4$/polymer core/shell/shell nanoparticles with significant enhancement of upconversion fluorescence. Chem Mater. 2007; 19: 341–3.
65. Qian HS, Zhang Y. Synthesis of hexagonal-phase core-shell $NaYF_4$ nanocrystals with tunable upconversion fluorescence. Langmuir. 2008; 24: 12123–5.
66. Chen G, Shen J, Ohulchanskyy TY, Patel NJ, Kutikov A, Li Z, et al. (α-$NaYbF_4$:Tm^{3+})/CaF_2 core/shell nanoparticles with efficient near-infrared to near-infrared upconversion for high-contrast deep tissue bioimaging. ACS Nano. 2012; 6: 8280–7.
67. Chen B, Wang F. $NaYbF_4$@CaF_2 core–satellite upconversion nanoparticles: One-pot synthesis and sensitive detection of glutathione. Nanoscale. 2018; 10: 19898–905.
68. Cao C, Xue M, Zhu X, Yang P, Feng W, Li F. Energy transfer highway in Nd^{3+}-sensitized nanoparticles for efficient near-infrared bioimaging. ACS Appl Mater Interfaces. 2017; 9: 18540–8.
69. Liu J, Chen G, Hao S, Yang C. Sub-6 nm monodisperse hexagonal core/shell $NaGdF_4$nanocrystals with enhanced upconversion photoluminescence. Nanoscale. 2017; 9: 91–8.
70. Zheng X, Shikha S, Zhang Y. Elimination of concentration dependent luminescence quenching in surface protected upconversion nanoparticles. Nanoscale. 2018; 10: 16447–54.
71. Huang K, Jayakumar MKG, Zhang Y. Lutetium doping for making big core and core-shell upconversion nanoparticles. J Mater Chem C. 2015; 3: 10267–72.
72. Liu D, Xu X, Du Y, Qin X, Zhang Y, Ma C, et al. Three-dimensional controlled growth of monodisperse sub-50 nm heterogeneous nanocrystals. Nat Commun. 2016; 7: 10254.
73. Zhang Y, Zhang L, Deng R, Tian J, Zong Y, Jin D, et al. Multicolor barcoding in a single upconversion crystal. J Am Chem Soc. 2014; 136: 4893–6.
74. Johnson NJJ, Korinek A, Dong C, van Veggel FCJM. Self-focusing by Ostwald ripening: A strategy for layer-by-layer epitaxial growth on upconverting nanocrystals. J Am Chem Soc. 2012; 134: 11068–71.
75. Dühnen S, Haase M. Study on the intermixing of core and shell in $NaEuF_4$/$NaGdF_4$ core/shell nanocrystals. Chem Mater. 2015; 27: 8375–86.
76. Dong C, van Veggel FCJM. Cation exchange in lanthanide fluoride nanoparticles. ACS Nano. 2009; 3: 123–30.
77. Han S, Qin X, An Z, Zhu Y, Liang L, Han Y, et al. Multicolour synthesis in lanthanide-doped nanocrystals through cation exchange in water. Nat Commun. 2016; 7: 13059.
78. Hao S, Chen G, Yang C, Shao W, Wei W, Liu Y, et al. Nd^{3+}-Sensitized multicolor upconversion luminescence from a sandwiched core/shell/shell nanostructure. Nanoscale. 2017; 9: 10633–8.
79. Wang F, Liu X. Upconversion multicolor fine-tuning: Visible to near-infrared emission from lanthanide-doped $NaYF_4$ nanoparticles. J Am Chem Soc. 2008; 130: 5642–3.
80. Zhou B, Tao L, Tsang YH, Jin W. Core-shell nanoarchitecture: A strategy to significantly enhance white-light upconversion of lanthanide-doped nanoparticles. J Mater Chem C. 2013; 1: 4313.
81. Mahalingam V, Mangiarini F, Vetrone F, Venkatramu V, Bettinelli M, Speghini A, et al. Bright white upconversion emission from Tm^{3+}/Yb^{3+}/Er^{3+}-doped $Lu_3Ga_5O_{12}$ nanocrystals. J Phys Chem C. 2008; 112: 17745–9.
82. Wang HQ, Nann T. Monodisperse upconverting nanocrystals by microwave-assisted synthesis. ACS Nano. 2009; 3: 3804–8.
83. Capobianco JA, Vetrone F, D'Alesio T, Tessari G, Speghini A, Bettinelli M. Optical spectroscopy of nanocrystalline cubic Y_2O_3:Er^{3+} obtained by combustion synthesis. Phys Chem Chem Phys. 2000; 2: 3203–7.
84. Wang X, Kong X, Yu Y, Sun Y, Zhang H. Effect of annealing on upconversion luminescence of ZnO:Er^{3+} nanocrystals and high thermal sensitivity. J Phys Chem C. 2007; 111: 15119–24.
85. Dong B, Cao B, He Y, Liu Z, Li Z, Feng Z. Temperature sensing and *in vivo* imaging by molybdenum sensitized visible upconversion luminescence of rare-earth oxides. Adv Mater. 2012; 24: 1987–93.
86. Stouwdam JW, van Veggel FCJM. Near-infrared emission of redispersible Er^{3+}, Nd^{3+}, and Ho^{3+} doped LaF_3 nanoparticles. Nano Lett. 2002; 2: 733–7.
87. Zhai X, Liu S, Liu X, Wang F, Zhang D, Qin G, et al. Sub-10 nm $BaYF_5$:Yb^{3+}, Er^{3+} core-shell nanoparticles with intense. 1.53 μm fluorescence for polymer-based waveguide amplifiers. J Mater Chem C. 2013; 1: 1525.
88. Wang J, Wang F, Wang C, Liu Z, Liu X. Single-band upconversion emission in lanthanide-doped $KMnF_3$ nanocrystals. Angew Chem Int Ed. 2011; 50: 10369–72.
89. Chen G, Qiu H, Prasad PN, Chen X. Upconversion nanoparticles: Design nanochemistry and applications in theranostics. Chem Rev. 2014; 114: 5161–214.
90. Krämer KW, Biner D, Frei G, Güdel HU, Hehlen MP, Lüthi SR. Hexagonal sodium yttrium fluoride based green and blue emitting upconversion phosphors. Chem Mater. 2004; 16: 1244–51.
91. Patra A, Friend CS, Kapoor R, Prasad PN. Effect of crystal nature on upconversion luminescence in Er^{3+}: ZrO_2 nanocrystals. Appl Phys Lett. 2003; 83: 284–6.
92. Bai Y, Wang Y, Yang K, Zhang X, Song Y, Wang CH. Enhanced upconverted photoluminescence in Er^{3+} and Yb^{3+} codoped ZnO nanocrystals with and without Li^+ ions. Opt Commun. 2008; 281: 5448–52.
93. Bai Y, Yang K, Wang Y, Zhang X, Song Y. Enhancement of the upconversion photoluminescence intensity in Li^+ and Er^{3+} codoped Y_2O_3 nanocrystals. Opt Commun. 2008; 281: 2930–2.
94. Chen GY, Liu HC, Somesfalean G, Sheng YQ, Liang HJ, Zhang ZG, et al. Enhancement of the upconversion radiation in Y_2O_3:Er^{3+} nanocrystals by co-doping with Li^+ ions. Appl Phys Lett. 2008; 92: 113114.
95. Yang D, Li C, Li G, Shang M, Kang X, Lin J. Colloidal synthesis and remarkable enhancement of the upconversion luminescence of $BaGdF_5$:Yb^{3+}/Er^{3+} nanoparticles by active-shell modification. J Mater Chem. 2011; 21: 5923.
96. Dou Q, Zhang Y. Tuning of the structure and emission spectra of upconversion nanocrystals by alkali ion doping. Langmuir. 2011; 27: 13236–41.
97. Tang H, Zhou H, Cheng X. Effects of Ca^{2+} doping on upconversion luminescence intensity and crystal field asymmetry of β-NaYF4:Yb^{3+}/Er^{3+} microcrystals. J Lumin. 2020; 221: 117086.
98. Jalani G, Tam V, Vetrone F, Cerruti M. Seeing targeting and delivering with upconverting nanoparticles. J Am Chem Soc. 2018; 140: 10923–31.
99. Jiang L, Xiao S, Yang X, Ding J, Dong K. Enhancement of up-conversion luminescence in Zn_2SiO_4:Yb^{3+},Er^{3+} by co-doping with Li^+ or Bi^{3+}. Appl Phys B. 2012; 107: 477–81.
100. Niu N, He F, Gai S, Li C, Zhang X, Huang S, et al. Rapid microwave reflux process for the synthesis of pure hexagonal $NaYF_4$:Yb^{3+},Ln^{3+},Bi^{3+} (Ln^{3+} = Er^{3+}, Tm^{3+}, Ho^{3+}) and its enhanced UC luminescence. J Mater Chem. 2012; 22: 21613.
101. Ramasamy P, Chandra P, Rhee SW, Kim J. Enhanced upconversion luminescence in $NaGdF_4$:Yb,Er nanocrystals by Fe^{3+} doping and their application in bioimaging. Nanoscale. 2013; 5:8711.
102. Li G, Jiang S, Liu A, Ye L, Ke J, Liu C, et al. Proof of crystal-field-perturbation-enhanced luminescence of lanthanide-doped nanocrystals through interstitial H^+ doping. Nat Commun. 2023; 14: 5870.
103. Garfield DJ, Borys NJ, Hamed SM, Torquato NA, Tajon CA, Tian B, et al.

Enrichment of molecular antenna triplets amplifies upconverting nanoparticle emission. Nat Photon. 2018; 12: 402–7.
104. Chen G, Ohulchanskyy TY, Kumar R, Ågren H, Prasad PN. Ultrasmall monodisperse $NaYF_4$:Yb^{3+}/Tm^{3+} nanocrystals with enhanced near-infrared to near-infrared upconversion photoluminescence. ACS Nano. 2010; 4: 3163–8.
105. Wang J, Deng R, MacDonald MA, Chen B, Yuan J, Wang F, et al. Enhancing multiphoton upconversion through energy clustering at sublattice level. Nat Mater. 2013; 13: 157–62.
106. Zhao J, Jin D, Schartner EP, Lu Y, Liu Y, Zvyagin AV, et al. Single-nanocrystal sensitivity achieved by enhanced upconversion luminescence. Nat Nanotech. 2013; 8: 729–34.
107. Wang F, Wen S, He H, Wang B, Zhou Z, Shimoni O, et al. Microscopic inspection and tracking of single upconversion nanoparticles in living cells. Light Sci Appl. 2018; 7: 18007.
108. Gargas DJ, Chan EM, Ostrowski AD, Aloni S, Altoe MVP, Barnard ES, et al. Engineering bright sub-10-nm upconverting nanocrystals for single-molecule imaging. Nat Nanotechnol. 2014; 9: 300–5.
109. Wei W, Chen G, Baev A, He GS, Shao W, Damasco J, et al. Alleviating luminescence concentration quenching in upconversion nanoparticles through organic dye sensitization. J Am Chem Soc. 2016; 138: 15130–3.
110. Johnson NJJ, He S, Diao S, Chan EM, Dai H, Almutairi A. Direct evidence for coupled surface and concentration quenching dynamics in lanthanide-doped nanocrystals. J Am Chem Soc. 2017; 139: 3275–82.
111. Zeng JH, Xie T, Li ZH, Li Y. Monodispersed nanocrystalline fluoroperovskite up-conversion phosphors. Cryst Growth Des. 2007; 7: 2774–7.
112. Xie MY, Peng XN, Fu XF, Zhang JJ, Li GL, Yu XF. Synthesis of Yb^{3+}/Er^{3+} Co-doped MnF_2 nanocrystals with bright red up-converted fluorescence. Scr Mater. 2009; 60: 190–3.
113. Zhang Y, Lin JD, Vijayaragavan V, Bhakoo KK, Tan TTY. Tuning sub-10 nm single-phase $NaMnF_3$ nanocrystals as ultrasensitive hosts for pure intense fluorescence and excellent T1 magnetic resonance imaging. Chem Commun. 2012; 48: 10322.
114. Tian G, Gu Z, Zhou L, Yin W, Liu X, Yan L, et al. Mn^{2+} dopant-controlled synthesis of $NaYF_4$:Yb,Er upconversion nanoparticles for *in vivo* imaging and drug delivery. Adv Mater. 2012; 24: 1226–31.
115. Wang F, Deng R, Wang J, Wang Q, Han Y, Zhu H, et al. Tuning upconversion through energy migration in core-shell nanoparticles. Nat Mater. 2011; 10: 968–73.
116. Li F, Tu L, Zhang Y, Huang D, Liu X, Zhang X, et al. Size-dependent lanthanide energy transfer amplifies upconversion luminescence quantum yields. Nat Photon. 2024; 18: 440–9.
117. Quintanilla M, Ren F, Ma D, Vetrone F. Light management in upconverting nanoparticles: Ultrasmall core/shell architectures to tune the emission color. ACS Photonics. 2014; 1: 662–9.
118. Zhang Y, Yu Z, Li J, Ao Y, Xue J, Zeng Z, et al. Ultrasmall-superbright neodymium-upconversion nanoparticles via energy migration manipulation and lattice modification: 808 nm-activated drug release. ACS Nano. 2017; 11: 2846–57.
119. Schäfer H, Ptacek P, Zerzouf O, Haase M. Synthesis and optical properties of KYF_4/Yb Er nanocrystals and their surface modification with undoped KYF_4. Adv Funct Mater. 2008; 18: 2913–8.
120. Wang F, Wang J, Liu X. Direct evidence of a surface quenching effect on size-dependent luminescence of upconversion nanoparticles. Angew Chem Int Ed. 2010; 49: 7456–60.
121. Bian W, Lin Y, Wang T, Yu X, Qiu J, Zhou M, et al. Direct identification of surface defects and their influence on the optical characteristics of upconversion nanoparticles. ACS Nano. 2018; 12: 3623–8.
122. Guo H, Li Z, Qian H, Hu Y, Muhammad IN. Seed-mediated synthesis of NaY F_4: Y b Er/$NaGdF_4$nanocrystals with improved upconversion fluorescence and MR relaxivity. Nanotechnology. 2010; 21: 125602.
123. Wang YF, Sun LD, Xiao JW, Feng W, Zhou JC, Shen J, et al. Rare-earth nanoparticles with enhanced upconversion emission and suppressed rare-earth-ion leakage. Chem. 2012; 18: 5558–64.
124. Lü Q, Li A, Guo F, Sun L, Zhao L. Experimental study on the surface modification of Y_2O_3:Tm^{3+}/Yb^{3+}nanoparticles to enhance upconversion fluorescence and weaken aggregation. Nanotechnology. 2008; 19: 145701.
125. Li Z, Guo H, Qian H, Hu Y. Facile microemulsion route to coat carbonized glucose on upconversion nanocrystals as high luminescence and biocompatible cell-imaging probes. Nanotechnology. 2010; 21: 315105.
126. Zhang C, Lee JY. Prevalence of anisotropic shell growth in rare earth core-shell upconversion nanocrystals. ACS Nano. 2013; 7: 4393–402.
127. Li X, Shen D, Yang J, Yao C, Che R, Zhang F, et al. Successive layer-by-layer strategy for multi-shell epitaxial growth: Shell thickness and doping position dependence in upconverting optical properties. Chem Mater. 2012; 25: 106–12.
128. Liang L, Teh DBL, Dinh ND, Chen W, Chen Q, Wu Y, et al. Upconversion amplification through dielectric superlensing modulation. Nat Commun. 2019; 10: 1391.
129. Su Q, Han S, Xie X, Zhu H, Chen H, Chen CK, et al. The effect of surface coating on energy migration-mediated upconversion. J Am Chem Soc. 2012; 134: 20849–57.
130. Zhang F, Che R, Li X, Yao C, Yang J, Shen D, et al. Direct imaging the upconversion nanocrystal core/shell structure at the subnanometer level: Shell thickness dependence in upconverting optical properties. Nano Lett. 2012; 12: 2852–8.
131. Vetrone F, Naccache R, Mahalingam V, Morgan CG, Capobianco JA. The active-core/active-shell approach: A strategy to enhance the upconversion luminescence in lanthanide-doped nanoparticles. Adv Funct Mater. 2009; 19: 2924–9.
132. Wang X, Valiev RR, Ohulchanskyy TY, Ågren H, Yang C, Chen G. Dye-sensitized lanthanide-doped upconversion nanoparticles. Chem Soc Rev. 2017; 46: 4150–67.
133. Geddes CD. Metal-enhanced fluorescence. Phys Chem Chem Phys. 2013; 15: 19537.
134. Deng W, Xie F, Baltar HTMCM, Goldys EM. Metal-enhanced fluorescence in the life sciences: Here now and beyond. Phys Chem Chem Phys. 2013; 15: 15695.
135. Kassab LRP, de Araújo CB, Kobayashi RA, de Almeida Pinto R, da Silva DM. Influence of silver nanoparticles in the luminescence efficiency of Pr^{3+}-doped tellurite glasses. J Appl Phys. 2007; 102: 103515.
136. Feng W, Sun LD, Yan CH. Ag nanowires enhanced upconversion emission of $NaYF_4$:Yb,Er nanocrystals via a direct assembly method. Chem Commun. 2009; 4393.
137. Schietinger S, Aichele T, Wang HQ, Nann T, Benson O. Plasmon-enhanced upconversion in single $NaYF_4$:Yb^{3+}/Er^{3+} codoped nanocrystals. Nano Lett. 2010; 10: 134–8.
138. Zhang H, Xu D, Huang Y, Duan X. Highly spectral dependent enhancement of upconversion emission with sputtered gold island films. Chem Commun. 2011; 47: 979–81.
139. Paudel HP, Zhong L, Bayat K, Baroughi MF, Smith S, Lin C, et al. Enhancement of near-infrared-to-visible upconversion luminescence using engineered plasmonic gold surfaces. J Phys Chem C. 2011; 115: 19028–36.
140. Saboktakin M, Ye X, Oh SJ, Hong SH, Fafarman AT, Chettiar UK, et al. Metal-enhanced upconversion luminescence tunable through metal nanoparticle–nanophosphor separation. ACS Nano. 2012; 6: 8758–66.
141. Zhang W, Ding F, Chou SY. Large enhancement of upconversion luminescence of $NaYF_4$:Yb^{3+}/Er^{3+} nanocrystal by 3D plasmonic nano-antennas. Adv Mater. 2012; 24: 1200220.
142. Sun QC, Mundoor H, Ribot JC, Singh V, Smalyukh II, Nagpal P. Plasmon-enhanced energy transfer for improved upconversion of infrared radiation in doped-lanthanide nanocrystals. Nano Lett. 2014; 14: 101–6.
143. Zhang F, Braun GB, Shi Y, Zhang Y, Sun X, Reich NO, et al. Fabrication of Ag@SiO_2@Y_2O_3: Er nanostructures for bioimaging: Tuning of the upconversion fluorescence with silver nanoparticles. J Am Chem Soc. 2010; 132: 2850–1.
144. Ge W, Zhang XR, Liu M, Lei ZW, Knize RJ, Lu Y. Distance dependence of gold-enhanced upconversion luminescence in Au/SiO_2/Y_2O_3:Yb^{3+},Er^{3+} nanoparticles. Theranostics. 2013; 3: 282–8.
145. Bao G, Wen S, Lin G, Yuan J, Lin J, Wong KL, et al. Learning from lanthanide complexes: The development of dye-lanthanide nanoparticles and their biomedical applications. Coord Chem Rev. 2021; 429: 213642.
146. Wen S, Zhou J, Schuck PJ, Suh YD, Schmidt TW, Jin D. Future and challenges for hybrid upconversion nanosystems. Nat Photon. 2019; 13: 828–38.
147. Zou W, Visser C, Maduro JA, Pshenichnikov MS, Hummelen JC. Broadband dye-sensitized upconversion of near-infrared light. Nat Photon. 2012; 6: 560–4.
148. Chen G, Damasco J, Qiu H, Shao W, Ohulchanskyy TY, Valiev RR, et al. Energy-cascaded upconversion in an organic dye-sensitized core/shell fluoride nanocrystal. Nano Lett. 2015; 15: 7400–7.
149. Zhang P, Ke J, Tu D, Li J, Pei Y, Wang L. Enhancing dye-triplet-sensitized upconversion emission through the heavy-atom effect in $CsLu_2F_7$:Yb/Er nanoprobes. Angew Chem Int Ed. 2021; 61: 202112125.
150. Zhao F, Hu J, Guan D, Liu J, Zhang X, Ling H, et al. Boosting dye-sensitized luminescence by enhanced short-range triplet energy transfer. Adv Mater. 2023; 35: 2304907.
151. Liu Y, Li Y, Koo S, Sun Y, Liu Y, Liu X, et al. Versatile types of inorganic/organic NIR-IIa/IIb fluorophores: From strategic design toward molecular imaging and theranostics. Chem Rev. 2021; 122: 209–68.
152. Tan MC, Kumar GA, Riman RE, Brik MG, Brown E, Hommerich U. Synthesis and optical properties of infrared-emitting YF_3:Nd nanoparticles. J Appl Phys. 2009; 106: 063118.
153. Fischer S, Mehlenbacher RD, Lay A, Siefe C, Alivisatos AP, Dionne JA. Small alkaline-earth-based core/shell nanoparticles for efficient upconversion. Nano Lett. 2019; 19: 3878–85.
154. Zhong Y, Ma Z, Wang F, Wang X, Yang Y, Liu Y, et al. *In vivo* molecular imaging for immunotherapy using ultra-bright near-infrared-IIb rare-earth nanoparticles. Nat Biotechnol. 2019; 37: 1322–31.
155. Zhong Y, Ma Z, Zhu S, Yue J, Zhang M, Antaris AL, et al. Boosting the down-shifting luminescence of rare-earth nanocrystals for biological imaging beyond 1500 nm. Nat Commun. 2017; 8: 737.
156. Yang Y, Chen Y, Pei P, Fan Y, Wang S, Zhang H, et al. Fluorescence-amplified nanocrystals in the second near-infrared window for *in vivo* real-time dynamic

multiplexed imaging. Nat Nanotechnol. 2023; 18: 1195–204.
157. Song X, Li S, Guo H, You W, Shang X, Li R, et al. Graphene-oxide-modified lanthanide nanoprobes for tumor-targeted visible/NIR-II luminescence imaging. Angew Chem Int Ed. 2019; 58: 18981–6.
158. Zhu H, Ren F, Wang T, Jiang Z, Sun Q, Li Z. Targeted immunoimaging of tumor-associated macrophages in orthotopic glioblastoma by the NIR-IIb nanoprobes. Small. 2022; 18: 2202201.
159. Li H, Wang X, Li X, Zeng S, Chen G. Clearable shortwave-infrared-emitting $NaErF_4$ nanoparticles for noninvasive dynamic vascular imaging. Chem Mater. 2020; 32: 3365–75.
160. Mi C, Guan M, Zhang X, Yang L, Wu S, Yang Z, et al. High spatial and temporal resolution NIR-IIb gastrointestinal imaging in mice. Nano Lett. 2022; 22: 2793–800.
161. Zheng W, Huang P, Tu D, Ma E, Zhu H, Chen X. Lanthanide-doped upconversion nano-bioprobes: Electronic structures optical properties and biodetection. Chem Soc Rev. 2015; 44: 1379–415.
162. Li Y, Zhang P, Ning H, Zeng J, Hou Y, Jing L, et al. Emitting/sensitizing ions spatially separated lanthanide nanocrystals for visualizing tumors simultaneously through up- and down-conversion near-infrared II luminescence *in vivo*. Small. 2019; 15: 1905344.
163. Zhan Q, Qian J, Liang H, Somesfalean G, Wang D, He S, et al. Using 915 nm laser excited $Tm^{3+}/Er^{3+}/Ho^{3+}$-doped $NaYbF_4$ upconversion nanoparticles for *in vitro* and deeper *in vivo* bioimaging without overheating irradiation. ACS Nano. 2011; 5: 3744–57.
164. Wang YF, Liu GY, Sun LD, Xiao JW, Zhou JC, Yan CH. Nd^{3+}-sensitized upconversion nanophosphors: Efficient *in vivo* bioimaging Bioimaging probes with minimized heating effect. ACS Nano. 2013; 7: 7200–6.
165. Chen G, Ohulchanskyy TY, Liu S, Law WC, Wu F, Swihart MT, et al. Core/shell $NaGdF_4$:Nd^{3+}/$NaGdF_4$ nanocrystals with efficient near-infrared to near-infrared downconversion photoluminescence for bioimaging applications. ACS Nano. 2012; 6: 2969–77.
166. Jiang Z, He L, Yang Z, Qiu H, Chen X, Yu X, et al. Ultra-wideband-responsive photon conversion through co-sensitization in lanthanide nanocrystals. Nat Commun. 2023; 14: 827.
167. Ming J, Chen Y, Miao H, Fan Y, Wang S, Chen Z, et al. High-brightness transition metal-sensitized lanthanide near-infrared luminescent nanoparticles. Nat Photon. 2024; 18: 1254–62.
168. Taguchi A, Takahei K. Trap level characteristics of rare-earth luminescence centers in III–V semiconductors. J Appl Phys. 1996; 79: 4330–4.
169. Klik MAJ, Gregorkiewicz T, Bradley IV, Wells JPR. Optically induced deexcitation of rare-earth ions in a semiconductor matrix. Phys Rev Lett. 2002; 89: 227401.
170. Zhong Y, Dai H. A mini-review on rare-earth down-conversion nanoparticles for NIR-II imaging of biological systems. Nano Res. 2020; 13: 1281–94.
171. Chengelis DA, Yingling AM, Badger PD, Shade CM, Petoud S. Incorporating lanthanide cations with cadmium selenide nanocrystals: A strategy to sensitize and protect Tb(III). J Am Chem Soc. 2005; 127: 16752–3.
172. Martín-Rodríguez R, Geitenbeek R, Meijerink A. Incorporation and luminescence of Yb^{3+} in CdSe nanocrystals. J Am Chem Soc. 2013; 135: 13668–71.
173. Pan G, Bai X, Yang D, Chen X, Jing P, Qu S, et al. Doping lanthanide into perovskite nanocrystals: Highly improved and expanded optical properties. Nano Lett. 2017; 17: 8005–11.
174. Zhang W, Chen T, Su L, Ge X, Chen X, Song J, et al. Quantum dot-based sensitization system for boosted photon absorption and enhanced second near-infrared luminescence of lanthanide-doped nanoparticle. Anal Chem. 2020; 92: 6094–102.
175. Swabeck JK, Fischer S, Bronstein ND, Alivisatos AP. Broadband sensitization of lanthanide emission with indium phosphide quantum dots for visible to near-infrared downshifting. J Am Chem Soc. 2018; 140: 9120–6.
176. Shao W, Chen G, Kuzmin A, Kutscher HL, Pliss A, Ohulchanskyy TY, et al. Tunable narrow band emissions from dye-sensitized core/shell/shell nanocrystals in the second near-infrared biological window. J Am Chem Soc. 2016; 138: 16192–5.
177. Wang D, Wang D, Kuzmin A, Pliss A, Shao W, Xia J, et al. ICG-sensitized $NaYF_4$: Er nanostructure for theranostics. Adv Opt Mater. 2018; 6: 1701142.
178. Liu Z, Ren F, Zhang H, Yuan Q, Jiang Z, Liu H, et al. Boosting often overlooked long wavelength emissions of rare-earth nanoparticles for NIR-II fluorescence imaging of orthotopic glioblastoma. Biomaterials. 2019; 219: 119364.
179. Liu Z, Yun B, Han Y, Jiang Z, Zhu H, Ren F, et al. Dye-sensitized rare earth nanoparticles with up/down conversion luminescence for on-demand gas therapy of glioblastoma guided by NIR-II fluorescence imaging. Adv Healthc Mater. 2022; 11: 2102042.
180. Liang T, Guo Z, He Y, Wang Y, Li C, Li Z, et al. Cyanine-doped lanthanide metal–organic frameworks for near-infrared II bioimaging. Adv Sci. 2022; 9: 2104561.
181. Wang Q, Liang T, Wu J, Li Z, Liu Z. Dye-sensitized rare earth-doped nanoparticles with boosted NIR-IIb emission for dynamic imaging of vascular network-related disorders. ACS Appl Mater Interfaces. 2021; 13: 29303–12.
182. Wang T, Wang S, Liu Z, He Z, Yu P, Zhao M, et al. A hybrid erbium(III)–bacteriochlorin near-infrared probe for multiplexed biomedical imaging. Nat Mater. 2021; 20: 1571–8.
183. Zhao F, Ling H, Zhang W, Zhang Y, Liu Q. Dye-to-Er^{3+} direct energy transfer for enhancing up- and down-conversion luminescence in sub-10 nm $NaErF_4$. Nano Lett. 2024; 24: 14838–46.
184. Wu B, Zhang L, Yan K, Mei M, Wu W, He Z, et al. Electronic-symmetry-tuned emission beyond. 1500 nm in erbium(III)-phthalocyanine complexes for high-resolution *in vivo* biosensing. J Am Chem Soc. 2025; 147: 44185–90.
185. Zheng B, Fan J, Chen B, Qin X, Wang J, Wang F, et al. Rare-earth doping in nanostructured inorganic materials. Chem Rev. 2022; 122: 5519–603.
186. Zhu X, Zhang H, Zhang F. Expanding NIR-II lanthanide toolboxes for improved biomedical imaging and detection. Acc Mater Res. 2023; 4: 536–47.
187. Schmidt EL, Ou Z, Ximendes E, Cui H, Keck CHC, Jaque D, et al. Near-infrared II fluorescence imaging. Nat Rev Meth Primers. 2024; 4: 23.
188. Yang Y, Jiang Q, Zhang F. Nanocrystals for deep-tissue *in vivo* luminescence imaging in the near-infrared region. Chem Rev. 2024; 124: 554–628.
189. Wang F, Zhong Y, Bruns O, Liang Y, Dai H. *In vivo* NIR-II fluorescence imaging for biology and medicine. Nat Photon. 2024; 18: 535–47.
190. Zhang H, Fan Y, Pei P, Sun C, Lu L, Zhang F. Tm^{3+}-sensitized NIR-II fluorescent nanocrystals for *in vivo* information storage and decoding. Angew Chem Int Ed Engl. 2019; 58: 10153–7.
191. Chang Y, Chen H, Xie X, Wan Y, Li Q, Wu F, et al. Bright Tm^{3+}-based downshifting luminescence nanoprobe operating around. 1800 nm for NIR-IIb and c bioimaging. Nat Commun. 2023; 14: 1079.
192. Yu Z, Ran Q, Li M, Wen S, Gao H, Xian Y, et al. Downshifting luminescence rare-earth nanoparticles for high-resolution *in vivo* imaging at NIR IIb/c window. Nano Lett. 2025; 25: 15996–6005.
193. Wang X, Wu W, Yun B, Huang L, Chen ZH, Ming J, et al. An emerging toolkit of Ho^{3+} sensitized lanthanide nanocrystals with NIR-II excitation and emission for *in vivo* bioimaging. J Am Chem Soc. 2025; 147: 2182–92.
194. Sun Y, Kong M, Ke J, Gu Y, Li F, Feng W. Rare earth luminescent nanothermometers for biological thermal sensing. Coord Chem Rev. 2025; 523: 216222.
195. del Rosal B, Ximendes E, Rocha U, Jaque D. *In vivo* luminescence nanothermometry: From materials to applications. Adv Opt Mater. 2017; 5: 1600508.
196. Liu M, Liang J, Vetrone F. Toward accurate photoluminescence nanothermometry using rare-earth doped nanoparticles for biomedical applications. Acc Chem Res. 2024; 57: 2653–64.
197. Brites CDS, Balabhadra S, Carlos LD. Lanthanide-based thermometers: At the cutting-edge of luminescence thermometry. Adv Opt Mater. 2019; 7: 1801239.
198. Piñol R, Zeler J, Brites CDS, Gu Y, Téllez P, Carneiro Neto AN, et al. Real-time intracellular temperature imaging using lanthanide-bearing polymeric micelles. Nano Lett. 2020; 20: 6466–72.
199. Zhou J, del Rosal B, Jaque D, Uchiyama S, Jin D. Advances and challenges for fluorescence nanothermometry. Nat Methods. 2020; 17: 967–80.
200. Jaque D, Vetrone F. Luminescence nanothermometry. Nanoscale. 2012; 4: 4301.
201. Đačanin Far L, Dramićanin MD. Luminescence thermometry with nanoparticles: A review. Nanomaterials. 2023; 13: 2904.
202. Vetrone F, Naccache R, Zamarrón A, Juarranz de la Fuente A, Sanz-Rodríguez F, Martinez Maestro L, et al. Temperature sensing using fluorescent nanothermometers. ACS Nano. 2010; 4: 3254–8.
203. Zhu X, Feng W, Chang J, Tan YW, Li J, Chen M, et al. Temperature-feedback upconversion nanocomposite for accurate photothermal therapy at facile temperature. Nat Commun. 2016; 7: 10437.
204. Xu M, Chen D, Huang P, Wan Z, Zhou Y, Ji Z. A dual-functional upconversion core@shell nanostructure for white-light-emission and temperature sensing. J Mater Chem C. 2016; 4: 6516–24.
205. Ximendes EC, Rocha U, Sales TO, Fernández N, Sanz-Rodríguez F, Martín IR, et al. *In vivo* subcutaneous thermal video recording by supersensitive infrared nanothermometers. Adv Funct Mater. 2017; 27: 1702249.
206. Zhang F, Tang BZ. Near-infrared luminescent probes for bioimaging and biosensing. Chem Sci. 2021; 12: 3377–8.
207. Jurga N, Runowski M, Grzyb T. Lanthanide-based nanothermometers for bioapplications: Excitation and temperature sensing in optical transparency windows. J Mater Chem C. 2024; 12: 12218–48.
208. Qiu X, Zhou Q, Zhu X, Wu Z, Feng W, Li F. Ratiometric upconversion nanothermometry with dual emission at the same wavelength decoded via a time-resolved technique. Nat Commun. 2020; 11: 4.
209. Jia M, Fu Z, Liu G, Sun Z, Li P, Zhang A, et al. NIR-II/III luminescence ratiometric nanothermometry with phonon-tuned sensitivity. Adv Opt Mater. 2020; 8: 1901173.
210. Hazra C, Skripka A, Ribeiro SJL, Vetrone F. Erbium single-band nanothermometry in the third biological imaging window: Potential and limitations. Adv Opt Mater. 2020; 8: 2001178.
211. Suo H, Zhao X, Zhang Z, Wang Y, Sun J, Jin M, et al. Rational design of

ratiometric luminescence thermometry based on thermally coupled levels for bioapplications. Laser Photonics Rev. 2021; 15: 2000319.
212. Cheng Y, Gao Y, Lin H, Huang F, Wang Y. Strategy design for ratiometric luminescence thermometry: circumventing the limitation of thermally coupled levels. J Mater Chem C. 2018; 6: 7462–78.
213. Li D, Jia M, Jia T, Chen G. Ultrasensitive NIR-II ratiometric nanothermometers for 3D *in vivo* thermal imaging. Adv Mater. 2024; 36: e2309452.
214. Li H, Tan M, Wang X, Li F, Zhang Y, Zhao L, et al. Temporal multiplexed *in vivo* upconversion imaging. J Am Chem Soc. 2020; 142: 2023–30.
215. Tan M, Li F, Cao N, Li H, Wang X, Zhang C, et al. Accurate *in vivo* nanothermometry through NIR-II lanthanide luminescence lifetime. Small. 2020; 16: e2004118.
216. Hauser M, Wojcik M, Kim D, Mahmoudi M, Li W, Xu K. Correlative super-resolution microscopy: New dimensions and new opportunities. Chem Rev. 2017; 117: 7428–56.
217. Jin D, Xi P, Wang B, Zhang L, Enderlein J, van Oijen AM. Nanoparticles for super-resolution microscopy and single-molecule tracking. Nat Methods. 2018; 15: 415–23.
218. Liu Y, Lu Y, Yang X, Zheng X, Wen S, Wang F, et al. Amplified stimulated emission in upconversion nanoparticles for super-resolution nanoscopy. Nature. 2017; 543: 229–33.
219. Nam SH, Bae YM, Park YI, Kim JH, Kim HM, Choi JS, et al. Long-term real-time tracking of lanthanide ion doped upconverting nanoparticles in living cells. Angew Chem Int Ed. 2011; 50: 6093–7.
220. Jo HL, Song YH, Park J, Jo EJ, Goh Y, Shin K, et al. Fast and background-free three-dimensional (3D) live-cell imaging with lanthanide-doped upconverting nanoparticles. Nanoscale. 2015; 7: 19397–402.
221. Liang L, Feng Z, Zhang Q, Cong TD, Wang Y, Qin X, et al. Continuous-wave near-infrared stimulated-emission depletion microscopy using downshifting lanthanide nanoparticles. Nat Nanotechnol. 2021; 16: 975–80.
222. Guo X, Pu R, Zhu Z, Qiao S, Liang Y, Huang B, et al. Achieving low-power single-wavelength-pair nanoscopy with NIR-II continuous-wave laser for multi-chromatic probes. Nat Commun. 2022; 13: 2843.
223. Pu R, Zhan Q, Peng X, Liu S, Guo X, Liang L, et al. Super-resolution microscopy enabled by high-efficiency surface-migration emission depletion. Nat Commun. 2022; 13: 6636.
224. Zhan Q, Liu H, Wang B, Wu Q, Pu R, Zhou C, et al. Achieving high-efficiency emission depletion nanoscopy by employing cross relaxation in upconversion nanoparticles. Nat Commun. 2017; 8: 1058.
225. Lamon S, Yu H, Zhang Q, Gu M. Lanthanide ion-doped upconversion nanoparticles for low-energy super-resolution applications. Light Sci Appl. 2024; 13: 252.
226. Miller CJ, Davidson LA. The interplay between cell signalling and mechanics in developmental processes. Nat Rev Genet. 2013; 14: 733–44.
227. Chaudhuri PK, Low BC, Lim CT. Mechanobiology of tumor growth. Chem Rev. 2018; 118: 6499–515.
228. Villeneuve C, McCreery KP, Wickstrom SA. Measuring and manipulating mechanical forces during development. Nat Cell Biol. 2025; 27: 575–90.
229. Bao G, Suresh S. Cell and molecular mechanics of biological materials. Nat Mater. 2003; 2: 715–25.
230. Arlett JL, Myers EB, Roukes ML. Comparative advantages of mechanical biosensors. Nat Nanotechnol. 2011; 6: 203–15.
231. Xin H, Li Y, Liu YC, Zhang Y, Xiao YF, Li B. Optical forces: From fundamental to biological applications. Adv Mater. 2020; 32: e2001994.
232. Mehlenbacher RD, Kolbl R, Lay A, Dionne JA. Nanomaterials for *in vivo* imaging of mechanical forces and electrical fields. Nat Rev Mater. 2018; 3: 17080.
233. Zhang H, Peng D, Wang W, Dong L, Pan C. Mechanically induced light emission and infrared-laser-induced upconversion in the Er-doped CaZnOS multifunctional piezoelectric semiconductor for optical pressure and temperature sensing. J Phys Chem C. 2015; 119: 28136–42.
234. Zhang JC, Long YZ, Yan X, Wang X, Wang F. Creating recoverable mechanoluminescence in piezoelectric calcium niobates through Pr^{3+} doping. Chem Mater. 2016; 28: 4052–7.
235. Chen C, Zhuang Y, Tu D, Wang X, Pan C, Xie RJ. Creating visible-to-near-infrared mechanoluminescence in mixed-anion compounds $SrZn_2S_2O$ and SrZnSO. Nano Energy. 2020; 68: 104329.
236. Zhuang Y, Tu D, Chen C, Wang L, Zhang H, Xue H, et al. Force-induced charge carrier storage: A new route for stress recording. Light Sci Appl. 2020; 9: 182.
237. Lay A, Wang DS, Wisser MD, Mehlenbacher RD, Lin Y, Goodman MB, et al. Upconverting nanoparticles as optical sensors of nano- to micro-Newton forces. Nano Lett. 2017; 17: 4172–7.
238. Mei S, Guo Y, Lin X, Dong H, Sun LD, Li K, et al. Experimental and simulation insights into local structure and luminescence evolution in Eu^{3+}-doped nanocrystals under high pressure. J Phys Chem Lett. 2020; 11: 3515–20.
239. Fardian-Melamed N, Skripka A, Ursprung B, Lee C, Darlington TP, Teitelboim A, et al. Infrared nanosensors of piconewton to micronewton forces. Nature. 2025; 637: 70–5.
240. Casar JR, McLellan CA, Shi C, Stiber A, Lay A, Siefe C, et al. Upconverting microgauges reveal intraluminal force dynamics *in vivo*. Nature. 2025; 637: 76–83.
241. Luo Z, Mao D, Li X, Luo J, Gong C, Liu X. Lanthanide-based nanoparticles for cancer phototherapy. Coord Chem Rev. 2024; 508: 215773.
242. Mao D, Hu F, Yi Z, Kenry, Xu S, Yan S, et al. AIEgen-coupled upconversion nanoparticles eradicate solid tumors through dual-mode ROS activation. Sci Adv. 2020; 6: eabb2712.
243. Castano AP, Mroz P, Hamblin MR. Photodynamic therapy and anti-tumour immunity. Nat Rev Cancer. 2006; 6: 535–45.
244. Burgess DJ. Tissue penetration of photodynamic therapy. Nat Rev Cancer. 2012; 12: 737.
245. Ji B, Wei M, Yang B. Recent advances in nanomedicines for photodynamic therapy (PDT)-driven cancer immunotherapy. Theranostics. 2022; 12: 434–58.
246. Li H, Wang X, Ohulchanskyy TY, Chen G. Lanthanide-doped near-infrared nanoparticles for biophotonics. Adv Mater. 2021; 33: e2000678.
247. Meijer MS, Talens VS, Hilbers MF, Kieltyka RE, Brouwer AM, Natile MM, et al. NIR-light-driven generation of reactive oxygen species using Ru(II)-decorated lipid-encapsulated upconverting nanoparticles. Langmuir. 2019; 35: 12079–90.
248. Li C, Ye J, Yang X, Liu S, Zhang Z, Wang J, et al. Fe/Mn bimetal-doped ZIF-8-coated luminescent nanoparticles with up/downconversion dual-mode emission for tumor self-enhanced NIR-II imaging and catalytic therapy. ACS Nano. 2022; 16: 18143–56.
249. Han XB, Li HX, Jiang YQ, Wang H, Li XS, Kou JY, et al. Upconversion nanoparticle-mediated photodynamic therapy induces autophagy and cholesterol efflux of macrophage-derived foam cells via ROS generation. Cell Death Dis. 2017; 8: e2864.
250. Qiu H, Tan M, Ohulchanskyy TY, Lovell JF, Chen G. Recent progress in upconversion photodynamic therapy. Nanomaterials. 2018; 8: 344.
251. Yu Z, Ge Y, Sun Q, Pan W, Wan X, Li N, et al. A pre-protective strategy for precise tumor targeting and efficient photodynamic therapy with a switchable DNA/upconversion nanocomposite. Chem Sci. 2018; 9: 3563–9.
252. Wang C, Tao H, Cheng L, Liu Z. Near-infrared light induced *in vivo* photodynamic therapy of cancer based on upconversion nanoparticles. Biomaterials. 2011; 32: 6145–54.
253. Ai X, Ho CJH, Aw J, Attia ABE, Mu J, Wang Y, et al. *In vivo* covalent cross-linking of photon-converted rare-earth nanostructures for tumour localization and theranostics. Nat Commun. 2016; 7, 10432.
254. Yang Y, Zhang L, Xiao C, Huang Z, Zhao F, Yin J. Highly efficient upconversion photodynamic performance of rare-earth-coupled dual-photosensitizers: Ultrafast experiments and excited-state calculations. Nanophotonics. 2024; 13: 443–55.
255. Yang M, Wang H, Wang Z, Han Z, Gu Y. A Nd^{3+} sensitized upconversion nanosystem with dual photosensitizers for improving photodynamic therapy efficacy. Biomater Sci. 2019; 7: 1686–95.
256. Xia L, Kong X, Liu X, Tu L, Zhang Y, Chang Y, et al. An upconversion nanoparticle–Zinc phthalocyanine based nanophotosensitizer for photodynamic therapy. Biomaterials. 2014; 35: 4146–56.
257. Zhang W, Zhang X, Shen Y, Shi F, Song C, Liu T, et al. Ultra-high FRET efficiency $NaGdF_4$: Tb^{3+}-Rose Bengal biocompatible nanocomposite for X-ray excited photodynamic therapy application. Biomaterials. 2018; 184: 31–40.
258. Yue L, Liu Y, Wang J, Wu Y, Liu J, Zhang Z, et al. Rechargeable afterglow superclusters for NIR-excitable repetitive phototherapy. Nano Lett. 2024; 24: 15406–13.
259. Xu J, Han W, Yang P, Jia T, Dong S, Bi H, et al. Tumor microenvironment-responsive mesoporous MnO_2-coated upconversion nanoplatform for self-enhanced tumor theranostics. Adv Funct Mater. 2018; 28: 1803804.
260. Wang M, Chen Z, Zheng W, Zhu H, Lu S, Ma E, et al. Lanthanide-doped upconversion nanoparticles electrostatically coupled with photosensitizers for near-infrared-triggered photodynamic therapy. Nanoscale. 2014; 6: 8274–82.
261. Li Y, Li Y, Bai Y, Wang R, Lin L, Sun Y. Semiconductor ZnO based photosensitizer core-shell upconversion nanoparticle heterojunction for photodynamic therapy. RSC Adv. 2020; 10: 38416–23.
262. Hou Z, Zhang Y, Deng K, Chen Y, Li X, Deng X, et al. UV-emitting upconversion-based TiO_2 photosensitizing nanoplatform: Near-infrared light mediated *in vivo* photodynamic therapy via mitochondria-involved apoptosis pathway. ACS Nano. 2015; 9: 2584–99.
263. Zuo J, Tu L, Li Q, Feng Y, Que I, Zhang Y, et al. Near infrared light sensitive ultraviolet-blue nanophotoswitch for imaging-guided "off-on" therapy. ACS Nano. 2018; 12: 3217–25.
264. Jia T, Du J, Yang J, Li F, Fang X, Chen G. Near-infrared upconversion photosensitizer enabling photodynamic production and *in situ* dynamic monitoring of hydroxyl radical in live mice. Nano Today. 2023; 51: 101932.
265. Li Z, Qiao X, He G, Sun X, Feng D, Hu L, et al. Core–satellite metal-organic framework@upconversion nanoparticle superstructures via electrostatic self-assembly for efficient photodynamic theranostics. Nano Res. 2020; 13: 3377–86.
266. Liu Q, Wu B, Li M, Huang Y, Li L. Heterostructures made of upconversion

nanoparticles and metal-organic frameworks for biomedical applications. Adv Sci. 2022; 9: e2103911.
267. Lu K, He C, Guo N, Chan C, Ni K, Lan G, et al. Low-dose X-ray radiotherapy-radiodynamic therapy via nanoscale metal-organic frameworks enhances checkpoint blockade immunotherapy. Nat Biomed Eng. 2018; 2: 600–10.
268. Lan G, Ni K, Lin W. Nanoscale metal–organic frameworks for phototherapy of cancer. Coord Chem Rev. 2019; 379, 65–81.
269. Li Y, Di Z, Gao J, Cheng P, Di C, Zhang G, et al. Heterodimers made of upconversion nanoparticles and metal–organic frameworks. J Am Chem Soc. 2017; 139: 13804–10.
270. Yang D, Yang G, Gai S, He F, Li C, Yang P. Multifunctional theranostics for dual-modal photodynamic synergistic therapy via stepwise water splitting. ACS Appl Mater Interfaces. 2017; 9: 6829–38.
271. Liu C, Liu B, Zhao J, Di Z, Chen D, Gu Z, et al. Nd^{3+}-sensitized upconversion metal–organic frameworks for mitochondria-targeted amplified photodynamic therapy. Angew Chem Int Ed. 2020; 59: 2634–8.
272. Rosenblum D, Joshi N, Tao W, Karp JM, Peer D. Progress and challenges towards targeted delivery of cancer therapeutics. Nat Commun. 2018; 9: 1410.
273. Large DE, Soucy JR, Hebert J, Auguste DT. Advances in receptor-mediated tumor-targeted drug delivery. Adv Ther. 2019; 2: 1800091.
274. Liu C, Gao Z, Zeng J, Hou Y, Fang F, Li Y, et al. Magnetic/upconversion fluorescent $NaGdF_4$:Yb,Er nanoparticle-based dual-modal molecular probes for imaging tiny tumors *in vivo*. ACS Nano. 2013; 7: 7227–40.
275. Idris NM, Gnanasammandhan MK, Zhang J, Ho PC, Mahendran R, Zhang Y. *In vivo* photodynamic therapy using upconversion nanoparticles as remote-controlled nanotransducers. Nat Med. 2012; 18: 1580–5.
276. Zhang P, Steelant W, Kumar M, Scholfield M. Versatile photosensitizers for photodynamic therapy at infrared excitation. J Am Chem Soc. 2007; 129: 4526–7.
277. Xu S, Zhu X, Zhang C, Huang W, Zhou Y, Yan D. Oxygen and Pt(II) self-generating conjugate for synergistic photo-chemo therapy of hypoxic tumor. Nat Commun. 2018; 9: 2053.
278. Hu P, Wu T, Fan W, Chen L, Liu Y, Ni D, et al. Near infrared-assisted Fenton reaction for tumor-specific and mitochondrial DNA-targeted photochemotherapy. Biomaterials. 2017; 141: 86–95.
279. Chang Y, Li X, Zhang L, Xia L, Liu X, Li C, et al. Precise photodynamic therapy of cancer via subcellular dynamic tracing of dual-loaded upconversion nanophotosensitizers. Sci Rep. 2017; 7: 45633.
280. Sun M, Xu L, Ma W, Wu X, Kuang H, Wang L, et al. Hierarchical plasmonic nanorods and upconversion core–satellite nanoassemblies for multimodal imaging-guided combination phototherapy. Adv Mater. 2016; 28: 898–904.
281. Wang Y, Li Y, Zhang Z, Wang L, Wang D, Tang BZ. Triple-jump photodynamic theranostics: MnO_2 combined upconversion nanoplatforms involving a type-I photosensitizer with aggregation-induced emission characteristics for potent cancer treatment. Adv Mater. 2021; 33: e2103748.
282. Han S, Samanta A, Xie X, Huang L, Peng J, Park SJ, et al. Gold and hairpin DNA functionalization of upconversion nanocrystals for imaging and *in vivo* drug delivery. Adv Mater. 2017; 29: 1704811.
283. Sedlmeier A, Gorris HH. Surface modification and characterization of photon-upconverting nanoparticles for bioanalytical applications. Chem Soc Rev. 2015; 44: 1526–60.
284. Ansari AA, Parchur AK, Chen G. Surface modified lanthanide upconversion nanoparticles for drug delivery cellular uptake mechanism and current challenges in NIR-driven therapies. Coord Chem Rev. 2022; 457: 214423.
285. Nsubuga A, Morice K, Fayad N, Pini F, Josserand V, Le Guével X, et al. Sub 20 nm upconversion photosensitizers for near-infrared photodynamic theranostics. Adv Funct Mater. 2024; 35: 2410077.
286. Zheng B, Zhong D, Xie T, Zhou J, Li W, Ilyas A, et al. Near-infrared photosensitization via direct triplet energy transfer from lanthanide nanoparticles. Chem. 2021; 7: 1615–25.
287. Zhang X, Chen W, Xie X, Zhang Y, Chao Z, Ma H, et al. Energy pumping by surface collectors on upconversion nanoparticles for extended transfer and efficient self-evaluable photodynamic therapy. CCS Chem. 2022; 4: 1251–62.
288. Yang K, Zhao S, Li B, Wang B, Lan M, Song X. Low temperature photothermal therapy: Advances and perspectives. Coord Chem Rev. 2022; 454: 214330.
289. Li X, Lovell JF, Yoon J, Chen X. Clinical development and potential of photothermal and photodynamic therapies for cancer. Nat Rev Clin Oncol. 2020; 17: 657–74.
290. Deng X, Shao Z, Zhao Y. Solutions to the drawbacks of photothermal and photodynamic cancer therapy. Adv Sci. 2021; 8: 2002504.
291. He S, Song J, Qu J, Cheng Z. Crucial breakthrough of second near-infrared biological window fluorophores: Design and synthesis toward multimodal imaging and theranostics. Chem Soc Rev. 2018; 47: 4258–78.
292. Ge X, Song ZM, Sun L, Yang YF, Shi L, Si R, et al. Lanthanide (Gd^{3+} and Yb^{3+}) functionalized gold nanoparticles for *in vivo* imaging and therapy. Biomaterials. 2016; 108: 35–43.
293. Xiao Q, Zheng X, Bu W, Ge W, Zhang S, Chen F, et al. A core/satellite multifunctional nanotheranostic for *in vivo* imaging and tumor eradication by radiation/photothermal synergistic therapy. J Am Chem Soc. 2013; 135: 13041–8.
294. Overchuk M, Weersink RA, Wilson BC, Zheng G. Photodynamic and photothermal therapies: Synergy opportunities for nanomedicine. ACS Nano. 2023; 17: 7979–8003.
295. Guo L, Yan DD, Yang D, Li Y, Wang X, Zalewski O, et al. Combinatorial photothermal and immuno cancer therapy using chitosan-coated hollow copper sulfide nanoparticles. ACS Nano. 2014; 8: 5670–81.
296. Cheng L, Yang K, Li Y, Chen J, Wang C, Shao M, et al. Facile preparation of multifunctional upconversion nanoprobes for multimodal imaging and dual-targeted photothermal therapy. Angew Chem Int Ed. 2011; 50: 7385–90.
297. Liu B, Li C, Xing B, Yang P, Lin J. Multifunctional UCNPs@PDA-ICG nanocomposites for upconversion imaging and combined photothermal/photodynamic therapy with enhanced antitumor efficacy. J Mater Chem B. 2016; 4: 4884–94.
298. Lv R, Yang P, Hu B, Xu J, Shang W, Tian J. *In situ* growth strategy to integrate up-conversion nanoparticles with ultrasmall CuS for photothermal theranostics. ACS Nano. 2017; 11: 1064–72.
299. Wang C, Xue R, Gulzar A, Kuang Y, Shao H, Gai S, et al. Targeted and imaging-guided chemo-photothermal ablation achieved by combining upconversion nanoparticles and protein-capped gold nanodots. Chem Eng J. 2019; 370: 1239–50.
300. Du K, Lei P, Dong L, Zhang M, Gao X, Yao S, et al. *In situ* decorating of ultrasmall Ag_2Se on upconversion nanoparticles as novel nanotheranostic agent for multimodal imaging-guided cancer photothermal therapy. Appl Mater Today. 2020; 18: 100497.
301. Liu Y, Li Y, Koo S, Sun Y, Liu Y, Liu X, et al. Versatile types of inorganic/organic NIR-IIa/IIb fluorophores: From strategic design toward molecular imaging and theranostics. Chem Rev. 2022; 122: 209–68.
302. Li X, Jiang M, Zeng S, Liu H. Polydopamine coated multifunctional lanthanide theranostic agent for vascular malformation and tumor vessel imaging beyond. 1500 nm and imaging-guided photothermal therapy. Theranostics. 2019; 9: 3866–78.
303. Wang X, Li H, Li F, Han X, Chen G. Prussian blue-coated lanthanide-doped core/shell/shell nanocrystals for NIR-II image-guided photothermal therapy. Nanoscale. 2019; 11: 22079–88.
304. Meng X, Zhang B, Yi Y, Cheng H, Wang B, Liu Y, et al. Accurate and real-time temperature monitoring during MR imaging guided PTT. Nano Lett. 2020; 20: 2522–9.
305. West CL, Doughty ACV, Liu K, Chen WR. Monitoring tissue temperature during photothermal therapy for cancer. J BioX Res. 2019; 2: 159–68.
306. Li L, Zhang X, Zhou J, Zhang L, Xue J, Tao W. Non-invasive thermal therapy for tissue engineering and regenerative medicine. Small. 2022; 18: e2107705.
307. Kong N, Hu Q, Wu Y, Zhu X. Lanthanide luminescent nanocomposite for non-invasive temperature monitoring *in vivo*. Chemistry A European J. 2022; 28: e202104237.
308. Sun X, Sun J, Dong B, Huang G, Zhang L, Zhou W, et al. Noninvasive temperature monitoring for dual-modal tumor therapy based on lanthanide-doped up-conversion nanocomposites. Biomaterials. 2019; 201: 42–52.
309. Liu Y, Zhu X, Wei Z, Feng W, Li L, Ma L, et al. Customized photothermal therapy of subcutaneous orthotopic cancer by multichannel luminescent nanocomposites. Adv Mater. 2021; 33: e2008615.
310. Liu G, Wang Z, Sun W, Lin X, Wang R, Li C, et al. Robust emission in near-infrared II of lanthanide nanoprobes conjugated with Au (LNPs-Au) for temperature sensing and controlled photothermal therapy. Chem Eng J. 2023; 452: 139504.
311. All AH, Zeng X, Teh DBL, Yi Z, Prasad A, Ishizuka T, et al. Expanding the toolbox of upconversion nanoparticles for *in vivo* optogenetics and neuromodulation. Adv Mater. 2019; 31: e1803474.
312. Chen S, Weitemier AZ, Zeng X, He L, Wang X, Tao Y, et al. Near-infrared deep brain stimulation via upconversion nanoparticle–mediated optogenetics. Science. 2018; 359: 679–84.
313. Lin X, Chen X, Zhang W, Sun T, Fang P, Liao Q, et al. Core-shell-shell upconversion nanoparticles with enhanced emission for wireless optogenetic inhibition. Nano Lett. 2018; 18: 948–56.
314. Wu X, Zhang Y, Takle K, Bilsel O, Li Z, Lee H, et al. Dye-sensitized core/active shell upconversion nanoparticles for optogenetics and bioimaging applications. ACS Nano. 2016; 10: 1060–6.
315. Yan J, Wan Y, Ji Z, Li C, Tao C, Tang Y, et al. Motor neuron-specific membrane depolarization of transected peripheral nerves by upconversion nanoparticle-mediated optogenetics. Adv Funct Mater. 2023; 33: 2303992.
316. Chen X, Zhang X, Liu Y, Chen Y, Zhao Y. Upconversion nanoparticle-anchored metal-organic framework nanostructures for remote-controlled cancer optogenetic therapy. J Am Chem Soc. 2024; 146: 34475–90.
317. Gu Z, Yan L, Tian G, Li S, Chai Z, Zhao Y. Recent advances in design and fabrication of upconversion nanoparticles and their safe theranostic applications. Adv Mater. 2013; 25: 3758–79.
318. Kang H, Zhang K, Wong DSH, Han F, Li B, Bian L. Near-infrared light-controlled regulation of intracellular calcium to modulate macrophage polarization. Biomaterials. 2018; 178: 681–96.

319. Chu H, Zhao J, Mi Y, Di Z, Li L. NIR-light-mediated spatially selective triggering of anti-tumor immunity via upconversion nanoparticle-based immunodevices. Nat Commun. 2019; 10: 2839.
320. Yan J, Wang G, Xie L, Tian H, Li J, Li B, et al. Engineering radiosensitizer-based metal-phenolic networks potentiate STING pathway activation for advanced radiotherapy. Adv Mater. 2022; 34: e2105783.
321. Li Y, Li X, Yi J, Cao Y, Qin Z, Zhong Z, et al. Nanoparticle-mediated STING activation for cancer immunotherapy. Adv Healthc Mater. 2023; 12: e2300260.
322. Martin JD, Cabral H, Stylianopoulos T, Jain RK. Improving cancer immunotherapy using nanomedicines: Progress opportunities and challenges. Nat Rev Clin Oncol. 2020; 17: 251–66.
323. Nam J, Son S, Park KS, Zou W, Shea LD, Moon JJ. Cancer nanomedicine for combination cancer immunotherapy. Nat Rev Mater. 2019; 4: 398–414.
324. Hao Y, Chung CK, Yu Z, Huis In 't Veld RV, Ossendorp FA, Ten Dijke P, et al. Combinatorial therapeutic approaches with nanomaterial-based photodynamic cancer therapy. Pharmaceutics. 2022; 14: 120.
325. Ovais M, Mukherjee S, Pramanik A, Das D, Mukherjee A, Raza A, et al. Designing stimuli-responsive upconversion nanoparticles that exploit the tumor microenvironment. Adv Mater. 2020; 32: e2000055.
326. Zhou T, Pliss A, Chen Y, Kuzmin AN, Prasad PN, Qu J. A dual mode nanophotonics concept for *in situ* activation of brain immune cells using a photoswitchable yolk-shell upconversion nanoformulation. Nanomed Nanotechnol Biol Med. 2020; 29: 102279.
327. Chen C, Song M, Du Y, Yu Y, Li C, Han Y, et al. Tumor-associated-macrophage-membrane-coated nanoparticles for improved photodynamic immunotherapy. Nano Lett. 2021; 21: 5522–31.
328. Yoon J, Le XT, Kim J, Lee H, Nguyen NT, Lee WT, et al. Macrophage-reprogramming upconverting nanoparticles for enhanced TAM-mediated antitumor therapy of hypoxic breast cancer. J Control Release. 2023; 360: 482–95.
329. Schaue D, McBride WH. Opportunities and challenges of radiotherapy for treating cancer. Nat Rev Clin Oncol. 2015; 12: 527–40.
330. Hong Z, Chen Z, Chen Q, Yang H. Advancing X-ray luminescence for imaging biosensing and theragnostics. Acc Chem Res. 2023; 56: 37–51.
331. Mowat P, Mignot A, Rima W, Lux F, Tillement O, Roulin C, et al. *In vitro* radiosensitizing effects of ultrasmall gadolinium based particles on tumour cells. J Nanosci Nanotechnol. 2011; 11: 7833–9.
332. Jiang X, Jiang X, Wu D, Xie W, Liu X, Zheng J. A pH-sensitive nanoparticle as reactive oxygen species amplifier to regulate tumor microenvironment and potentiate tumor radiotherapy. Int J Nanomedicine. 2024; 19: 709–25.
333. Kamkaew A, Chen F, Zhan Y, Majewski RL, Cai W. Scintillating nanoparticles as energy mediators for enhanced photodynamic therapy. ACS Nano. 2016; 10: 3918–35.
334. Ou X, Qin X, Huang B, Zan J, Wu Q, Hong Z, et al. High-resolution X-ray luminescence extension imaging. Nature. 2021; 590: 410–5.
335. Pei P, Chen Y, Sun C, Fan Y, Yang Y, Liu X, et al. X-ray-activated persistent luminescence nanomaterials for NIR-II imaging. Nat Nanotechnol. 2021; 16: 1011–8.
336. Zhong X, Wang X, Zhan G, Tang YA, Yao Y, Dong Z, et al. $NaCeF_4$: Gd Tb scintillator as an X-ray responsive photosensitizer for multimodal imaging-guided synchronous radio/radiodynamic therapy. Nano Lett. 2019; 19: 8234–44.
337. Jiang M, Xue Z, Li Y, Liu H, Zeng S, Hao J. A soft X-ray activated lanthanide scintillator for controllable NO release and gas-sensitized cancer therapy. Nanoscale Horiz. 2020; 5: 268–73.
338. Dou Y, Liu Y, Zhao F, Guo Y, Li X, Wu M, et al. Radiation-responsive scintillating nanotheranostics for reduced hypoxic radioresistance under ROS/NO-mediated tumor microenvironment regulation. Theranostics. 2018; 8: 5870–89.
339. Li Y, Jiang M, Deng Z, Zeng S, Hao J. Low dose soft X-ray remotely triggered lanthanide nanovaccine for deep tissue CO gas release and activation of systemic anti-tumor immunoresponse. Adv Sci. 2021; 8: e2004391.
340. Fan W, Bu W, Zhang Z, Shen B, Zhang H, He Q, et al. X-ray radiation-controlled NO-release for on-demand depth-independent hypoxic radiosensitization. Angew Chem Int Ed. 2015; 54: 14026–30.
341. Xue Z, Jiang M, Liu H, Zeng S, Hao J. Low dose soft X-ray-controlled deep-tissue long-lasting NO release of persistent luminescence nanoplatform for gas-sensitized anticancer therapy. Biomaterials. 2020; 263: 120384.
342. Fan W, Yung BC, Chen X. Stimuli-responsive NO release for on-demand gas-sensitized synergistic cancer therapy. Angew Chem Int Ed. 2018; 57: 8383–94.
343. Liu S, Li W, Zhang Y, Zhou J, Du Y, Dong S, et al. Tailoring silica-based nanoscintillators for peroxynitrite-potentiated nitrosative stress in postoperative radiotherapy of colon cancer. Nano Lett. 2022; 22: 6409–17.
344. Yang L, Wang D, Jia H, Yang C, Zhang Y, Li H, et al. Tumor-specific peroxynitrite overproduction disrupts metabolic homeostasis for sensitizing melanoma immunotherapy. Adv Mater. 2023; 35: e2301455.
345. Du Z, Zhang X, Guo Z, Xie J, Dong X, Zhu S, et al. X-ray-controlled generation of peroxynitrite based on nanosized $LiLuF_4$:Ce^{3+} scintillators and their applications for radiosensitization. Adv Mater. 2018; 30: e1804046.
346. Li H, Zeng J, You Q, Zhang M, Shi Y, Yang X, et al. X-ray-activated nanoscintillators integrated with tumor-associated neutrophils polarization for improved radiotherapy in metastatic colorectal cancer. Biomaterials. 2025; 316: 123031.
347. Naldini L. Gene therapy returns to centre stage. Nature. 2015; 526: 351–60.
348. El-Aneed A. An overview of current delivery systems in cancer gene therapy. J Control Release. 2004; 94: 1–14.
349. Zhang Y, Ren K, Zhang X, Chao Z, Yang Y, Ye D, et al. Photo-tearable tape close-wrapped upconversion nanocapsules for near-infrared modulated efficient siRNA delivery and therapy. Biomaterials. 2018; 163: 55–66.
350. Wu Y, Zheng J, Zeng Q, Zhang T, Xing D. Light-responsive charge-reversal nanovector for high-efficiency *in vivo* CRISPR/Cas9 gene editing with controllable location and time. Nano Res. 2020; 13: 2399–406.
351. Pan Y, Yang J, Luan X, Liu X, Li X, Yang J, et al. Near-infrared upconversion-activated CRISPR-Cas9 system: A remote-controlled gene editing platform. Sci Adv. 2019; 5: eaav7199.
352. He Y, Guo S, Wu L, Chen P, Wang L, Liu Y, et al. Near-infrared boosted ROS responsive siRNA delivery and cancer therapy with sequentially peeled upconversion nano-onions. Biomaterials. 2019; 225: 119501.
353. Zeng J, Huang X, Yang Y, Wang J, Shi Y, Li H, et al. Near-infrared optogenetic nanosystem for spatiotemporal control of CRISPR-Cas9 gene editing and synergistic photodynamic therapy. ACS Appl Mater Interfaces. 2025; 17: 701–10.
354. Lee S, Dang H, Moon JI, Kim K, Joung Y, Park S, et al. SERS-based microdevices for use as *in vitro* diagnostic biosensors. Chem Soc Rev. 2024; 53: 5394–427.
355. Ascanio LC, Carroll S, Paniz-Mondolfi A, Ramírez JD. *In vitro* diagnostic methods of Chagas disease in the clinical laboratory: A scoping review. Front Microbiol. 2024; 15: 1393992.
356. Zhou J, Liu Q, Feng W, Sun Y, Li F. Upconversion luminescent materials: Advances and applications. Chem Rev. 2015; 115: 395–465.
357. Ye H, Li Y, Chen X, Du W, Song L, Chen Y, et al. Current developments in emerging lanthanide-doped persistent luminescent scintillators and their applications. Chemistry. 2024; 30: e202303661.
358. Ji T, Xu X, Wang X, Cao N, Han X, Wang M, et al. Background-free chromatographic detection of sepsis biomarker in clinical human serum through near-infrared to near-infrared upconversion immunolabeling. ACS Nano. 2020; 14: 16864–74.
359. Alexander C, Guo Z, Glover PB, Faulkner S, Pikramenou Z. Luminescent lanthanides in biorelated applications: From molecules to nanoparticles and diagnostic probes to therapeutics. Chem Rev. 2025; 125: 2269–370.
360. Noviana E, Ozer T, Carrell CS, Link JS, McMahon C, Jang I, et al. Microfluidic paper-based analytical devices: From design to applications. Chem Rev. 2021; 121: 11835–85.
361. Lisowski P, Zarzycki PK. Microfluidic paper-based analytical devices (μPADs) and micro total analysis systems (μTAS): Development applications and future trends. Chromatographia. 2013; 76: 1201–14.
362. Nishat S, Jafry AT, Martinez AW, Awan FR. Paper-based microfluidics: Simplified fabrication and assay methods. Sens Actuat B Chem. 2021; 336: 129681.
363. Musile G, Grazioli C, Fornasaro S, Dossi N, De Palo EF, Tagliaro F, et al. Application of paper-based microfluidic analytical devices (μPAD) in forensic and clinical toxicology: A review. Biosensors. 2023; 13: 743.
364. Xu S, Dong B, Zhou D, Yin Z, Cui S, Xu W, et al. Paper-based upconversion fluorescence resonance energy transfer biosensor for sensitive detection of multiple cancer biomarkers. Sci Rep. 2016; 6: 23406.
365. Martinez AW, Phillips ST, Butte MJ, Whitesides GM. Patterned paper as a platform for inexpensive low-volume portable bioassays. Angew Chem Int Ed. 2007; 46: 1318–20.
366. He M, Liu Z. Paper-based microfluidic device with upconversion fluorescence assay. Anal Chem. 2013; 85: 11691–4.
367. Wu YM, Cen Y, Huang LJ, Yu RQ, Chu X. Upconversion fluorescence resonance energy transfer biosensor for sensitive detection of human immunodeficiency virus antibodies in human serum. Chem Commun. 2014; 50: 4759–62.
368. Máčala J, Makhneva E, Hlaváček A, Kopecký M, Gorris HH, Skládal P, et al. Upconversion nanoparticle-based dot-blot immunoassay for quantitative biomarker detection. Anal Chem. 2024; 96: 10237–45.
369. Jin B, Li Z, Zhao G, Ji J, Chen J, Yang Y, et al. Upconversion fluorescence-based paper disc for multiplex point-of-care testing in water quality monitoring. Anal Chim Acta. 2022; 1192: 339388.
370. Aydindogan E, Guler Celik E, Timur S. Paper-based analytical methods for smartphone sensing with functional nanoparticles: Bridges from smart surfaces to global health. Anal Chem. 2018; 90: 12325–33.
371. He M, Li Z, Ge Y, Liu Z. Portable upconversion nanoparticles-based paper device for field testing of drug abuse. Anal Chem. 2016; 88: 1530–4.
372. Hosseinifard M, Jurga N, Brandmeier JC, Farka Z, Hlaváček A, Gorris HH, et al. Influence of surface modification and size of lanthanide-doped upconverting nanoparticles on wheat seedlings. Chemosphere. 2024; 347: 140629.
373. Wang M, Abbineni G, Clevenger A, Mao C, Xu S. Upconversion nanoparticles: Synthesis surface modification and biological applications. Nanomed Nanotechnol Biol Med. 2011; 7: 710–29.

374. Das D, Dsouza A, Kaur N, Soni S, Toley BJ. Paper stacks for uniform rehydration of dried reagents in paper microfluidic devices. Sci Rep. 2019; 9: 15755.
375. Boobphahom S, Nguyet Ly M, Soum V, Pyun N, Kwon OS, Rodthongkum N, et al. Recent advances in microfluidic paper-based analytical devices toward high-throughput screening. Molecules. 2020; 25: 2970.
376. Andresen E, Islam F, Prinz C, Gehrmann P, Kai L, Roik J, et al. Assessing the reproducibility and up-scaling of the synthesis of Er,Yb-doped $NaYF_4$-based upconverting nanoparticles and control of size morphology and optical properties. Sci Rep. 2023; 13: 2288.
377. Javaid M, Haleem A, Singh RP, Suman R. Sustaining the healthcare systems through the conceptual of biomedical engineering: A study with recent and future potentials. Biomed Technol. 2023; 1: 39–47.
378. Xiao J, Liu Y, Su L, Zhao D, Zhao L, Zhang X. Microfluidic chip-based wearable colorimetric sensor for simple and facile detection of sweat glucose. Anal Chem. 2019; 91: 14803–7.
379. Chandnani K, Rajput N, Jadav T, Pillai M, Dhakne P, Tekade RK, et al. Technological advancement and current standing of microfluidic chip based devices for targeted analysis of biomarkers. Microchem J. 2023; 195: 109532.
380. Wu J, Wei W, Zareef M, Li S, Ouyang Q, Chen Q. Simple design of upconversion nanoparticles-based aptasensor integrated microfluidic chip for ultrasensitive detection of bisphenol A in aquatic products. Sens Actuat B Chem. 2023; 390: 134017.
381. Shikha S, Zheng X, Zhang Y. Upconversion nanoparticles-encoded hydrogel microbeads-based multiplexed protein detection. Nano Micro Lett. 2017; 10: 31.
382. Sklenárová D, Hlaváček A, Křivánková J, Brandmeier JC, Weisová J, Řiháček M, et al. Single-molecule microfluidic assay for prostate-specific antigen based on magnetic beads and upconversion nanoparticles. Lab Chip. 2024; 24: 3536–45.
383. Liu Y, Lao X, Wong MC, Song M, Lai H, Wang P, et al. Microfluidic chip-assisted upconversion luminescence biosensing platform for point-of-care virus diagnostics. Adv Healthc Mater. 2024; 13: 2303897.
384. Wimalachandra DC, Li Y, Liu J, Shikha S, Zhang J, Lim YC, et al. Microfluidic-based immunomodulation of immune cells using upconversion nanoparticles in simulated blood vessel-tumor system. ACS Appl Mater Interfaces. 2019; 11: 37513–23.
385. Lyu J, Xu H, Dong B, Li C, Yu S, Hu S, et al. Upconversion luminescence based inverted microfluidic chip for *in situ* CTCs capture monitor and killing. Chem Eng J. 2022; 448: 137761.
386. Geitenbeek RG, Vollenbroek JC, Weijgertze HMH, Tregouet CBM, Nieuwelink AE, Kennedy CL, et al. Luminescence thermometry for *in situ* temperature measurements in microfluidic devices. Lab Chip. 2019; 19: 1236–46.
387. Wu J, Wu J, Wei W, Zhang Y, Chen Q. Upconversion nanoparticles based sensing: From design to point-of-care testing. Small. 2024; 20: e2311729.
388. Hou X, Zhang YS, Trujillo-de Santiago G, Alvarez MM, Ribas J, Jonas SJ, et al. Interplay between materials and microfluidics. Nat Rev Mater. 2017; 2: 17016.
389. Perestrelo AR, Águas ACP, Rainer A, Forte G. Microfluidic organ/body-on-a-chip devices at the convergence of biology and microengineering. Sensors. 2015; 15: 31142–70.
390. Koczula KM, Gallotta A. Lateral flow assays. Essays Biochem. 2016; 60: 111–20.
391. Sena-Torralba A, Álvarez-Diduk R, Parolo C, Piper A, Merkoçi A. Toward next generation lateral flow assays: Integration of nanomaterials. Chem Rev. 2022; 122: 14881–910.
392. He H, Liu B, Wen S, Liao J, Lin G, Zhou J, et al. Quantitative lateral flow strip sensor using highly doped upconversion nanoparticles. Anal Chem. 2018; 90: 12356–60.
393. Jiao X, Peng T, Liang Z, Hu Y, Meng B, Zhao Y, et al. Lateral flow immunoassay based on time-resolved fluorescence microspheres for rapid and quantitative screening CA199 in human serum. Int J Mol Sci. 2022; 23: 9991.
394. Yu B, Cui Y, Mao X, Li Z, Li Z, Shi G. A time-resolved fluorescence lateral flow immunochromatographic assay based on oriented immobilized antibodies for the ultrasensitive detection of C-peptides in human serum. Anal Chim Acta. 2022; 1208: 339833.
395. Masoumeh Ghorbanpour S, Wen S, Kaitu'u-Lino TJ, Hannan NJ, Jin D, McClements L. Quantitative point of care tests for timely diagnosis of early-onset preeclampsia with high sensitivity and specificity. Angew Chem Int Ed. 2023; 62: e202301193.
396. He W, Wang M, Cheng P, Liu Y, You M. Recent advances of upconversion nanoparticles-based lateral flow assays for point-of-care testing. Trac Trends Anal Chem. 2024; 176: 117735.
397. Liz-Marzán LM, Kagan CR, Millstone JE. Reproducibility in nanocrystal synthesis? Watch out for impurities!. ACS Nano. 2020; 14: 6359–61.
398. Vealan K, Joseph N, Alimat S, Karumbati AS, Thilakavathy K. Lateral flow assay: A promising rapid point-of-care testing tool for infections and non-communicable diseases. Asian Biomed. 2023; 17: 250–66.
399. Liang G, Wang H, Shi H, Wang H, Zhu M, Jing A, et al. Recent progress in the development of upconversion nanomaterials in bioimaging and disease treatment. J Nanobiotechnology. 2020; 18: 154.
400. Gerelkhuu Z, Lee YI, Yoon TH. Upconversion nanomaterials in bioimaging and biosensor applications and their biological response. Nanomaterials. 2022; 12: 3470.
401. Henderson IM, Benevidez AD, Mowry CD, Watt J, Bachand GD, Kirk ML, et al. Precipitation of gadolinium from magnetic resonance imaging contrast agents may be the Brass tacks of toxicity. Magn Reson Imaging. 2025; 119: 110383.
402. Li R, Ji Z, Dong J, Chang CH, Wang X, Sun B, et al. Enhancing the imaging and biosafety of upconversion nanoparticles through phosphonate coating. ACS Nano. 2015; 9: 3293–306.
403. Lucky SS, Idris NM, Huang K, Kim J, Li Z, Thong PSP, et al. *In vivo* biocompatibility biodistribution and therapeutic efficiency of titania coated upconversion nanoparticles for photodynamic therapy of solid oral cancers. Theranostics. 2016; 6: 1844–65.
404. Rodríguez-Gómez FD, Monferrer D, Penon O, Rivera-Gil P. Regulatory pathways and guidelines for nanotechnology-enabled health products: A comparative review of EU and US frameworks. Front Med. 2025; 12: 1544393.
405. van der Zee M, de Vries C, Masa M, Morales M, Rayo M, Hegger I. Regulatory aspects of a nanomaterial for imaging therapeutic cells. Drug Deliv Transl Res. 2023; 13: 2693–703.
406. Younis MA, Tawfeek HM, Abdellatif AAH, Abdel-Aleem JA, Harashima H. Clinical translation of nanomedicines: Challenges opportunities and keys. Adv Drug Deliv Rev. 2022; 181: 114083.
407. Wang X, Fu J, Jiang C, Liao X, Chen Y, Jia T, et al. Specific and long-term luminescent monitoring of hydrogen peroxide in tumor metastasis. Adv Mater. 2023; 35: e2210948.
408. Hou B, Yi L, Hu D, Luo Z, Gao D, Li C, et al. A swallowable X-ray dosimeter for the real-time monitoring of radiotherapy. Nat Biomed Eng. 2023; 7: 1242–51.
409. Liu Y, Lao X, Wong MC, Song M, Zhao Y, Ma Y, et al. Intelligent point-of-care biosensing platform based on luminescent nanoparticles and microfluidic biochip with machine vision algorithm analysis. Nano-Micro Lett. 2025; 17: 215.
410. Li H, Liu H, Wong KL, All AH. Lanthanide-doped upconversion nanoparticles as nanoprobes for bioimaging. Biomater Sci. 2024; 12: 4650–63.
411. Ma Q, Wang J, Li Z, Lv X, Liang L, Yuan Q. Recent progress in time-resolved biosensing and bioimaging based on lanthanide-doped nanoparticles. Small. 2019; 15: 1804969.
412. Lin B, Lv R, Ju Z, Ansari AA. NIR-II luminescent rare-earth-doped nanomaterials for precision targeted and surgical navigation of tumors. Coord Chem Rev. 2026; 549: 217251.
413. Lv R, Wang Y, Lin B, Peng X, Liu J, Lü WD, et al. Targeted luminescent probes for precise upconversion/NIR II luminescence diagnosis of lung adenocarcinoma. Anal Chem. 2021; 93: 4984–92.
414. Merchant A, Batzner S, Schoenholz SS, Aykol M, Cheon G, Cubuk ED. Scaling deep learning for materials discovery. Nature. 2023; 624: 80–5.
415. Boiko DA, MacKnight R, Kline B, Gomes G. Autonomous chemical research with large language models. Nature. 2023; 624: 570–8.